DISS. ETH NO. 24730

PORE-SCALE INVESTIGATION OF BIOFILM GROWTH IN THREE-DIMENSIONAL POROUS MEDIA

A thesis submitted to attain the degree of

DOCTOR OF SCIENCES of ETH ZURICH

(Dr. sc. ETH Zurich)

presented by

Maxence Carrel

Master of Science, ETH ZURICH

born on 19.08.1988

citizen of Fribourg (FR)

accepted on the recommendation of

Prof. Dr. Markus Holzner, examiner
Prof. Dr. Tanguy Le Borgne, co-examiner
Prof. Dr. Verónica Morales, co-examiner
Prof. Dr. Eberhard Morgenroth, co-examiner

2017

PhD Thesis

Pore-scale investigation of biofilm growth in three-dimensional porous media

Maxence Carrel

October 25, 2017

Abstract

Abstract

Biofilms are ubiquitous bacterial communities developing at aqueous liquid-solid interfaces in many industrial and natural systems. A case of particular interest are porous media, i.e. materials containing voids saturated with water such as soils, where the interplay of the 3D topology of the substratum and complex hydrodynamic and mass transport processes condition the development and morphology of biofilms. There is still a lack of experimental data allowing to describe the coupled interactions between the developing biofilm and the pore-scale hydrodynamic and mass transfer processes.

The first part of this thesis investigates the influence of biofilm growth in porous media on transport processes. The pore-scale hydrodynamics in a progressively bioclogged porous medium are quantified at different time points of biofilm growth with 3D particle tracking velocimetry. The evolution of the Lagrangian flow field obtained reflects the increasing heterogeneity of the porous medium, that results from the formation of preferential flow paths and stagnation zones as biofilm grows. This increase is related to the exponential growth phase of the bacteria. A gamma distribution provides a remarkable fit of the bulk and the high tail of the velocity probability density functions. A correlated continuous time random walk including a stochastic velocity relaxation process allowed to quantitatively capture transport statistics. We anticipate that the parametrization of the velocity distribution and the stochastic model used could be more broadly applied to model transport processes where the heterogeneity of the pore network considered is either inherent to the porous medium itself or changing dynamically due to physico-chemical processes such as mineral dissolution and precipitation or in the case of unsaturated flows with non-negligible gas exchange.

The second part of this work presents a novel approach based on X-ray tomography to access biofilm morphology in a three-dimensional porous medium. Iron sulfate was used as a contrast agent and combined with propagation-based phase-contrast imaging tools. The iron sulfate was added continuously to the biofilm during biofilm growth, so that it was incorporated within the biofilm itself in order to avoid injecting a destructive contrast agent after the biofilm culturing. A Lorentzian Filter, commonly used to perform phase-retrieval in the context of synchrotron X-ray tomography, was applied as a preprocessing filter prior to the tomographic reconstruction in combination with a very long sample-to-detector distance. Here, we exploited the high numerical stability of this filter under the presence of noise to substantially increase the contrast between the biofilm and the surrounding liquid. A comparison of this method an already existing one using particulate barium sulfate suspensions as contrast agent showed that the rheological properties of the non-Newtonian barium sulfate suspension (i.e. shear-thinning fluid) induced a substantial biofilm detachment. Altogether, a quantitative analysis showed that up to 50 % of the biofilm might have had been detached during the injection of the contrast agent.

Finally, we analyze the local influence of hydrodynamics and transport processes on the development of the biofilm. The pore-scale hydrodynamic data obtained with 3D particle tracking velocimetry is combined X-ray micro computed tomography scans performed on the same sample in order to reveal both the structure of the porous medium and of the biofilm. Barium sulfate was injected very slowly, over a duration of 12 hours to limit biofilm detachment. The registration of the hydrodynamic and structural data sets provides the basis for a local analysis of the influence of flow and mass transport on biofilm growth. This analysis reveals wide distributions of wall shear stresses and concentration boundary layer thicknesses. The spatial distribution of the biofilm patches revealed that the wall shear stress controlled the biofilm adhesion, biofilm development and the biofilm thickness. Neither external nor internal mass transfer limitations were observable, which is consistent with the fact that nutrients and electron acceptors were present in excess in the system considered. Interestingly, the wall shear stress remained fairly constant in the vicinity of the biofilm, whereas it increased substantially elsewhere. This allows to indirectly estimate the shear strength of the biofilm and also points at the complex feedback between a developing biofilm and the pore-scale hydrodynamics.

Zusammenfassung

Zusammenfassung

Biofilme sind bakterielle Gemeinschaften, die sich in vielen industriellen und natürlichen Systemen an flüssig-festen Grenzflächen bilden. Von besonderem Interesse sind Biofilme in porösen Medien, d.h. Materialen, die mit Wasser gesättigten Poren enthalten. In porösen Medien definieren die 3D Topologie des Substratums und die komplexe Strömungs- und Stofftransportsverhältnisse das Biofilmwachstum und die Biofilmmorphologie. Es gibt einen Mangel an experimentellen Daten, die die gekoppelten Wechselwirkungen zwischen den Biofilm und die Strömungs- und Stofftransportsverhältnisse beschreiben.

Der erste Teil dieser Dissertation befasst sich mit dem Einfluss des Biofilmwachstums auf den Stofftransport in porösen Medien. Die sich ändernden Strömungsverhältnisse werden mit einem dreidimensionalen experimentellen Aufbau zur Verfolgung von Partikeln zu vier verschiedenen Zeitpunkten während des Biofilmwachstums gemessen. Die zeitliche Änderung des Lagrangeschen Strömungsfeldes zeigt eine zunehmende Heterogenität des porösen Mediums, die auf die Entstehung von präferenziellen Fliesswegen und entsprechenden stagnierenden Zonen zurückzuführen ist. Diese Zunahme ist mit dem exponentiellen Wachstum der Bakterien in verbunden. Eine Gamma Verteilung zeigt eine bemerkenswert gute Annäherung der Geschwindigkeitsmagnitude. Ein korrelierter Continuous Time Random Walk (CTRW) basierend auf einem stochastischen Relaxationsprozess erlaubt ein quantitatives Modellieren der mittleren und mittleren quadratischen Verschiebung im betrachteten System. Der hier vorgestellte Ansatz konnte zur zeitlichen Modellierung von Stofftransportprozessen innerhalb des exponentiellen Bakterienwachstums angewendet werden. Wir erwarten, dass die vorgeschlagene Parametrisierung der Geschwindigkeit und der weiteren Parametern des CTRW Modells das Modellieren von Stofftransport in Systemen ermöglichen könnte, in denen die Heterogenität des Porennetzwerks entweder inhärent Teil der Struktur des berücksichtigten porösen Medium ist oder sich im Verlauf der Zeit, als Konsequenz physikalisch-chemischen Prozesse wie mineralischer Lösung oder Ausfällung oder im Falle ungesättigter Strömung durch nicht-vernachlässigbaren Gasaustausch, verändert.

Der zweite Teil dieser Arbeit beschreibt einen neuen Ansatz um die Biofilmmorphologie in einem dreidimensionalen porösen Medium anhand von Röntgenbildern zu erfassen. Zum ersten Mal wurde Eisensulfat als Kontrastmittel eingesetzt und zusätzlich mit Methoden aus der Propagationphasenkontrast-Bilderfassung kombiniert. Das Eisensulfat wurde kontinuierlich während des Biofilmwachstums zugegeben, sodass es in den Biofilm eingebaut wurde um die negativen Konsequenzen einer Kontrastmittelinjektion nach dem Biofilmwachstum zu vermeiden. Ein Lorentzfilter, der üblicherweise zum Zweck des Phasenkontrastes mit Synchrotronbildern eingesetzt wird, wurde hier in Kombination mit einer sehr langen „sample-to-detector“ Distanz als vorbereitender Schritt vor der tomographischen Rekonstruktion eingebaut. Dank der hohen numerischen Stabilität des Filters in Anwesenheit von Rauschen konnte der Kontrast zwischen dem Biofilm und der umgebenden Flüssigkeit erhöht werden. Ein Vergleich dieser Methode mit der auf Bariumsulfat basierenden zeigte, dass die rheologischen Eigenschaften der nicht-newtonisches Bariumsulfatsuspension (scherverdünnend) eine Ablösung eines Teiles des Biofilms verursachte. Zusätzlich konnte Abrasion als ein weiterer Ablösungsmechanismus ermittelt werden. Eine quantitative Analyse zeigte, dass bis ca. 50 % des Biofilms während der Injektion des Kontrastmittels abgelöst wurde.

Der letzte Teil dieser Arbeit ist dem lokalen Einfluss der Strömungsverhältnisse und des Stofftransports auf die porenskalige Biofilmentwicklung gewidmet. Zusätzlich zu den hydrodynamischen Messungen wurden Röntgenbilder aufgenommen und die Struktur des Biofilms und des porösen Mediums mittels Mikrocomputertomographie rekonstruiert. Bariumsulfat wurde sehr langsam injiziert, über eine Dauer von 12 Stunden, um Biofilmablösung zu vermeiden. Die Registrierung der Strömungs- und der strukturellen Daten erlaubt eine Analyse des Einflusses der lokalen Strömungs- und Stofftransportsverhältnisse auf die Biofilmentwicklung. Diese Analyse zeigt breite Verteilungen der Wanschubspannung und der Konzentrationsgrenzschichtdicke. Die räumliche Verteilung des Biofilms zeigt, dass die Wandschubspannung die Biofilmadhäsion, Biofilmentwicklung und Biofilmdicke kontrolliert. Weder interne noch externe Stofftransporteinschränkungen wurden beobachtet, was im Einklang mit den hohen Nährstoffen- und Oxidationsmittelnkonzentrationen ist. Auffälligerweise bleibt die Wandschubspannung relativ konstant in der Nähe des Biofilms, während es an weiteren Stellen substantiell zunimmt. Das erlaubt indirekt die Biofilmscherkraft abzuschätzen und deutet auf die komplexe Wechselwirkungen zwischen den Biofilm und die Strömungsverhältnisse.

Contents

Abstract i

Zusammenfassung iii

1 Introduction 3
- 1.1 Motivation . . . 3
- 1.2 Summary . . . 8

2 Pores-scale hydrodynamics in a progressively bio-clogged three-dimensional porous medium: 3D particle tracking experiments and stochastic transport modeling 23
- 2.1 Introduction . . . 24
- 2.2 Material and Methods . . . 25
  - 2.2.1 Porous Media and Working Fluid . . . 25
  - 2.2.2 Biofilm Growth and Hydrodynamic Conditions . . . 26
  - 2.2.3 3D-PTV Measurements . . . 26
- 2.3 Results . . . 28
  - 2.3.1 Experimental pore-scale characterization of the progressive bio-clogging 28
  - 2.3.2 Lagrangian velocity probability density functions . . . 29
  - 2.3.3 Velocity auto-correlation functions . . . 29
  - 2.3.4 Approximation of the velocity magnitude with a gamma distribution 31
  - 2.3.5 Temporal evolution of the hydrodynamic quantities . . . 33
  - 2.3.6 Correlated continuous time random walk . . . 33
  - 2.3.7 Displacement statistics . . . 34
  - 2.3.8 Conditional displacement PDFs . . . 34
- 2.4 Discussion . . . 36
- 2.5 Conclusion . . . 38
- 2.6 Acknowledgments . . . 38

3 Biofilm Imaging in Porous Media by Laboratory X-ray Tomography: Combining a Non-Destructive Contrast Agent with Propagation-Based Phase-Contrast Imaging Tools 47
3.1 Introduction 48
3.2 Materials and Methods 50
  3.2.1 Porous media and Biofilm culturing 50
  3.2.2 Contrast agents 51
  3.2.3 X-ray imaging 52
  3.2.4 Image analysis 53
3.3 Results 58
3.4 Discussion 60
3.5 Conclusion 62

4 Supplementary material to Chapter 3 73
4.1 Segmentation of the LFeSO$_4$ data set 73
4.2 Segmentation of the BaSO$_4$ data set 73
4.3 Effect of the rheological properties of the BaSO$_4$ on the wall shear stress . . 76
4.4 Biofilm detachment upon injection of the BaSO$_4$ suspension 77
4.5 Theoretical derivation of the Lorentzian filter from first principles 78

5 Biofilms in 3D porous media: delineating the influence of the pore network geometry, flow and mass transport on biofilm development 85
5.1 Introduction 86
5.2 Material and Methods 88
  5.2.1 Porous Medium 88
  5.2.2 Biofilm Culturing 88
  5.2.3 Three-Dimensional Particle Tracking Velocimetry 89
  5.2.4 X-ray microtomography 90
  5.2.5 Registration 90
  5.2.6 Calculation of local wall shear stress and concentration boundary layer thickness 91
5.3 Results 92
  5.3.1 Registered Data 92
  5.3.2 Influence of biofilm growth on pore scale statistics 92
  5.3.3 Local statistical analysis 95
  5.3.4 Morphology of the biofilm patches 96
  5.3.5 Relation between pore-scale velocities and radii 97
5.4 Discussion 97
  5.4.1 Which variable does locally control biofilm development? 97
  5.4.2 Local vs. Non-local mass transfer 100
  5.4.3 Influence of biofilm growth on the pore-scale radii and velocity distributions 100
5.5 Conclusions 101
5.6 Acknowledgments 102

6 Supplementary material to Chapter 5 **107**
6.1 Quantitative analysis of the refractive index matching 107
6.1.1 Three-dimensional Particle Tracking Velocimetry 108
6.2 Segmentation and registration 109
6.3 Information concerning the shear stress computation 109

7 Synthesis **115**
7.1 Conclusion 115
7.2 Suggestions for future work 117

Acknowledgements **123**

List of Figures

1.1 Hierarchy of scales relevant to bacterial activities in porous media as described in Ginn et al. (2006) 5

2.1 Photographs illustrating progressive changes in the porous media with increasing bio-clogging of the flow cell (top) and particle trajectories obtained by 3D-PTV (bottom) for the time points T = 0, 36 and 48 h. The bright spot in the upper right corner of the photographs is a reflection by a teflon-coated plastic screw that is used to close the opening of the flow cell. The trajectories are color-coded with the logarithm of the norm of the velocity vector. 28

2.2 Probability density functions of the t-Lagrangian (a) longitudinal velocity component and (b) magnitude obtained at different time points. (c) shows the auto-correlation function of the velocity magnitude, indicating the corresponding correlation lengths in the legend. (d) illustrates the temporal evolution of the average velocity $\langle v \rangle$, the variance of the natural logarithm of the velocity $\sigma^2_{ln(v)}$, the correlation length λ, and of the characteristic velocity v_0, as normalized by their value at the time point T = 0 h. The dashed line shows an exponential fit with growth rate $\mu = 0.015$ h^{-1}. The evolution of α (with dotted line representing the corresponding exponential fit with $\mu_\alpha = 0.012$ h^{-1}) and of the porosity ϕ are illustrated on the same y-axis. The evolution of the normalized velocity variance σ^2_v/σ^2_{v0} is shown on the secondary y-axis (with the dashed-dotted line showing the corresponding fit, $\mu_{\sigma^2_v} = 0.045$ h^{-1}). 30

2.3 Probability density functions of the velocity magnitudes obtained with 3D-PTV, the corresponding MLE gamma distributions and the PDFs of the velocity obtained from the CTRW model for all time points. 32

2.4 (a) Experimental (3D-PTV) and numerical (CTRW) mean m and mean-squared displacements σ^2 obtained for all time points. The spatial moments presented here are dimensionless, as they are rescaled by the corresponding length scales (λ or λ^2). The time is rescaled by the advective time scale τ_A. (b) CTRW mean-squared displacements for all the different time points. (c) Magnification of (b) illustrating a moderate increase in superdiffusive behavior with increasing biofilm growth. The continuous lines in (a) or (b) and (c), respectively, indicate Fickian scaling. 35

2.5 Conditional displacement probability density functions for the 3D-PTV and the CTRW data for all the different time points. The semi-logarithmic insets shows that the propagators never reach a fickian regime where they would follow a Gaussian distribution. 36

3.1 (A) Schematic of the experimental setup used for the biofilm culturing as well as the region of the tubular reactor used for biofilm imaging. (B) Schematic of the configuration used for the X-ray scans where the distances SOD and STD represent the source-to-object (SOD) and the source-to-detector distance (STD). 51

3.2 (A) raw projection image (unfiltered). (B) Lorentz filtered image of (A) using $\alpha = 1.5 \cdot 10^{-7}$. (C) Lorentz filtered image of A using $\alpha = 1.5 \cdot 10^{-8}$. The same dynamic range was used for (A), (B) and (C) for the sake of comparison. (D) displays horizontal normalized profiles at the location of the dashed line in (A), and (B) and (C) as well as for additional values of α. The inset shows a magnification of the gray value profile at the center of the tubular reactor. The scale bar in (A) is also valid on (B) and (C). . . . 55

3.3 Slices from the $FeSO_4$ (A) and $LFeSO_4$ (C) datasets. For the sake of comparison, both images were normalized with 0.4 % of the pixels saturated. The two red resp. blue arrows indicate the location and direction at which the gray value profiles are extracted. The scale bar represents 1 mm. Gray value profile for the first (P1, (D) and the second location P2, (B)). The profiles are labeled with the different phases observed. 56

3.4 Middle slices (filtered prior to segmentation according information in Table 3.1) for the $LFeSO_4$ (A) and $BaSO_4$ (B) datasets. The corresponding 8 bit gray value histograms are shown in C) for the $BaSO_4$ (blue) dataset and for the $LFeSO_4$ (red) dataset after contrast enhancement and application of the 3D curvature-driven diffusive filter. For the $LFeSO_4$ dataset, the vertical dashed lines in yellow, purple and green correspond to isosurface values of 64, 73 and 82 used for the segmentation and the corresponding sensitivity analysis. The peaks corresponding to the different phases are annotated. (D) and (E) show the segmented datasets where the solid, liquid and biofilm phases are color coded in white, blue and green respectively. The scale bar represents 1 mm. 57

3.5 Three-dimensional renderings of the solid phase (left), of the sample imaged with $FeSO_4$ (center) and barium suflate (right) as a contrast-enhancing agents. 58

3.6 Profiles of the volumetric fractions (S: solid, L: liquid, BF: biofilm) obtained for the different datasets ($BaSO_4$: small dashes, $FeSO_4$: longer dashes). The shaded region is defined by the results obtained for the threshold sensitivity analysis. For the sake of clarity, the results of this sensitivity analysis are not added to the liquid phases. The average volumetric fractions (in percent) for the different phases (Solid V_S, Liquid V_L, Biofilm V_{BF}) obtained with the two different contrast-enhancing agents is given in the legend. 59

3.7 Schematic of biofilm detachment mechanisms during $BaSO_4$ injection. . . . 61

4.1 Extract of the gray value histogram for the $LFeSO_4$ data set (red). The first and second derivative of the histogram are shown in gray respectively dark green. The yellow, purple and light green dashed vertical lines at 8 bit gray value of 64, 73 and 82 represent the uncertainty zone considering the inflection point determination. 74

4.2 A) raw image of the $FeSO_4$ data set. B), C) and D) : biofilm phases obtained for the $FeSO_4$ data set based on 8 bit gray value thresholds of 64, resp. 73 and 82. 74

4.3 Histogram of the whole $BaSO_4$ data set (blue) and after the substraction of the solid phase obtained with the seeded region growin algorithm (dashed blue). The yellow, purple and green vertical lines represent the 8 bit gray value threhsolds of 102, 110 and 118 used for the sensitivity analysis. 75

4.4 A) raw image of the $BaSO_4$ data set. B), C) and D) : liquid phases obtained for the $BaSO_4$ data set based on 8 bit gray value thresholds of 102, resp. 110 and 118. 75

4.5 Velocity profile obtained for a flow in a representative pore for the growth solution and for the $BaSO_4$ suspension. 77

4.6 A) Biofilm tubular reactor used in this study. B) and C) images of the biofilm during the injection. The arrow is showing a biofilm patch beeing detached. 78

4.7 Schematic of the configuration used for the X-ray scans where the distances SOD , ODD and STD represent the source-to-object (SOD), object-to-detector and the source-to-detector distance (STD), adapted from Paganin et al. (2002). 79

5.1 Schematic illustration of the experimental set up used for biofilm culturing in (a) and for the 3D-PTV measurements in (b). 89

5.2 (a) and (b) show the registered data 3D-PTV and X-ray of the central zone of the sample prior to biofilm culturing and after 36 hours of biofilm growth. The solid surfaces (nafion grains and biofilm) are here representing a color-coded (nafion grains in gray and biofilm in green) Delaunay triangulation of the segmented X-ray data. (c) and (d) show a local magnification of a pore before and after biofilm colonization. Note that the black points in (c) represent the skeleton along which the pore radii were computed. The colorbar in (d) shows the scale of the velocity magnitude color-coding used for (a)-(d). The skeletons are not shown in (a), (b) and (d) for the sake of clarity. (e) shows the biofilm patches illustrated in (d). (f) shows the same patches and bounding boxes from which the aspect ratio of the patches were computed. Note that the biofilm patches of sizes smaller than 10 voxels visible in (e) and removed in 5.2 (f). 93

5.3 (a) shows probability density functions of the velocity magnitude for different time points during biofilm growth. The probability density functions of the pore radii are presented in (b) whereas (c) and (d) show the probability density functions of the measured wall shear stresses and of concentration boundary layer thicknesses for the clean and bioclogged porous media, respectively. 94

5.4 (a) and (b) show the PDFs of the pore-scale velocity magnitudes for the clean and bioclogged porous medium, whereas (c) and (d) show the corresponding pore radii PDFs. BF and N here indicates if the considered data is located in a one pore radius distance to the biofilm or nafion grains. 95

5.5 (a) and (b) shows the PDFs of wall shear stresses for the clean and bioclogged porous medium. (c) and (d) presents the corresponding concentration boundary layer thicknesses PDFs. BF and N here indicates if the considered data is located within a one pore radius distance to the biofilm or nafion grains. 96

5.6 (a) shows the PDF of the biofilm patch sizes in the porous media and (b) the distribution of biofilm patch sizes as a function of the pore radius. (c) shows the distribution of aspect ratio and (d) the patch size distribution as a function of the aspect ratio. (e) shows the distribution of the biofilm thickness and (f) shows the biofilm thickness as a function of the wall shear stress. 98

5.7 (a) and (b) show the joint PDFs of $v/\langle v\rangle$ and $r_P/\langle r_P\rangle$ for the clean and bioclogged porous media. The dashed and dashed-dotted lines show power laws with exponents of 2 and -2 respectively. The white circles are conditional averages of $v/\langle v\rangle$ on $r_P/\langle r_P\rangle$ and the continous line is a regression of the conditonal average. The exponents of the regression are indicated. . . . 99

6.1 Cropped lines, segmented lines and corresponding linear regressions obtained for glucose concentrations of 0 (a) and 11 % w/v (b). (c) SRMSE values obtained for different glucose concentrations. (d) temporal evolution of the SRMSE during biofilm culturing. 108
6.2 (a) and (b) show the raw and segmented slices obtained from the X-ray scan performed without the addition of contrast agent. (c) and (d) show similar slices obtained after the addition of the contrast agent. (e) and (f) show slices of the registered 3D-PTV and X-ray data. 110
6.3 (a) Close up of a pore with the surface of the nafion grain in blue and normal to the faces obtained by Delaunay triangulation in red. (b) Nafion grains in dark gray, velocity-coded Lagrangian flow data and location of the pore central lines in black. A normal to one of the faces is shown in blue. (c) shows the Eulerian flow field obtained by mapping the Lagrangian data on a grid of 100 μm meshsize. 111

Chapter 1

Introduction

1.1 Motivation

Biofilms are sessile microorganisms developing at solid-liquid interfaces (Costerton et al., 1995). The peculiarity of biofilms lies within the matrix consisting of extracellular polymeric substances (EPS) that they produce (Flemming and Wingender, 2010). The EPS matrix protects biofilms so efficiently from their environment, that they persistently survive in natural, industrial or biomedical settings (Hall-Stoodley et al., 2004) and form one of the most successful, abundant and oldest forms of life on Earth (Costerton et al., 1995; Westall et al., 2001). As such, these bacterial communities form fascinating microbial lanscapes (Battin et al., 2007) exhibiting heterogeneous structures (Van Loosdrecht et al., 1997) ranging over wide ranges of scales (Milferstedt et al., 2009) and shaped by the interplay between shear stresses, mass transfer and nutrient limitations (Picioreanu et al., 1998; Eberl et al., 2000). Reactions due to bacterial activity causes the formation of chemical gradients and nutrient limitations promoting the formation of multispecies biofilms (Picioreanu et al., 2004). This results in biofilms with bacterial populations of diverse genotypes and phenotypes expressing different metabolic pathways (Stewart and Franklin, 2008). The vitality, diversity and ubiquity of biofilms can represent a substantial issue, as on the one hand, biofilms were identified to be at the root of a variety of persistent infections (Costerton et al., 1999) and can lead to an up to 1000-fold increase in antibiotics resistance (Mah et al., 2003). On the other hand, one can also capitalize on biofilms for the degradation of organic compounds and nitrogen (Boltz et al., 2017) or toxins (Kohler et al., 2014). Therefore, understanding the development of biofilms in response to local mass transfer and hydrodynamic conditions is of paramount interest for a wide range of research fields spanning from biomedical research (Donlan and Costerton, 2002) or drinking water production (Derlon et al., 2012) and wastewater treatment (Martin and Nerenberg, 2012) to the carbon cycle (Battin et al., 2008), sediment transport (Vignaga et al., 2013) or energy production (Oh et al., 2010) and storage (Ebigbo et al., 2013).

Some authors introduced a scale separation in order to understand the implications of biofilm related processes for the different applications mentioned (Ginn et al., 2006; Battin et al., 2007; Morgenroth and Milferstedt, 2009; Milferstedt et al., 2009; Wagner et al., 2010b; Davit et al., 2013). This scale separation usually distinguishes between three biofilm related typical scales, namely the micro-, meso- and macroscales.

At the microscale, several microscopy techniques allow to image the sub-micron distribution of biofilms and their constituents, such as confocal laser scanning microscopy (CLSM) (Neu et al., 2001) or Raman microscopy (Ivleva et al., 2008; Wagner et al., 2009). These imaging methods are typically used to study the functions, properties and constituents of the EPS or to understand which mechanisms underpin initial attachment of individual bacteria. For instance, initial adhesion was shown to be determined by microscale velocity gradients (Rusconi et al., 2014; Yawata et al., 2016).

Zooming out, the mesoscale is the scale at which the interplay between the topology of the substratum on which biofilms grow and flow and mass transfer processes (Picioreanu et al., 1998; Eberl et al., 2000) orcompetition in multispecies biofilms (Picioreanu et al., 2004) shape the evolving bacterial structures. Further microscopy techniques are typically used to image biofilms at the mesoscale, optical coherence tomography (OCT) being the state of the art method actually available (Wagner and Horn, 2017). OCT based studies allowed to gain some insights about the structural or rheological properties of biofilms (Wagner et al., 2010b; Blauert et al., 2015) or the biofouling occuring upon biofilm development in feed spacer channels in reverse osmosis membrane modules (West et al., 2016) or drip irrigation devices (Qian et al., 2017). Further studies showed that the structures of biofilms developing on ultrafiltration membranes were shaped by the predation of grazing protozoan (Derlon et al., 2012) or the activity of metazoa (Derlon et al., 2013), so that biofilms ultimately increase membrane flux and permeate quality (Derlon et al., 2014).

Finally, the macroscale is the scale of larger systems such a reactors (Boltz et al., 2017), aquifers (Meckenstock et al., 2015) or streams (Battin et al., 2016) influenced by biofilms as overarching sytems. The different scales mentioned are highly interconnected as for instance, the overall performance of a trickling filter reactor (Gujer and Boller, 1986) results from the integral of small scale processes such as reactions or biofilm detachment. This results in bi-directional feedbacks between small and large scales and as well upscaling approaches as approaches tackling the cascade towards smaller scale are to be further developed and compared against small and large scale experimental evidence.

Most natural or industrial systems colonized by biofilms exhibit rough three-dimensional (3D) features or corners. Commons examples are teeth and corrugated pipes (Drescher et al., 2013; Kim et al., 2016) or porous media (Coyte et al., 2017). Porous media contain interconnected voids or pores forming three-dimensional networks with pore radii spanning over a wide range of length scales (Holzner et al., 2015). The very high surface area of porous media offers multitudes of niches enhancing bacterial activity and diversity in general and more specifically biofilm development under both saturated and unsaturated conditions (Ginn et al., 2002; Gans et al., 2005; Curtis and Sloan, 2005; Or et al., 2007; Pérez-Reche et al., 2012). Biofilms are therefore relevant for a variety of engineering problems involving materials that can be considered to be porous like the clogging of biomedical devices such as catheters (Drescher et al., 2013) or of membrane feed spacers (Picioreanu et al., 2009), natural aquifer bioremediation (Meckenstock et al., 2015) or bioremediation by means of permeable reactive barriers (Blowes et al., 2000), microbial enhanced oil recovery (Lappin-Scott et al., 1988; MacLeod et al., 1988) or sequestration of carbon dioxide (Ebigbo et al., 2010; Mitchell et al., 2013).

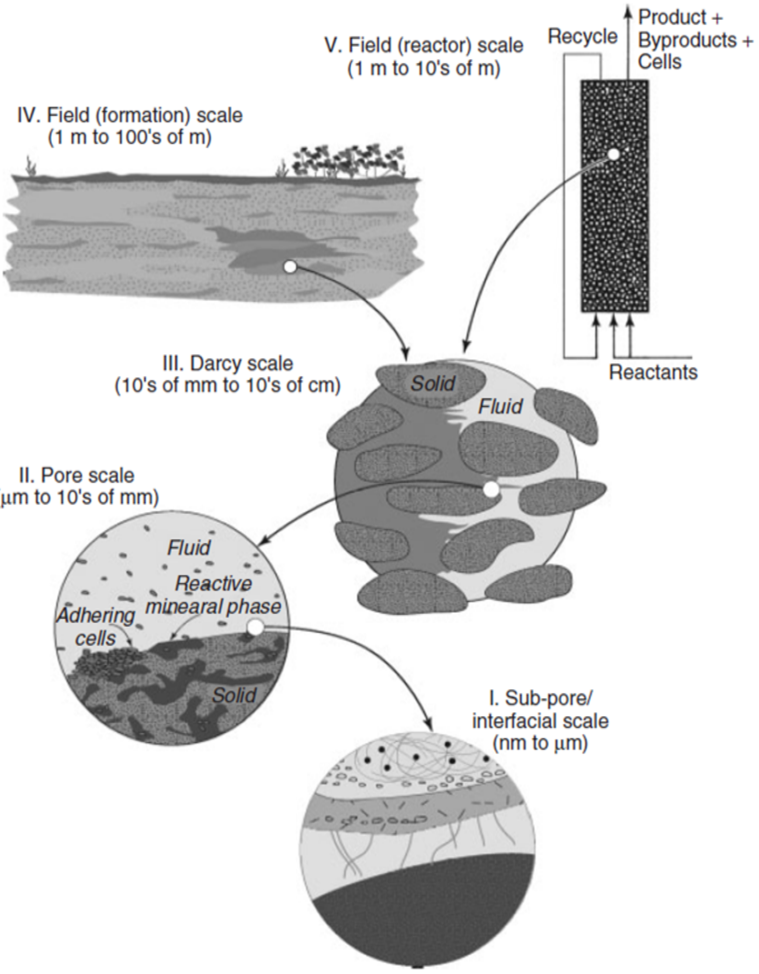
V. Field (reactor) scale
(1 m to 10's of m)
Recycle
Product +
Byproducts +
Cells
IV. Field (formation) scale
(1 m to 100's of m)
Reactants
III. Darcy scale
(10's of mm to 10's of cm)
Solid
Fluid
II. Pore scale
(μm to 10's of mm)
Fluid
Reactive
minearal phase
Adhering
cells
Solid
I. Sub-pore/
interfacial scale
(nm to μm)

Figure 1.1: Hierarchy of scales relevant to bacterial activities in porous media as described in Ginn et al. (2006)

The scale separation introduced earlier can be applied to porous media systems in order to understand the implications of biofilm growth in this context. Figure 1.1 presents such a hierarchy of scales and indicates an approximate order of magnitude for each different scale. The microscale is here represented as the sub-pore/interfacial scale, the mesoscale corresponding to the pore scale and the field or reactor scale to the macroscale. The Darcy scale represented in Figure 1.1 is an intermediate scale between the pore scale and the field scale. The details of the pore scale are typically treated as homogeneous at the Darcy scale yielding quantities (porosity, permeability etc.) allowing to model flow and transport at the field or reaction scale with formulations based on Darcy's law.

The present study is focusing on the development of biofilms at the mesoscale (pore scale) in porous media. This scale is of crucial importance as it links processes happening at the micro-scale to the macro-scale systems such as reactors or aquifers. Historically, the first experimental studies involving biofilms in porous media were soil column experiments in which bulk variables (pressure drop, hydraulic conductivity or permeability) were quantified (Taylor and Jaffé, 1990; Cunningham et al., 1991; Baveye et al., 1998). Later on, microscopic studies allowed to investigate biofilm development in flow cells containing glass beads or mimicking porous media (Stoodley et al., 1994; Sharp et al., 1999). The growth of biofilms in this context was identified to strongly depend on the dimensionality considered, i.e. 1D, 2D or 3D (Seki et al., 2006; von der Schulenburg et al., 2009). Previous experimental studies either considered 2D porous network (Sharp et al., 1999; Dupin and McCarty, 2000; Vayenas et al., 2002; Marty et al., 2012) or 3D hydrodynamics within channels mimicking 2D porous networks (Rusconi et al., 2010, 2011; Guglielmini et al., 2011; Drescher et al., 2013). For instance, von der Schulenburg et al. (2009) presented the first numerical study in a fully 3D porous medium and showed that the dynamics of biofilm development were substantially different in 2D or 3D, i.e. the influence of the growing biofilm on the velocity field was substantially stronger in 2D than in 3D. Many numerical studies considering biofilms in porous media (Kapellos et al., 2007; Pintelon et al., 2009; von der Schulenburg et al., 2009; Bottero et al., 2013) rely on assumptions relative to the initial bacterial adhesion or on the material properties of biofilms (e.g. biofilm shear strength or resistence to shear) that are extracted from the literature for biofilms grown under other conditions, (substratum topology, nutrients etc.) and it is well known that these properties can be highly variable and strongly case dependent. For instance, biofilm shear strengths spanning over order of magnitudes were measured in the context of dental plaque, venous catheters or capillary reactors (Stewart, 2014; Blauert et al., 2015). Therefore, there still remains a lack of understanding of biofilm development in fully 3D porous media. Some attempts in that direction were already done, as for example the work by Seymour et al. (2004, 2007) using magnetic resonance microscopy (MRM) to image biofilm growth in 3D bead packs. However, these studies did not allow to retrieve the exact spatial distribution and the morphology of the biofilm patches in the system considered or provide some information about the biofilm shear strength in these systems. Biofilm spatial distribution and morphology could be accessed using MRM in another study (Wagner et al., 2010a), which was considering biofilm growth in a capillary tube reactor. However, as biofilm growth in porous media induces the formation of stagnation zones in which mass transfer is dominated by molecular diffusion, differentiation of the biofilm from these stagnation zones in the structural data obtained with MRI is difficult and has not been performed until now.

The pioneering work by Seymour et al. (2004, 2007) revealed a strong impact of the growing biofilm on the pore-scale flow and hydrodynamics. Namely, biofilm growth enhanced pore-scale dispersion and induced a transition from Gaussian to non-Gaussian dynamics, a phenomenon commonly referred to as non-Fickian or anomalous transport. Anomalous transport is a phenomenon characterized by incomplete mixing or enhanced spreading and persistently spans from the pore to the field scale in heterogeneous porous media (Berkowitz et al., 2000; Gouze et al., 2008; Neuman and Tartakovsky, 2009; Le Borgne et al., 2011b; de Anna et al., 2013). Several authors presented data in which the heterogeneity added to a porous medium by biofilm growth caused a transition to anomalous transport or the increase of anomalous transport as well at the pore- as at the field scale (Atekwana and Atekwana, 2010; Knecht et al., 2011; Deng et al., 2013; Vogt et al., 2013; Kone et al., 2014). Thereby, anomalous transport is commonly characterized by non-Gaussian velocity distributions (Bijeljic et al., 2013; Matyka et al., 2016), high temporal correlation of velocities along intermittent fluid particle trajectories (Le Borgne et al., 2011a; de Anna et al., 2013). Accounting for anomalous dispersive processes is necessary in order to model pollutant plume transport and to optimally biodegradation processes at the field scale (Meckenstock et al., 2015).

Recent studies presented upscaling approaches allowing to numerically consider the influence of biofilm growth on transport and reaction processes. Several continuum approaches modeling Darcy-scale transport with advection-dispersion-reaction equations in which the dispersion tensor was obtained with volume averaging techniques were presented (Golfier et al., 2009; Orgogozo et al., 2010; Davit et al., 2010; Kapellos et al., 2010, 2012). However, these models were up to now not compared to experimental results as the dispersion tensor mentioned needs to be defined based on experimental data. Additionally, these theoretical formulations describe asymptotic heterogeneity-induced transport and do not account for the fact that such asymptotic behaviors are often not reached at the field scale. Finally, as the work by Seymour et al. (2004) showed, bioclogging is a dynamic process, so that accounting for the dynamics of biofilm development is also necessary in oder to accurately model transport processes. Lately, transport during the preasymptotic regime has been sucessfully reproduced by continuous time random walks (Dentz and Berkowitz, 2003; Neuman and Tartakovsky, 2009; Le Borgne et al., 2011a; de Anna et al., 2013). Such a stochastic approach was also presented by (Seymour et al., 2004) to model transport in the considered system qualitatively using a conceptual continuous time random walk assuming a power law Lévy wait time distribution and a Gaussian jump length distribution. However, this approach did not quantitatively consider the temporal evolution of the bioclogged porous medium in order to model transport dynamics.

A first goal of this thesis was to adapt existing experimental methods in order to obtain pore scale hydrodynamic information in a progressively bioclogged three-dimensional porous medium. In order to access the pore scale flow, 3D particle tracking velocimetry (3D-PTV) experiments were performed at different time points in a porous medium in which biofilm was being cultured. The 3D-PTV code used in this work was already extensively used in order to access position, velocity, acceleration and related hydrodynamic quantities in different kind of flows (Luethi et al., 2005; Hoyer et al., 2005; Gülan et al., 2012; Saha et al., 2014; Michalec et al., 2015; Holzner et al., 2015; Schmidt et al., 2016; Morales et al., 2017). The use of refractive index matched porous media allows to use this method in order to obtain pore-scale hydrodynamic information (Moroni and Cushman, 2001; Holzner et al., 2015; Morales et al., 2017) in 3D porous media. Based on the pore-scale hydrodynamic information gathered, a description of the evolution of transport processes in the progressively bioclogged system is performed. Additionally, the transport processes are modeled with a correlated continous time random walk based on a gamma distribution of the velocity magnitude and assuming a stochastic velocity relaxation.

A second goal of this thesis was to delineate the interplay between the pore network topology and the flow and mass transport processes on biofilm development. X-ray micro computed tomography was used to obtain both structural information about the porous medium and the biofilm morphology. X-ray micro computed tomography (mCT) has become a standard tool for imaging soil samples (Wildenschild et al., 2002; Wildenschild and Sheppard, 2013) and was used to image biofilm structures in 3D soil-like samples (Davit et al., 2011). The segmentation of the biofilm, solid and liquid phases is a difficult task when using X-ray microtomography due to the high water content of biofilms and the consecutively very close density and attenuation coefficients of water and biofilms. The use of contrast agents is therefore necessary in order to increase the contrast between the biofilm and the surrounding liquid. Several studies were performed testing different contrast agents such as silver-coated microspheres, barium sulfate or 1-chloronaphtalene (Iltis et al., 2011; Davit et al., 2011; Rolland du Roscoat et al., 2014; Ivankovic et al., 2016). Thereby, the physical or chemical interactions between biofilms and the contrast agents were not considered thoroughly. These interactions include the detachment of the biofilm due to the injection of the contrast agent, as observed for barium sulfate by Davit et al. (2011) or the impact of the powerful pesticide 1-chloronapthalene on the biofilm. In this study, the use of a novel contrast agent, namely iron sulfate, was presented. This contrast agent is added continuously to the biofilm during biofilm growth, so that biofilm morphologies can be obtained in a non-destructive way, which was confirmed by a comparison with biofilm morphologies obtained using an already existing method. Additionally, iron sulfate is a non-toxic inorganic compound naturally found in soil biofilms (Li et al., 2005). Further, biofilm imaging with iron sulfate as a contrast agent was made possible by using imaging tools normally applied for synchrotron X-ray phase-contrast imaging. Finally, the pore scale hydrodynamic and structural information are combined, allowing a pore scale quantitative analysis of the interplay between the porous media topology, the flow and mass transfer processes on the biofilm development. In order to do so, the wall shear stress and concentration boundary layer thickness distributions in are measured and different metrics describing the biofilm morphology (i.e. biofilm patch size, aspect ratio or thickness) and the influence of the local pore network topology (pore radius), wall shear stresses and concentration boundary layer thicknesses on these metrics are considered.

1.2 Summary

This dissertation is composed of three scientific publications presented as individual chapters. The abstract of each publication summarizes the findings presented. The introduction of each of the publications provides some information about the context of the different research lines addressed.

Chapter 2 is about the influence of progressive bioclogging on anomalous transport in porous media, by gathering experimental evidence describing the temporal evolution of pore-scale hydrodynamics and presenting a numerical framework allowing to quantitatively capture these transport processes. Previous work qualitatively linked biofilms to an anomalous transport increase (Seymour et al., 2004; Knecht et al., 2011; Kone et al., 2014) but still little was known about the temporal dynamics involved and a quantitative description was still missing. In order to adress this, a biofilm is first grown in a 3D transparent and refractive index matched porous medium. Pore-scale hydrodynamics are measured with 3D-PTV at four different time points during biofilm growth. A statistical analysis of the flow information gathered along trajectories, the so-called Lagrangian flow field, provides a quantitative description of the influence of biofilm growth on pore-scale hydrodynamics. This influence is characterized by an exponential increase in both average and variance of the flow velocity as well of the velocity correlation length. Transport processes in the considered system are characterized by mean-square-displacements reflecting an increasingly non-Fickian spreading behavior. This increase of anomalous transport in the porous medium indicates the formation of preferential flow paths and stagnation zones as the biofilm progressively changes the pore network. The probability density functions (PDFs) of the evolving pore-scale velocity magnitudes can be approximated by a gamma distribution remarkably well capturing the bulk and the high tail of the velocity distributions. With progressive bioclogging, the shape parameter α decreases substantially from 1.9 to 0.9, pointing at an evolving pore arrangement from mainly parallel towards more serial. A correlated continuous time random walk assuming a gamma distribution of the pore-scale velocities and based on a stochastic velocity relaxation model allows to accurately reproduce the temporal evolution of the first two spatial moments (i.e. mean and mean-square displacements) of the experimental data. The findings presented in this chapter provide a framework allowing to describe and model the temporal evolution of a progressively bioclogged porous medium. The approach presented here could also be applied to model transport processes for further porous systems where the heterogeneity considered is either inherent to the porous media itself or is dynamically driven by physico-chemical processes.

Chapter 3 presents an innovative method for biofilm imaging in 3D samples with X-ray microtomography. A biofilm was grown for seven days and imaged with X-rays afterwards. Thereby, phase-contrast tools commonly used in the context of synchrotron X-ray tomography were applied in order to enhance contrast and reduce noise. These tools consisted of a Lorentzian filter ran on the individual X-ray projections prior to tomographic reconstruction and an especially long sample-to-detector distance allowing to enhance refractive effects. Due to the similar densities of high water content biofilms and water, contrast agents are commonly required to reveal the biofilm morphology. The tools mentioned were therefore combined with iron sulfate as a contrast agent, which was never used previously as a contrast agent for X-ray imaging. Additionally, the results obtained with this innovative method were compared with a method using barium sulfate (0.1 g/L) as a contrast agent (Davit et al., 2011). Previous studies had shown that some biofilm detached during the injection of the barium sulfate. However, the actual amount of biofilm detached was never quantitatively measured. In order to avoid detachment, the contrast agent injection flow rate was set 10 times smaller than the biofilm cultivation flow rate. Interestingly, the comparison of both methods revealed that about 50% of the biofilm was detached upon biofilm injection. An analysis accounting for the rheological properties of the barium sulfate suspension showed that even at an injection flow rate 10 times smaller than the cultivation flow rate, the wall shear stress exerted by the contrast agent was 3 times higher than during cultivation. This allowed to identify shear induced detachment as the main detachment mechanism occurring during the contrast agent injection.

Finally, chapter 5 presents a more local analysis on the spatial distribution of biofilm patches in a 3D porous medium in function of local pore-scale hydrodynamics. Here again, 3D-PTV measurements provided a description of the initial flow conditions in the considered system and after 36 h of biofilm growth. The structure of the porous medium and the biofilm spatial distribution within it was obtained from X-ray μCT measurements. A barium sulfate suspension was used here as a contrast agent and injected very slowly over 12 hours to limit biofilm detachment. The registration 3D-PTV hydrodynamic data and of the X-ray structural data allows to perform a pore-scale analysis of the influence the pore network topology, flow and mass transport on biofilm growth. The flow and mass transport processes were accounted for by measuring wall shear stress and concentration boundary layer thickness distributions. A local analysis revealed that these distributions were fairly wide. An investigation regarding the morphology of biofilm patches revealed that the wall shear stresses controlled biofilm adhesion, biofilm development and the biofilm thickness. Due to the presence of nutrients and electron acceptors in excess, mass transfer did not influence biofilm development. The wall shear stresses stayed relatively low in the vicinity of the biofilm, whereas it increased substantially elsewhere, so that a biofilm shear strength could be estimated.

The upcoming chapters 2 - 6 of this thesis are based on the following publications:

Chapter 2: M. Carrel^{a,b,c,d}, V. Morales^{a,b,c,e}, M. Dentz^{b,c,e}, N. Derlon^{a,e}, E. Morgenroth^{a,e} and M. Holzner^{a,c,e}.

Pore-scale hydrodynamics in a progressively bio-clogged three-dimensional porous medium: 3D particle tracking experiments and stochastic transport modelling. Submitted to *Water Resources Research*

[a] Study concept and design; [b] Data acquisition and analysis; [c] Interpretation of data; [d] Drafting manuscript; [e] Critical revision

My contribution to this first chapter started with adapting the flow cell and the porous medium used for the growth of biofilm and developping a biofilm growth protocol. Then, I performed the experiments, analyzed the experimental data and implemented the numerical model, upon which I drafted the manuscript, to which all co-authors contributed.

Chapter 3: M. Carrel[a,b,c,e], M. Beltran[a,b,c,d,f], V. Morales[a,c,f], N. Derlon[a,f], E. Morgenroth[a,f] , R. Kaufmann[a,f]and M. Holzner[a,c,f] (2017).

Biofilm imaging in porous media by laboratory X-ray tomography: combining a non-destructive contrast agent with propagation-based phase-contrast imaging tools. *PLOS ONE*

doi: 10.1371/journal.pone.0180374

[a] Study concept and design; [b] Data acquisition and analysis; [c] Interpretation of data; [d] Developing the theoretical concept; [e] Drafting manuscript; [f] Critical revision

For this third chapter, my contribution was to suggest the use of iron sulfate as a contrast agent and I performed the biofilm culturing. After that, I assisted the data acquisition, performed the analysis and interpretation of the data before drafting the manuscript, to which all co-authors contributed.

Chapter 5: M. Carrel[a,b,c,d], V. Morales[a,b,e], M. Beltran[a,b], N. Derlon[a,e], E. Morgenroth[a,e] , R. Kaufmann[a,e]and M. Holzner[a,c,e]

Biofilms in 3D porous media: delineating the influence of the pore network topology, flow and mass transport on biofilm development. Submitted to *Water Research*

[a] Study concept and design; [b] Data acquisition and analysis; [c] Interpretation of data; [d] Drafting manuscript; [e] Critical revision

For this fifth chapter, I performed and fine tuned the 3D-PTV and X-ray measurements as well as took care of the data analysis. Finally, I wrote the manuscript that was significantly improved by the contributions of all co-authors.

Bibliography

Atekwana, E. A. and Atekwana, E. A. (2010). Geophysical signatures of microbial activity at hydrocarbon contaminated sites: A review. *Surveys in Geophysics*, 31(2):247–283. pages

Battin, T. J., Besemer, K., Bengtsson, M. M., Romani, A. M., and Packmann, A. I. (2016). The ecology and biogeochemistry of stream biofilms. *Nat Rev Micro*, 14(4):251–263. pages

Battin, T. J., Kaplan, L. A., Findlay, S., Hopkinson, C. S., Marti, E., Packman, A. I., Newbold, J. D., and Sabater, F. (2008). Biophysical controls on organic carbon fluxes in fluvial networks. *Nature Geosci*, 1(2):95–100. 10.1038/ngeo101. pages

Battin, T. J., Sloan, W. T., Kjelleberg, S., Daims, H., Head, I. M., Curtis, T. P., and Eberl, L. (2007). Microbial landscapes: new paths to biofilm research. *Nat Rev Micro*, 5(1):76–81. pages

Baveye, P., Vandevivere, P., Hoyle, B. L., DeLeo, P. C., and de Lozada, D. S. (1998). Environmental impact and mechanisms of the biological clogging of saturated soils and aquifer materials. *Critical Reviews in Environmental Science and Technology*, 28(2):123–191. pages

Berkowitz, B., Scher, H., and Silliman, S. E. (2000). Anomalous transport in laboratory-scale, heterogeneous porous media. *Water Resources Research*, 36(1):149–158. pages

Bijeljic, B., Raeini, A., Mostaghimi, P., and Blunt, M. J. (2013). Predictions of non-fickian solute transport in different classes of porous media using direct simulation on pore-scale images. *Physical Review E*, 87(1):013011. PRE. pages

Blauert, F., Horn, H., and Wagner, M. (2015). Time-resolved biofilm deformation measurements using optical coherence tomography. *Biotechnology and Bioengineering*, 112(9):1893–1905. pages

Blowes, D. W., Ptacek, C. J., Benner, S. G., McRae, C. W. T., Bennett, T. A., and Puls, R. W. (2000). Treatment of inorganic contaminants using permeable reactive barriers1. *Journal of Contaminant Hydrology*, 45(1–2):123–137. pages

Boltz, J. P., Smets, B. F., Rittmann, B. E., van Loosdrecht, M. C. M., Morgenroth, E., and Daigger, G. T. (2017). From biofilm ecology to reactors: a focused review. *Water Science and Technology*, 75(8):1753–1760. pages

Bottero, S., Storck, T., Heimovaara, T. J., van Loosdrecht, M. C. M., Enzien, M. V., and Picioreanu, C. (2013). Biofilm development and the dynamics of preferential flow paths in porous media. *Biofouling*. pages

Costerton, J. W., Lewandowski, Z., Caldwell, D. E., Korber, D. R., and Lappin-Scott, H. M. (1995). Microbial biofilms. *Annual Review of Microbiology*, 49(1):711–745. pages

Costerton, J. W., Stewart, P. S., and Greenberg, E. P. (1999). Bacterial biofilms: A common cause of persistent infections. *Science*, 284(5418):1318–1322. pages

Coyte, K. Z., Tabuteau, H., Gaffney, E. A., Foster, K. R., and Durham, W. M. (2017). Microbial competition in porous environments can select against rapid biofilm growth. *Proceedings of the National Academy of Sciences*, 114(2):E161–E170. pages

Cunningham, A. B., Characklis, W. G., Abedeen, F., and Crawford, D. (1991). Influence of biofilm accumulation on porous media hydrodynamics. *Environmental Science and Technology*, 25(7):1305–1311. pages

Curtis, T. P. and Sloan, W. T. (2005). Exploring microbial diversity–a vast below. *Science*, 309(5739):1331. pages

Davit, Y., Byrne, H., Osborne, J., Pitt-Francis, J., Gavaghan, D., and Quintard, M. (2013). Hydrodynamic dispersion within porous biofilms. *Physical Review E*, 87(1):012718. pages

Davit, Y., Debenest, G., Wood, B. D., and Quintard, M. (2010). Modeling non-equilibrium mass transport in biologically reactive porous media. *Advances in Water Resources*, 33(9):1075–1093. pages

Davit, Y., Iltis, G., Debenest, G., Veran-Tissoires, S., Wildenschild, D., Gerino, M., and Quintard, M. (2011). Imaging biofilm in porous media using x-ray computed microtomography. *Journal of Microscopy*, 242(1):15–25. pages

de Anna, P., Le Borgne, T., Dentz, M., Tartakovsky, A. M., Bolster, D., and Davy, P. (2013). Flow intermittency, dispersion, and correlated continuous time random walks in porous media. *Physical Review Letters*, 110(18):184502. PRL. pages

Deng, W., Cardenas, M. B., Kirk, M. F., Altman, S. J., and Bennett, P. C. (2013). Effect of permeable biofilm on micro- and macro-scale flow and transport in bioclogged pores. *Environmental Science & Technology*, 47(19):11092–11098. pages

Dentz, M. and Berkowitz, B. (2003). Transport behavior of a passive solute in continuous time random walks and multirate mass transfer. *Water Resources Research*, 39(5):n/a–n/a. pages

Derlon, N., Koch, N., Eugster, B., Posch, T., Pernthaler, J., Pronk, W., and Morgenroth, E. (2013). Activity of metazoa governs biofilm structure formation and enhances permeate flux during gravity-driven membrane (gdm) filtration. *Water Research*, 47(6):2085–2095. pages

Derlon, N., Mimoso, J., Klein, T., Koetzsch, S., and Morgenroth, E. (2014). Presence of biofilms on ultrafiltration membrane surfaces increases the quality of permeate produced during ultra-low pressure gravity-driven membrane filtration. *Water Research*, 60(0):164–173. pages

Derlon, N., Peter-Varbanets, M., Scheidegger, A., Pronk, W., and Morgenroth, E. (2012). Predation influences the structure of biofilm developed on ultrafiltration membranes. *Water Research*, 46(10):3323–3333. pages

Donlan, R. M. and Costerton, J. W. (2002). Biofilms: Survival mechanisms of clinically relevant microorganisms. *Clinical Microbiology Reviews*, 15(2):167–193. pages

Drescher, K., Shen, Y., Bassler, B. L., and Stone, H. A. (2013). Biofilm streamers cause catastrophic disruption of flow with consequences for environmental and medical systems. *Proceedings of the National Academy of Sciences*, 110(11):4345–4350. pages

Dupin, H. J. and McCarty, P. L. (2000). Impact of colony morphologies and disinfection on biological clogging in porous media. *Environmental Science and Technology*, 34(8):1513–1520. pages

Eberl, H. J., Picioreanu, C., Heijnen, J. J., and van Loosdrecht, M. C. M. (2000). A three-dimensional numerical study on the correlation of spatial structure, hydrodynamic conditions, and mass transfer and conversion in biofilms. *Chemical Engineering Science*, 55(24):6209–6222. pages

Ebigbo, A., Golfier, F., and Quintard, M. (2013). A coupled, pore-scale model for methanogenic microbial activity in underground hydrogen storage. *Advances in Water Resources*, 61:74–85. pages

Ebigbo, A., Helmig, R., Cunningham, A. B., Class, H., and Gerlach, R. (2010). Modelling biofilm growth in the presence of carbon dioxide and water flow in the subsurface. *Advances in Water Resources*, 33(7):762–781. pages

Flemming, H.-C. and Wingender, J. (2010). The biofilm matrix. *Nat Rev Micro*, 8(9):623–633. 10.1038/nrmicro2415. pages

Gans, J., Wolinsky, M., and Dunbar, J. (2005). Computational improvements reveal great bacterial diversity and high metal toxicity in soil. *Science*, 309(5739):1387. pages

Ginn, T. R., Camesano, T., Scheibe, T. D., Nelson, K. E., Clement, T. P., and Wood, B. D. (2006). *Microbial Transport in the Subsurface.* John Wiley and Sons, Ltd. pages

Ginn, T. R., Wood, B. D., Nelson, K. E., Scheibe, T. D., Murphy, E. M., and Clement, T. P. (2002). Processes in microbial transport in the natural subsurface. *Advances in Water Resources*, 25(8):1017–1042. pages

Gülan, U., Lüthi, B., Holzner, M., Liberzon, A., Tsinober, A., and Kinzelbach, W. (2012). Experimental study of aortic flow in the ascending aorta via particle tracking velocimetry. *Experiments in Fluids*, 53(5):1469–1485. pages

Golfier, F., Wood, B. D., Orgogozo, L., Quintard, M., and Buès, M. (2009). Biofilms in porous media: Development of macroscopic transport equations via volume averaging with closure for local mass equilibrium conditions. *Advances in Water Resources*, 32(3):463–485. pages

Gouze, P., Le Borgne, T., Leprovost, R., Lods, G., Poidras, T., and Pezard, P. (2008). Non-fickian dispersion in porous media: 1. multiscale measurements using single-well injection withdrawal tracer tests. *Water Resources Research*, 44(6):n/a–n/a. pages

Guglielmini, L., Rusconi, R., Lecuyer, S., and Stone, H. A. (2011). Three-dimensional features in low-reynolds-number confined corner flows. *Journal of Fluid Mechanics*, 668:33–57. pages

Gujer, W. and Boller, M. (1986). Design of a nitrifying tertiary trickling filter based on theoretical concepts. *Water Research*, 20(11):1353–1362. pages

Hall-Stoodley, L., Costerton, J. W., and Stoodley, P. (2004). Bacterial biofilms: from the natural environment to infectious diseases. *Nat Rev Micro*, 2(2):95–108. pages

Holzner, M., Morales, V. L., Willmann, M., and Dentz, M. (2015). Intermittent lagrangian velocities and accelerations in three-dimensional porous medium flow. *Physical Review E*, 92(1):013015. pages

Hoyer, K., Holzner, M., Lüthi, B., Guala, M., Liberzon, A., and Kinzelbach, W. (2005). 3d scanning particle tracking velocimetry. *Experiments in Fluids*, 39(5):923–934. pages

Iltis, G. C., Armstrong, R. T., Jansik, D. P., Wood, B. D., and Wildenschild, D. (2011). Imaging biofilm architecture within porous media using synchrotron-based x-ray computed microtomography. *Water Resources Research*, 47(2):W02601. pages

Ivankovic, T., Rolland du Roscoat, S., Geindreau, C., Séchet, P., Huang, Z., and Martins, J. M. F. (2016). Development and evaluation of an experimental protocol for 3-d visualization and characterization of the structure of bacterial biofilms in porous media using laboratory x-ray tomography. *Biofouling*, 32(10):1235–1244. pages

Ivleva, N. P., Wagner, M., Horn, H., Niessner, R., and Haisch, C. (2008). In situ surface-enhanced raman scattering analysis of biofilm. *Analytical Chemistry*, 80(22):8538–8544. pages

Kapellos, G. E., Alexiou, T. S., and Payatakes, A. C. (2007). Hierarchical simulator of biofilm growth and dynamics in granular porous materials. *Advances in Water Resources*, 30(6–7):1648–1667. pages

Kapellos, G. E., Alexiou, T. S., and Payatakes, A. C. (2010). Theoretical modeling of fluid flow in cellular biological media: An overview. *Mathematical Biosciences*, 225(2):83–93. pages

Kapellos, G. E., Alexiou, T. S., and Payatakes, A. C. (2012). A multiscale theoretical model for fluid flow in cellular biological media. *International Journal of Engineering Science*, 51:241–271. pages

Kim, M. K., Ingremeau, F., Zhao, A., Bassler, B. L., and Stone, H. A. (2016). Local and global consequences of flow on bacterial quorum sensing. *Nature microbiology*, 1:15005–15005. pages

Knecht, K., Schroth, M. H., Schulin, R., and Nowack, B. (2011). Development and evaluation of micro push–pull tests to investigate micro-scale processes in porous media. *Environmental Science & Technology*, 45(15):6460–6467. pages

Kohler, E., Villiger, J., Posch, T., Derlon, N., Shabarova, T., Morgenroth, E., Pernthaler, J., and Blom, J. F. (2014). Biodegradation of microcystins during gravity-driven membrane (gdm) ultrafiltration. *PLOS ONE*, 9(11):e111794. pages

Kone, T., Golfier, F., Orgogozo, L., Oltéan, C., Lefèvre, E., Block, J. C., and Buès, M. A. (2014). Impact of biofilm-induced heterogeneities on solute transport in porous media. *Water Resources Research*, 50(11):9103–9119. pages

Lappin-Scott, H. M., Cusack, F., and Costerton, J. W. (1988). Nutrient resuscitation and growth of starved cells in sandstone cores: a novel approach to enhanced oil recovery. *Applied and Environmental Microbiology*, 54(6):1373–1382. pages

Le Borgne, T., Bolster, D., Dentz, M., de Anna, P., and Tartakovsky, A. (2011a). Effective pore-scale dispersion upscaling with a correlated continuous time random walk approach. *Water Resources Research*, 47(12). pages

Le Borgne, T., Dentz, M., Davy, P., Bolster, D., Carrera, J., de Dreuzy, J.-R., and Bour, O. (2011b). Persistence of incomplete mixing: A key to anomalous transport. *Physical Review E*, 84(1):015301. PRE. pages

Li, L., Benson, C. H., and Lawson, E. M. (2005). Impact of mineral fouling on hydraulic behavior of permeable reactive barriers. *Ground Water*, 43(4):582–596. pages

Luethi, B., Tsinober, A., and Kinzelbach, W. (2005). Lagrangian measurement of vorticity dynamics in turbulent flow. *Journal of Fluid Mechanics*, 528:87–118. pages

MacLeod, F. A., Lappin-Scott, H. M., and Costerton, J. W. (1988). Plugging of a model rock system by using starved bacteria. *Applied and Environmental Microbiology*, 54(6):1365–1372. pages

Mah, T.-F., Pitts, B., Pellock, B., Walker, G. C., Stewart, P. S., and O'Toole, G. A. (2003). A genetic basis for pseudomonas aeruginosa biofilm antibiotic resistance. *Nature*, 426(6964):306–310. 10.1038/nature02122. pages

Martin, K. J. and Nerenberg, R. (2012). The membrane biofilm reactor (mbfr) for water and wastewater treatment: Principles, applications, and recent developments. *Bioresource Technology*, 122(0):83–94. pages

Marty, A., Roques, C., Causserand, C., and Bacchin, P. (2012). Formation of bacterial streamers during filtration in microfluidic systems. *Biofouling*, 28(6):551–562. pages

Matyka, M., Gołembiewski, J., and Koza, Z. (2016). Power-exponential velocity distributions in disordered porous media. *Physical Review E*, 93(1):013110. PRE. pages

Meckenstock, R. U., Elsner, M., Griebler, C., Lueders, T., Stumpp, C., Aamand, J., Agathos, S. N., Albrechtsen, H.-J., Bastiaens, L., Bjerg, P. L., Boon, N., Dejonghe, W., Huang, W. E., Schmidt, S. I., Smolders, E., Sørensen, S. R., Springael, D., and van Breukelen, B. M. (2015). Biodegradation: Updating the concepts of control for microbial cleanup in contaminated aquifers. *Environmental Science and Technology*, 49(12):7073–7081. pages

Michalec, F.-G., Souissi, S., and Holzner, M. (2015). Turbulence triggers vigorous swimming but hinders motion strategy in planktonic copepods. *Journal of The Royal Society Interface*, 12(106). pages

Milferstedt, K., Pons, M. N., and Morgenroth, E. (2009). Analyzing characteristic length scales in biofilm structures. *Biotechnology and Bioengineering*, 102(2):368–379. pages

Mitchell, A. C., Phillips, A., Schultz, L., Parks, S., Spangler, L., Cunningham, A. B., and Gerlach, R. (2013). Microbial caco3 mineral formation and stability in an experimentally simulated high pressure saline aquifer with supercritical co2. *International Journal of Greenhouse Gas Control*, 15:86–96. pages

Morales, V. L., Dentz, M., Willmann, M., and Holzner, M. (2017). Stochastic dynamics of intermittent pore-scale particle motion in three–dimensional porous media: Experiments and theory. *Geophysical Research Letters*, pages n/a–n/a. pages

Morgenroth, E. and Milferstedt, K. (2009). Biofilm engineering: linking biofilm development at different length and time scales. *Reviews in Environmental Science and Bio/Technology*, 8(3):203–208. pages

Moroni, M. and Cushman, J. H. (2001). Statistical mechanics with three-dimensional particle tracking velocimetry experiments in the study of anomalous dispersion. ii. experiments. *Physics of Fluids (1994-present)*, 13(1):81–91. pages

Neu, T. R., Swerhone, G. D. W., and Lawrence, J. R. (2001). Assessment of lectin-binding analysis for in situ detection of glycoconjugates in biofilm systems. *Microbiology*, 147(2):299–313. pages

Neuman, S. P. and Tartakovsky, D. M. (2009). Perspective on theories of non-fickian transport in heterogeneous media. *Advances in Water Resources*, 32(5):670–680. pages

Oh, S. T., Kim, J. R., Premier, G. C., Lee, T. H., Kim, C., and Sloan, W. T. (2010). Sustainable wastewater treatment: How might microbial fuel cells contribute. *Biotechnology Advances*, 28(6):871–881. pages

Or, D., Smets, B. F., Wraith, J. M., Dechesne, A., and Friedman, S. P. (2007). Physical constraints affecting bacterial habitats and activity in unsaturated porous media – a review. *Advances in Water Resources*, 30(6):1505–1527. pages

Orgogozo, L., Golfier, F., Buès, M., and Quintard, M. (2010). Upscaling of transport processes in porous media with biofilms in non-equilibrium conditions. *Advances in Water Resources*, 33(5):585–600. pages

Picioreanu, C., Kreft, J.-U., and van Loosdrecht, M. C. M. (2004). Particle-based multidimensional multispecies biofilm model. *Applied and Environmental Microbiology*, 70(5):3024–3040. pages

Picioreanu, C., van Loosdrecht, M. C. M., and Heijnen, J. J. (1998). Mathematical modeling of biofilm structure with a hybrid differential-discrete cellular automaton approach. *Biotechnology and Bioengineering*, 58(1):101–116. pages

Picioreanu, C., Vrouwenvelder, J. S., and van Loosdrecht, M. C. M. (2009). Three-dimensional modeling of biofouling and fluid dynamics in feed spacer channels of membrane devices. *Journal of Membrane Science*, 345(1–2):340–354. pages

Pintelon, T. R. R., Graf von der Schulenburg, D. A., and Johns, M. L. (2009). Towards optimum permeability reduction in porous media using biofilm growth simulations. *Biotechnology and Bioengineering*, 103(4):767–779. pages

Pérez-Reche, F. J., Taraskin, S. N., Otten, W., Viana, M. P., Costa, L. d. F., and Gilligan, C. A. (2012). Prominent effect of soil network heterogeneity on microbial invasion. *Physical Review Letters*, 109(9):098102. PRL. pages

Qian, J., Horn, H., Tarchitzky, J., Chen, Y., Katz, S., and Wagner, M. (2017). Water quality and daily temperature cycle affect biofilm formation in drip irrigation devices revealed by optical coherence tomography. *Biofouling*, 33(3):211–221. pages

Rolland du Roscoat, S., Martins, J. M. F., Séchet, P., Vince, E., Latil, P., and Geindreau, C. (2014). Application of synchrotron x-ray microtomography for visualizing bacterial biofilms 3d microstructure in porous media. *Biotechnology and Bioengineering*, 111(6):1265–1271. pages

Rusconi, R., Guasto, J. S., and Stocker, R. (2014). Bacterial transport suppressed by fluid shear. *Nat Phys*, 10(3):212–217. pages

Rusconi, R., Lecuyer, S., Autrusson, N., Guglielmini, L., and Stone, H. (2011). Secondary flow as a mechanism for the formation of biofilm streamers. *Biophysical Journal*, 100(6):1392–1399. pages

Rusconi, R., Lecuyer, S., Guglielmini, L., and Stone, H. A. (2010). Laminar flow around corners triggers the formation of biofilm streamers. *Journal of The Royal Society Interface*, 7(50):1293–1299. pages

Saha, D., Soos, M., Lüthi, B., Holzner, M., Liberzon, A., Babler, M. U., and Kinzelbach, W. (2014). Experimental characterization of breakage rate of colloidal aggregates in axisymmetric extensional flow. *Langmuir*, 30(48):14385–14395. pages

Schmidt, L., Fouxon, I., Krug, D., van Reeuwijk, M., and Holzner, M. (2016). Clustering of particles in turbulence due to phoresis. *Physical Review E*, 93(6):063110. PRE. pages

Seki, K., Thullner, M., Hanada, J., and Miyazaki, T. (2006). Moderate bioclogging leading to preferential flow paths in biobarriers. *Ground Water Monitoring and Remediation*, 26(3):68–76. pages

Seymour, J. D., Gage, J. P., Codd, S. L., and Gerlach, R. (2004). Anomalous fluid transport in porous media induced by biofilm growth. *Physical Review Letters*, 93(19):198103. pages

Seymour, J. D., Gage, J. P., Codd, S. L., and Gerlach, R. (2007). Magnetic resonance microscopy of biofouling induced scale dependent transport in porous media. *Advances in Water Resources*, 30(6–7):1408–1420. pages

Sharp, R. R., Cunningham, A. B., Komlos, J., and Billmayer, J. (1999). Observation of thick biofilm accumulation and structure in porous media and corresponding hydrodynamic and mass transfer effects. *Water Science and Technology*, 39(7):195. pages

Stewart, P. S. (2014). Biophysics of biofilm infection. *Pathogens and Disease*, 70(3):212–218. pages

Stewart, P. S. and Franklin, M. J. (2008). Physiological heterogeneity in biofilms. *Nat Rev Micro*, 6(3):199–210. pages

Stoodley, P., deBeer, D., and Lewandowski, Z. (1994). Liquid flow in biofilm systems. *Applied and Environmental Microbiology*, 60(8):2711–2716. pages

Taylor, S. and Jaffé, P. (1990). Biofilm growth and the related changes in the physical properties of a porous medium: 1. experimental investigation. *Water Resources Research*, 26(9):2153–2159. pages

Van Loosdrecht, M. C. M., Picioreanu, C., and Heijnen, J. J. (1997). A more unifying hypothesis for biofilm structures. *FEMS Microbiology Ecology*, 24(2):181–183. pages

Vayenas, D. V., Michalopoulou, E., Constantinides, G. N., Pavlou, S., and Payatakes, A. C. (2002). Visualization experiments of biodegradation in porous media and calculation of the biodegradation rate. *Advances in Water Resources*, 25(2):203–219. pages

Vignaga, E., Sloan, D. M., Luo, X., Haynes, H., Phoenix, V. R., and Sloan, W. T. (2013). Erosion of biofilm-bound fluvial sediments. *Nature Geosci*, 6(9):770–774. pages

Vogt, S. J., Sanderlin, A. B., Seymour, J. D., and Codd, S. L. (2013). Permeability of a growing biofilm in a porous media fluid flow analyzed by magnetic resonance displacement-relaxation correlations. *Biotechnology and Bioengineering*, 110(5):1366–1375. pages

von der Schulenburg, D. A. G., Pintelon, T. R. R., Picioreanu, C., Van Loosdrecht, M. C. M., and Johns, M. L. (2009). Three-dimensional simulations of biofilm growth in porous media. *AIChE Journal*, 55(2):494–504. pages

Wagner, M. and Horn, H. (2017). Optical coherence tomography in biofilm research: A comprehensive review. *Biotechnology and Bioengineering*, 114(7):1386–1402. pages

Wagner, M., Ivleva, N. P., Haisch, C., Niessner, R., and Horn, H. (2009). Combined use of confocal laser scanning microscopy (clsm) and raman microscopy (rm): Investigations on eps – matrix. *Water Research*, 43(1):63–76. pages

Wagner, M., Manz, B., Volke, F., Neu, T. R., and Horn, H. (2010a). Online assessment of biofilm development, sloughing and forced detachment in tube reactor by means of magnetic resonance microscopy. *Biotechnology and Bioengineering*, 107(1):172–181. pages

Wagner, M., Taherzadeh, D., Haisch, C., and Horn, H. (2010b). Investigation of the mesoscale structure and volumetric features of biofilms using optical coherence tomography. *Biotechnology and Bioengineering*, 107(5):844–853. pages

West, S., Wagner, M., Engelke, C., and Horn, H. (2016). Optical coherence tomography for the in situ three-dimensional visualization and quantification of feed spacer channel fouling in reverse osmosis membrane modules. *Journal of Membrane Science*, 498:345–352. pages

Westall, F., de Wit, M. J., Dann, J., van der Gaast, S., de Ronde, C. E. J., and Gerneke, D. (2001). Early archean fossil bacteria and biofilms in hydrothermally-influenced sediments from the barberton greenstone belt, south africa. *Precambrian Research*, 106(1):93–116. pages

Wildenschild, D. and Sheppard, A. P. (2013). X-ray imaging and analysis techniques for quantifying pore-scale structure and processes in subsurface porous medium systems. *Advances in Water Resources*, 51:217–246. pages

Wildenschild, D., Vaz, C. M. P., Rivers, M. L., Rikard, D., and Christensen, B. S. B. (2002). Using x-ray computed tomography in hydrology: systems, resolutions, and limitations. *Journal of Hydrology*, 267(3–4):285–297. pages

Yawata, Y., Nguyen, J., Stocker, R., and Rusconi, R. (2016). Microfluidic studies of biofilm formation in dynamic environments. *Journal of Bacteriology.* pages

Chapter 2

Pores-scale hydrodynamics in a progressively bio-clogged three-dimensional porous medium: 3D particle tracking experiments and stochastic transport modeling

This chapter consists of a manuscript submitted to: Water Resources Research

M. Carrel^{a,b,c,d}, V. Morales^{a,b,c,e}, M. Dentz^{b,c,e}, N. Derlon^{a,e}, E. Morgenroth^{a,e} and M. Holzner^{a,c,e}. Pore-scale hydrodynamics in a progressively bio-clogged three-dimensional porous medium: 3D particle tracking experiments and stochastic transport modeling.

^{a} Study concept and design; ^{b} Data acquisition and analysis; ^{c} Interpretation of data; ^{d} Developing the theoretical concept; ^{e} Drafting manuscript; ^{f} Critical revision

Abstract

Biofilms are ubiquitous bacterial communities growing in various porous media including soils, trickling and sand filters where they play a central role in services ranging from degradation of pollutants to water purification. They dynamically change the pore structure of the medium through selective clogging of pores, a process known as bioclogging.

This affects how solutes are transported and spread through the porous matrix, but the temporal changes to transport behavior during bioclogging are not well understood. To address this uncertainty, we experimentally study the hydrodynamic changes of a transparent 3D porous medium as it experiences progressive bioclogging. Statistical analysis of the system's hydrodynamics at four time points of bioclogging (0, 24, 36 and 48 hrs in the exponential growth phase) reveals exponential increases in both average and variance of the flow velocity, as well as its correlation length. Measurements for spreading, as mean-square displacements, are found to be non-Fickian and more intensely superdiffusive with progressive bioclogging, indicating the formation of preferential flow pathways and stagnation zones. A gamma distribution describes well the Lagrangian velocity distributions and provides a parametrization for the changing flow, which evolves from a parallel pore arrangement under unclogged conditions, toward more serial with increasing clogging. Exponentially evolving hydrodynamic metrics agree with the bacterial growth phase, and are used to parametrize a correlated continuous time random walk model with a stochastic velocity relaxation. The model accurately reproduces transport observations and can be used to resolve transport behavior at intermediate time points within the exponential growth phase considered.

2.1 Introduction

Porous media flows are strongly affected by the ubiquitous structural heterogeneities of porous networks consisting in wide distributions of pore sizes and length scales inducing non-Gaussian or anomalous transport. This phenomenon is characterized by incomplete mixing or enhanced spreading persistently spanning from the pore to the field scale (Berkowitz et al., 2000; Gouze et al., 2008; Le Borgne and Gouze, 2008; Dentz et al., 2011; Le Borgne et al., 2011b; Edery et al., 2014). At the pore-scale, anomalous transport exhibits many different characteristics such as non-Gaussian velocity distributions (Bijeljic et al., 2013; Matyka et al., 2016), high temporal correlation of Lagrangian velocities forming a spatial Markov process (Le Borgne et al., 2011a), intermittency of velocities along trajectories (de Anna et al., 2013) or super-diffusive spreading of advected particles (Kang et al., 2014; Holzner et al., 2015). The intensity of the anomalous transport is related to the heterogeneity of the porous medium and was investigated in media of different complexity ranging from simple beadpacks to fractured sandstones and carbonates (Bijeljic et al., 2013; Siena et al., 2014; Meyer and Bijeljic, 2016; Morales et al., 20).

The distributions of pore sizes and lengths scales present in porous media can have a dynamic component driven by biological or physico-chemical processes such as the development of bacterial biofilms (Stoodley et al., 1994; Seymour et al., 2004, 2007), mineral dissolution and precipitation (Daccord and Lenormand, 1987; Noiriel et al., 2013; Menke et al., 2015; Linga et al., 2017) or gas exchange for multiphase flows (Klump et al., 2007; Datta et al., 2013; Kazemifar et al., 2016; Jiménez-Martínez et al., 2016). The resulting structural changes (e.g. porosity and connectivity changes) influence the pore-scale hydrodynamics (e.g. pore-scale velocity distributions) and alter the system's anomalous transport intensity. In this work, we focus on the clogging of pores by bacterial biofilms. These sessile bacterial communities are of interest due to the ubiquitous presence of in natural or industrial systems (Costerton et al., 1999; Hall-Stoodley et al., 2004) and are relevant for various applications involving porous media flows such as bioremediation (Bouwer and Zehnder, 1993) and microbial enhanced oil recovery (Head et al., 2003; Lazar et al., 2007), trickling and sand filters (Gujer and Boller, 1986; Leverenz et al., 2009) or artificial groundwater recharge (Rubol et al., 2014).

Many different numerical or experimental approaches have been used to investigate the growth of biofilms in porous media. Biofilms were shown to change pore networks, so that the growth of tenuous biofilm patches could reduce pore sizes, thus significantly influencing the flow field (Coyte et al., 2017). Biofilms were experimentally (Seki et al., 2006; Durham et al., 2012; Nadell et al., 2017) and numerically (Pintelon et al., 2009; Bottero et al., 2013) observed to induce the formation of preferential flow pathways and stagnation zones in two-dimensional (2D) systems. Numerically, von der Schulenburg et al. (2009) combined a lattice Boltzmann simulation with an individual-based biofilm model to investigate the growth of biofilms in a 3D porous media. By comparing 2D and 3D results, the authors underlined the necessity of considering three-dimensional systems, as the results in 2D or 3D differed substantially. For instance, they showed that the variance of velocity distributions increased more slowly in 3D than in 2D and the formation of preferential flow pathways was strongly delayed in 3D, warranting experimental data to corroborate the findings. Ultimately, biofilms were shown to cause an increase of non-Fickian transport dynamics (Seymour et al., 2004, 2007; Knecht et al., 2011; Kone et al., 2014). The pioneering work by Seymour et al. (2004) revealed a transition from Gaussian to non-Gaussian transport dynamics due to biofilm development in a homogeneous beadpack. Thereby, the authors used magnetic resonance microscopy to quantify the evolution of propagators (i.e. displacement probability density functions). The transition of the propagators was then modeled qualitatively for different degrees of bioclogging using a conceptual continuous time random walk based on a power law Lévy wait time and a Gaussian jump length distributions. However, this approach does not honor the temporal correlation of the intermittent pore-scale flow, thus not accounting for the spatial Markovian nature of porous media flows which was recently shown to be an essential ingredient for accurate transport modeling (de Anna et al., 2013). The importance of this temporal correlation is expected to increase with the heterogeneity induced by increasing bioclogging (Le Borgne et al., 2011a).

The goal of this study is to experimentally quantify the influence of biofilm growth on pore-scale hydrodynamics to better understand and model flow and transport processes in bioclogged systems. 3D Particle tracking velocimetry is first used to determine the velocity distribution, mean square displacement and particle displacement distributions of transport behavior at different bioclogging stages. Then, the hydrodynamic quantities are statistically analyzed and their temporal evolution linked to expected trends of biofilm growth. Lastly, these quantities are used to parametrize a correlated continuous time random walk model that accurately captures transport observations and quantifies flow transition from uniform to preferential.

2.2 Material and Methods

2.2.1 Porous Media and Working Fluid

The porous medium used in this study consisted of Nafion pellets (NR50 1100 EW, Ion Power, Munich, Germany) of diameter $d_N \approx 2.5\ mm$, with similar physico-chemical properties to that of sand grains (Downie et al., 2012). The refractive index of the nafion pellets was matched with a 11% w/v glucose aqueous solution. The optimal glucose concentration was defined using a protocol similar to the one presented by Downie et al. (2012). To enhance bacterial growth, we ensured the solution was saturated with oxygen and further nutrients (nitrogen, phosphorus) and electron acceptors were added ($NaNO_3$, K_2HPO_4 and $NaH_2PO_4{\cdot}2(H_2O)$) resulting in an influent with C:N:P molecular ratio of 1000:1:1. In order to optimize the refractive index matching, ca. 20 g of the nafion pellets used were heated up in 250 mL of the glucose solution to 65 °C for one hour and cooled in a fresh solution overnight. This cycle was repeated three times.

2.2.2 Biofilm Growth and Hydrodynamic Conditions

The bacterial inoculum used in this study was isolated from river water samples. Frozen bacterial stock contained in 2 mL Eppendorf tubes was added to 100 mL of the growth medium incubated for 20-24 h at 30°and stirred at 200 rpm until reaching midlogarithmic phase (OD_{600} 0.52 ± 0.096). Subsequently, 10 mL of the inoculum were added to 90 mL of fresh growth medium. This incubation procedure was repeated three times for the bacteria to adapt to the synthetic carbon source of the growth medium. An effective exponential growth rate of 0.097 ± 0.012 1/h was measured by considering the OD_{600} (0.0505 ± 0.011) initially and once midlogarithmic phase was reached. The nafion grains prepared following the protocol described above were added to the inoculum for the last incubation cycle to allow initial bacterial attachment. A custom-built PMMA flow cell with point inlet and oulet (inner dimensions: 38x38x16 mm^3) was wet-packed with the prepared Nafion grains.

A biofilm was cultivated in the flow cell for 48 h under a constant volumetric flow rate (10 mL/min, corresponding to an initial average residence time of ca. 40 s) set with a peristaltic pump (Ismatec, Glattbrugg, Switzerland). At this flow rate, the initial Darcy velocity q was of 0.274 mm/s and the effective porosity of $\phi = 0.27$, yielding an average interstitial pore velocity $v_p = q/\phi$ of ≈ 1 mm/s and corresponding initial Reynolds number $Re = v_p d_N/\nu \approx 0.5$. After biofilm growth, threefold increase in v_p results in an Re increase to ≈ 1.5, which is still within Darcy's law validity range ($Re \leq 10$). In this system, the Péclet number defined as the ratio between the advective and diffusive and transport rates v_p and D_{H2O}/d_N, $Pe = \frac{v_p d_N}{D_{H2O}} \approx 2500$ with D_{H2O} the molecular diffusion coefficient of water.

2.2.3 3D-PTV Measurements

In this work, 3D-PTV measurements were performed in a refractive index matched (RIM) (Budwig, 1994) porous medium to characterize the evolution of pore-scale hydrodynamics during biofilm growth. The open source 3D-PTV code employed here allows to characterize flows by providing position, velocity and acceleration of tracer particles along trajectories ((Lüthi et al., 2005; Hoyer et al., 2005; Gülan et al., 2012; Holzner et al., 2015; Michalec et al., 2015; Schmidt et al., 2016)). 3D-PTV was used to perform measurements over the course of the biofilm growth, providing a quantitative description of the influence of biofilm growth on flow and transport.

Three-dimensional particle tracking velocimetry (3D-PTV) measurements were performed at the time points T = 0, 24, 36 and 48 h of biofilm culturing. To perform the 3D-PTV measurements, a syringe connected to the flow cell was mounted on a syringe pump (Lambda Vit-Fit, Lambda, Baar, Switzerland). Fluorescent tracer particles (Red Polyethylene Microspheres, Cospheric, Santa Barbara, CA USA) of diameter $d_P \approx 70\ \mu m$ and density $\rho_P = 0.995$ g/cm^3, thus neutrally buoyant (Stokes number $Stk \ll 1$), were seeded to the flow and tracked in time and 3D space with 3D-PTV. The Péclet number of the particles can be considered to be infinite due to the size of the particle and their corresponding negligible diffusion coefficient. The tracer particle concentration was of 0.02 g/L (volume fraction concentration ≈ 0.002 %) and 0.2 ppm of surfactant (Tween, Cospheric, Santa Barbara, USA) was added to the fluid to prevent particle agglomeration during the 3D-PTV measurements. Note that the tracer particles are too large to enter the sub-micrometer sized inner biofilm channels (Stoodley et al., 1994; Carrel et al., 2017) and that the particle to nafion pellet diameter ratio d_N/d_P is of ca. 35. Thus, the porosity reduction of the porous medium due to interception of the tracer particles can be considered to be insignificant (Sakthivadivel and Einstein, 1970; Yao et al., 1971). Additionally, due to the extremely low volume fraction concentration, particle-particle interactions can be neglected.

The particles were then illuminated with a 100 W pulsed Nd-YLF laser (Darwin Duo, Quantronix, Hamden, USA). Images were acquired with a Photron Fastcam SA5 at 50 Hz with 1 Mega pixel resolution. An image splitter was used in order to mimic a four camera system. A redundant 4 views system allowed particle recognition and tracking (Maas et al., 1993; Malik et al., 1993; Lüthi et al., 2005) in the progressively bioclogged system. Before the tracking, a pre-processing step consisting of a running image substraction with a lag of 50 images and a high pass filter were applied in order to improve each image signal to noise ratio. Subsequent tracking of the particles in 6D position-velocity space allowed to connect segments of interrupted Lagrangian trajectories (Haitao, 2008). A Savitzky-Golay filter was then implemented in order to smooth trajectories (Saha et al., 2014). The final sub-pixel accuracy of the particles positions along trajectories was of about 50 μm (Holzner et al., 2015). Short or immobile trajectories with length smaller than 21 frames resp. total displacement shorter than 1 mm were discarded, finally yielding more than $O(10^3)$ trajectories for every 3D-PTV measurement time point in the bioclogged porous medium (4465, 3604, 1953 and 2660 for the time points T = 0, 24, 36 and 48 h respectively). In the course of the experiment, the growing biofilm increasingly attenuated the signal emitted by the tracer particles. The experiment was stopped after 48 h of biofilm growth, as tracer particles could be detected well only up to 50 % of the flow cell depth. In order to compensate for the increasing light attenuation and to image particle tracers over the whole flow cell depth, images were consecutively acquired from both front and back sides of the flow cell. Over the course of the experiment, the average trajectory length remained relatively constant at around 25 % of the total flow cell length (26, 28, 33 and 22 % for the time points T = 0, 24, 36 and 48 h respectively) and the RIM quality stayed constant upon biofilm growth. Finally in order to account for entry effects due to the point inlet, the first advective time scale of the trajectories $\tau_A = \lambda_i/\langle v \rangle$, with λ_i a representative length scale and $\langle v \rangle$ the average velocity (see Table 2.1), was discarded.

2.3 Results

2.3.1 Experimental pore-scale characterization of the progressive bio-clogging

Figure 2.1 shows photographs of the flow cell during biofilm culturing (top) after 0, 36 and 48 h. The photographs illustrate how the biofilm progressively develops in the flow cell. Note that the transparency of the flow cell decreases with biofilm growth. On the bottom part of Figure 2.1, frontal projections of 3D-trajectories (more than 10^6 data points for each case) color-coded with the logarithm of the norm of the velocity vector showing the influence of the progressive bio-clogging on the Lagrangian flow field.

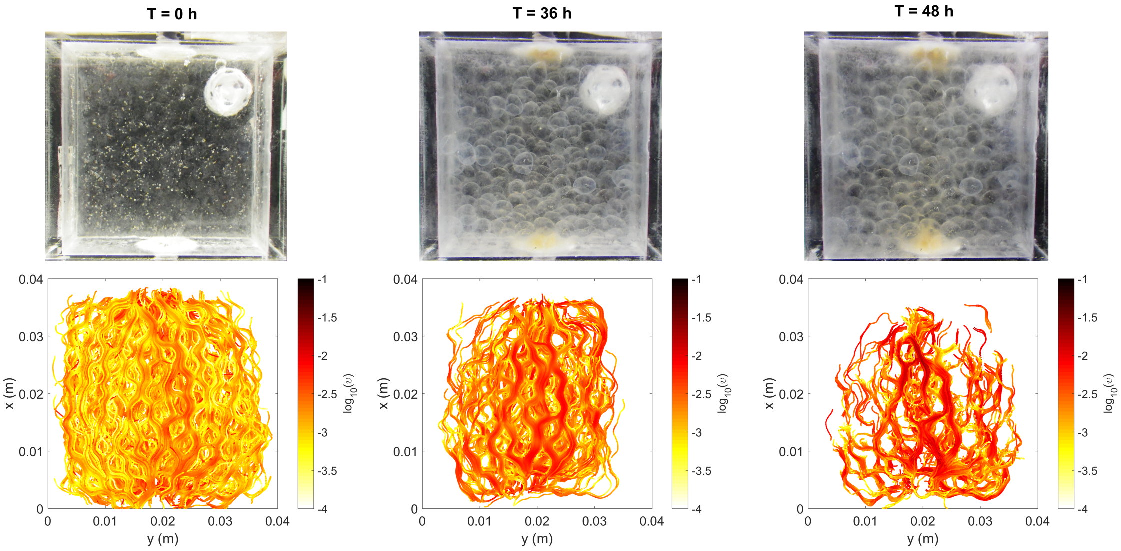

Figure 2.1: Photographs illustrating progressive changes in the porous media with increasing bio-clogging of the flow cell (top) and particle trajectories obtained by 3D-PTV (bottom) for the time points T = 0, 36 and 48 h. The bright spot in the upper right corner of the photographs is a reflection by a teflon-coated plastic screw that is used to close the opening of the flow cell. The trajectories are color-coded with the logarithm of the norm of the velocity vector.

The trajectories display intermittent Lagrangian velocities inherent to fluid flows in porous media (de Anna et al., 2013; Kang et al., 2014; Holzner et al., 2015; Morales et al., 20), accelerating at pore throats and decelerating at pore bodies(Holzner et al., 2015). The flow cell is operated with a constant flow rate, so that biofilm growth in the system increases the average longitudinal velocity, as illustrated by the increasingly darker color-coding of the trajectories. Note that the photographs and the trajectories are not on the same coordinate space, so that the alignment is just for the sake of visualization and qualitative comparison. As larger amounts of biofilm form in the flow cell, tracer particles are confined to fewer channels in the domain. Mass conservation corroborates such channel formation as it is observed in the ca. 3 fold increase in longitudinal velocity (see table 2.1). Consequently, regions not sampled by the particles can be considered to be stagnation zones occupied by biofilm and not contributing to the flow. With increasing bio-clogging, more of these stagnation zones appear. It is visible qualitatively that these stagnant zones in Fig. 2 (trajectories for T = 48 h) correlate with the opaque bioclogged regions in Fig. 2 (photograph for T = 48 h).

2.3.2 Lagrangian velocity probability density functions

In order to quantitatively investigate the influence of progressive bio-clogging on flow in the porous medium, we first consider probability density functions (PDFs) of isochronic Lagrangian velocities (t-Lagrangian) along the trajectories (Moroni and Cushman, 2001; Moroni et al., 2007; Holzner et al., 2015; Morales et al., 20). Under ergodic conditions and for incompressible flow, the t-Lagrangian velocity PDF is equivalent to the Eulerian velocity PDF (Dentz et al., 2016). The PDFs of t-Lagrangian velocities $P_t(v)$ are obtained by

$$P_t(v) = \frac{1}{N_p} \sum_{i=1}^{N_p} \frac{1}{T_i} \int_0^{T_i} dt \frac{\mathbb{I}[v \leq v(t; \mathbf{a}_i) < v + \Delta v]}{\Delta v}, \tag{2.1}$$

where N_p is the number of trajectories, $\mathbf{a}_i$ the initial point of the ith trajectory, T_i is its duration; $v(t; \mathbf{a}_i)$ denotes either the longitudinal or transverse components of the particle velocity $\mathbf{v}(t; \mathbf{a}_i)$ or its magnitude, and Δv the sampling interval.

The PDFs of the t-Lagrangian velocities in longitudinal and transverse directions as well as for the velocity magnitude for the four time points during biofilm growth are illustrated in Figure 2.2 (a) and (b). As listed in Table 2.1, upon biofilm growth and subsequent porosity reduction, the average velocity in the system increases due to fluid mass conservation.

As Figure 2.2 (a) and (b) show, the PDFs of the longitudinal velocity component and of the velocity magnitude exhibit substantial increase in variance and tailing heftiness. The variance increase of the velocity magnitude (see σ_v^2 in Table 2.1) reflects the formation of preferential flow paths of high velocities, as the variance σ_v^2 is dominated by the contribution of velocities much higher than the mean $\langle v \rangle$. Therefore, we also report the variance of the natural logarithm of the velocity (see $\sigma_{ln(v)}^2$ in Table 2.1) whose increase confirms the formation of zones of almost stagnant, slow velocities.

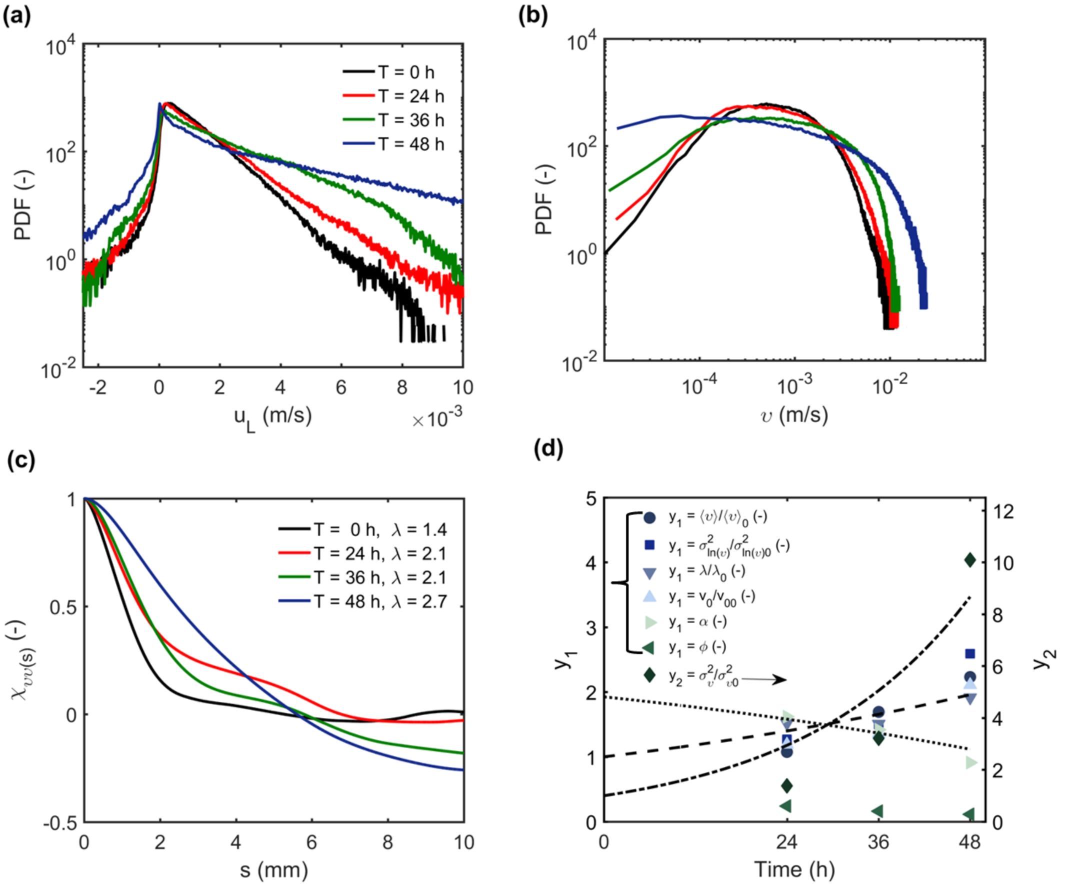

Figure 2.2: Probability density functions of the t-Lagrangian (a) longitudinal velocity component and (b) magnitude obtained at different time points. (c) shows the auto-correlation function of the velocity magnitude, indicating the corresponding correlation lengths in the legend. (d) illustrates the temporal evolution of the average velocity $\langle \upsilon \rangle$, the variance of the natural logarithm of the velocity $\sigma^2_{ln(\upsilon)}$, the correlation length λ, and of the characteristic velocity υ_0, as normalized by their value at the time point T = 0 h. The dashed line shows an exponential fit with growth rate $\mu = 0.015$ h^{-1}. The evolution of α (with dotted line representing the corresponding exponential fit with $\mu_\alpha = 0.012$ h^{-1}) and of the porosity ϕ are illustrated on the same y-axis. The evolution of the normalized velocity variance $\sigma^2_\upsilon/\sigma^2_{\upsilon 0}$ is shown on the secondary y-axis (with the dashed-dotted line showing the corresponding fit, $\mu_{\sigma^2_\upsilon} = 0.045$ h^{-1}).

2.3.3 Velocity auto-correlation functions

The spatial auto-correlation length of Lagrangian velocities has previously been identified to reflect the spatial Markovian nature of flows in porous media (Le Borgne et al.,

Table 2.1: Average velocity magnitude$\langle v\rangle$, velocity magnitude variance σ_v^2, correlation length scale λ of the t-Lagrangian velocity magnitudes, as well as scale parameter v_0 expressing a characteristic velocity, shape parameter α informing the system connectivity for all time points T = 0, 24, 36 and 48 h. μ_i is the exponential coefficient and R_i^2 is the coefficient of determination for the exponential change in time of the listed hydrodynamic parameters.

	T = 0 (h)	T = 24 (h)	T = 36 (h)	T = 48 (h)	μ_i (1/h)	R_i^2
$\langle v\rangle$ (mm/s)	1.3	1.4	2.2	2.9	0.015	0.85
σ_v^2 ($\mathrm{m}^2/\mathrm{s}^2$)	9.82E-07	1.35E-06	3.16E-06	9.91E-06	0.045	0.86
$\sigma_{ln(v)}^2$ (-)	0.651	0.825	0.975	1.686	0.017	0.81
λ (mm)	1.38	2.1	2.1	2.7	0.013	0.92
v_0 (-)	0.518	0.616	0.705	1.093	0.013	0.79
α (-)	1.929	1.619	1.418	0.914	0.012	0.95
ϕ (-)	0.27	0.24	0.19	0.12	-	-
Δs (mm)	0.0138	0.021	0.021	0.027	-	-

2008). We therefore determine the Lagrangian velocity magnitude auto-correlations during progressive bioclogging. An increase in spatial correlation is indicative of persistent fast velocities along trajectories, and suggests the formation of preferential flow paths. The auto-correlation functions of the s-Lagrangian velocity magnitude $v_s(s;\mathbf{a})$ (Dentz et al., 2016) sampled equidistantly along a trajectory are defined as:

$$\chi_{vv}(\Delta s) = \frac{\sum\limits_{i=1}^{N_p} R_{vv}(\Delta s;\mathbf{a}_i)}{\sum\limits_{i=1}^{N_p} \sigma_{vv}^2(\mathbf{a}_i)}, \tag{2.2}$$

where the velocity covariance along a single trajectory is defined by

$$R_{vv}(\Delta s;\mathbf{a}_i) = \frac{1}{L_i}\int\limits_0^{L_i} ds\big[v_s(s+\Delta s;\mathbf{a}_i) - \langle v_s(s)\rangle\big]\big[v_s(s;\mathbf{a}_i) - \langle v_s(s+\Delta s)\big]. \tag{2.3}$$

where $v_s(s;\mathbf{a})$ is the velocity magnitude along the trajectory which starts at $\mathbf{a}$, measured in distance s traveled along the trajectory, and L is the length of the trajectory. The velocity variance along the trajectory is given by $\sigma_{vv}^2(\mathbf{a}) = R_{vv}(0;\mathbf{a})$. Finally, the correlation length, λ, is obtained by integration of χ_{vv}.

Figure 2.2 (c) shows the auto-correlation functions of the s-Lagrangian velocity magnitudes obtained from the 3D-PTV measurements for all time points and the corresponding correlation lengths obtained by integration for the different data sets. As these results show (see Figure 2.2 (c) and Table 2.1), the correlation length measured along trajectories increases from approximately $\lambda \approx d_N/2$ to $\lambda \approx d_N$, where $d_N \approx 2.5$ mm is the average nafion pellet diameter.

2.3.4 Approximation of the velocity magnitude with a gamma distribution

Hereinafter, we consider the t-Lagrangian velocity magnitude for all time points presented in Figure 2.2 (b). We find that the PDF of the t-Lagrangian velocity magnitude can be approximated by the following gamma distribution

$$\mathcal{P}(v_t) = \frac{v^{\alpha-1}}{\mathrm{v_0}^{\alpha}\Gamma(\alpha)} e^{\frac{-v}{\mathrm{v_0}}} \tag{2.4}$$

It allows to account for the increasing heterogeneity in the system upon biofilm growth by an evolution of the exponent α (probability weight at low velocities, refer to Table 2.1 for values for each time point) and the scaling parameter $\mathrm{v_0}$ (a characteristic velocity reflecting the increase in the average velocity, refer to Table 2.1 for values at each time point).

Figure 2.3 shows the 3D-PTV velocity magnitudes for all time points and the corresponding gamma distributions with shape and scale parameters estimated by least squares. As listed in Table 2.1, the exponent α which represents the connectivity of the pore network (Holzner et al., 2015) decreases substantially. Holzner et al. (2015) showed based on theoretical considerations that the maximal and minimal values of α were of 2 and -2 for completely serial or parrallel pore arrangements, respectively. The decrease of α observed in Table 2.1 from 1.929 to 0.914 therefore indicates that the structure of the pore network evolves from a predominantly parallel pore arrangement towards a more serial pore arrangement. The characteristic velocity $\mathrm{v_0}$ increases substantially, similar to the average velocity increase upon biofilm growth and the corresponding reduction of the void space.

2.3.5 Temporal evolution of the hydrodynamic quantities

The hydrodynamic quantities presented in Figure 2.2 and Table 2.1 can be approximated by an exponential increase of the type $X(t) = \mathrm{X_0}e^{\mu_i t}$, where X_0 is the value of the considered quantity at the time point T = 0 h and μ_i is the corresponding exponential constant. α follows a decrease according to $\alpha(t) = (\alpha_0 + 1) - e^{\mu_\alpha t}$. Albeit the consideration of only 3 different time points (excluding the initial value which was kept fixed), the coefficients of determination are fairly high ($R_i^2 > 0.75$). It is important to note that, as mentioned above, the porosity ϕ is estimated from the average pore velocity $\langle v \rangle$ by $\langle v \rangle = q/\phi$ where q is the fixed flux. Therefore, the exponential increase of the velocity observed is considered to be directly linked to the biofilm development and simultaneous porosity reduction (see Table 2.1).

2.3.6 Correlated continuous time random walk

In order to investigate the influence of the formation of preferential flow paths and stagnation zones on transport processes, we employ a correlated continuous-time random walk (CTRW) model for the pore-scale particle motion (Le Borgne et al., 2011a; de Anna et al., 2013; Holzner et al., 2015). The CTRW provides an efficient modeling approach for transport in velocity fields that vary over a characteristic length scale (Dentz et al., 2016). As we saw in the previous section, s-Lagrangian particle velocities vary over a correlation scale

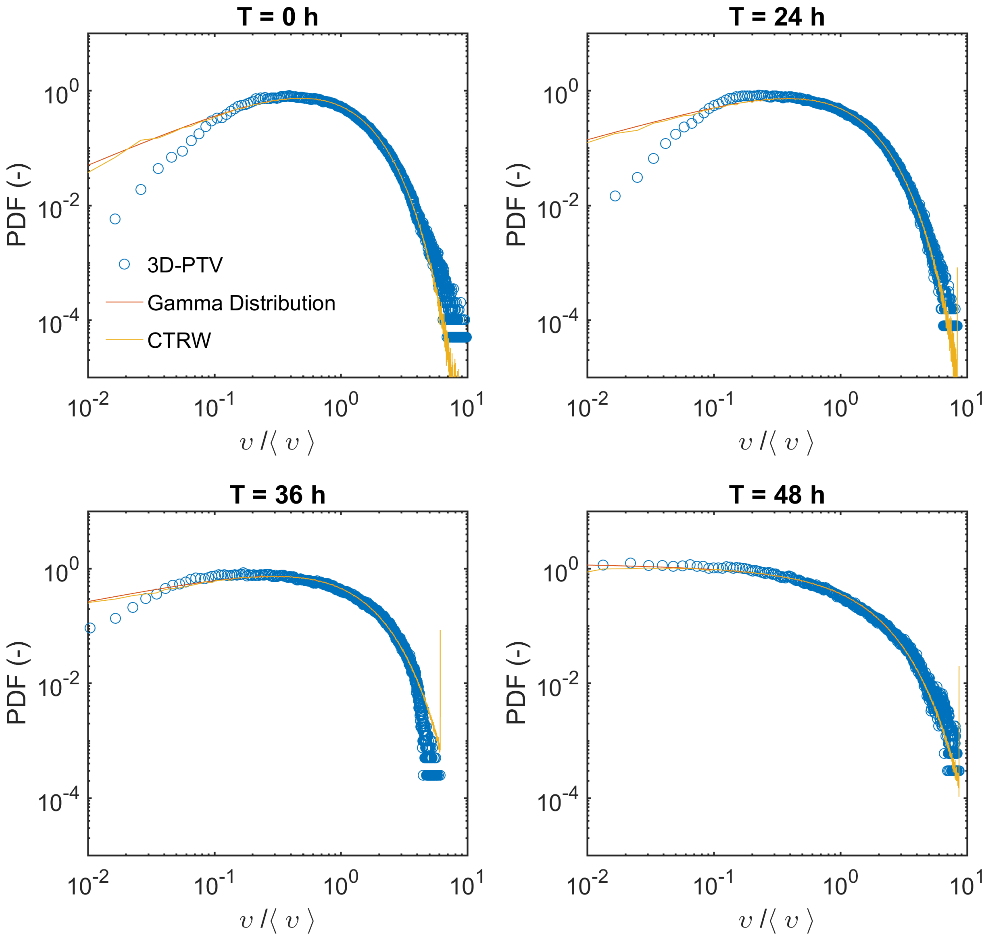

Figure 2.3: Probability density functions of the velocity magnitudes obtained with 3D-PTV, the corresponding MLE gamma distributions and the PDFs of the velocity obtained from the CTRW model for all time points.

λ, or in other words particle velocities persist over the characteristic length scale λ, which changes according to the growth of the biofilm. We assume that the evolution of λ is much slower than the typical particle transport scales. Thus, particle motion is modeled by the recursion relation

$$s_{n+1} = s_n + \Delta s, \qquad t_{n+1} = t_n + \frac{\Delta s}{v_n} \tag{2.5}$$

where $v_n = v_s(s_n)$ and Δs a space increment. The velocity series $\{v_n\}$ is modeled by a stochastic relaxation proces (Dentz et al., 2016) to account for the correlation of velocities inherent to the spatial Markovian nature of flows in porous media (Le Borgne et al., 2008, 2011a; de Anna et al., 2013). The steady state PDF $P_s(v)$ of the spatial Markov chain $\{v_n\}$ is obtained from $P_t(v)$ through flux-weighting as (Dentz et al., 2016)

$$P_s(v) = \frac{vP_t(v)}{\langle v_t \rangle}. \tag{2.6}$$

Particles maintain the same velocity at a turning point after n steps according to a Bernoulli process with persistence probability $p = \exp[-\Delta s'/(2\lambda'_T)]$ and change to a random velocity distributed by $P_s(v)$ according to $1 - p$. The single quotation mark indicates the normalization of the spatial increments Δs (see Table 2.1) and of λ_T by the reference length scale λ_T ($T = 0, 24, 36$ and 48). The persistence of the velocity p over the spatial increments is based on an exponential decorrelation over twice the computed correlation length in order to account for incomplete mixing at pore throats. In the following, particle transport is simulated by Equation 2.5 for the different time points and the corresponding correlation lengths λ_T. The PDFs of the t-Lagrangian velocity magnitude obtained from the correlated CTRW in figure 2.3 show a good agreement with the experimental data and with the fitted gamma distributions.

2.3.7 Displacement statistics

The displacement $s(t)$ at a given time t is given in terms of the CTRW model by $s(t) = s_{n_t}$, where $n_t = \max(n|t_n \leq t)$. We study the mean and centered mean squared displacements

$$m(t) = \langle s(t) \rangle, \qquad \sigma_s^2(t) = \langle s(t)^2 \rangle - m(t)^2, \tag{2.7}$$

obtained from the 3D-PTV data and interpret them in the light of the correlated CTRW model discussed above, which gives some insight into the heterogeneity of the porous medium and the role of biofilm growth for particle dispersion. The angular brackets denote the average over all particles.

Figure 2.4 (a) shows the evolution of the first and second centered displacements moments of the 3D-PTV experimental data and of the CTRW for all time points. The mean displacement is always very well captured by the CTRW model. All experimental mean-squared displacements (MSDs) $\sigma_s^2(t)$ show a transition from a ballistic regime ($\sigma_s^2(t) \propto t^2$) to a superdiffusive regime with a temporal scaling higher ($\sigma_s^2(t) \approx t^{1.5}$) than the expected asymptotic Fickian regime ($\sigma_s^2(t) \propto t$). Here a transition between ballistic and superdiffusive regimes occurs at ca. one advective time scale. Both regimes as well as the transition are captured by the CTRW model. Note the discontinuity and interruption of the experimental data after 5 to 10 advective time scales τ_A due to the finite size of the experimental field of view and of the trajectory lengths. In Figure 2.4, the insets (b) and (c) show the evolution of the mean-squared displacements obtained from the CTRW (b) and a magnification of the superdiffusive regime (c). The vertical shift of the MSDs with progressive bio-clogging is similar throughout ballistic and superdiffusive regimes. For the ballistic regime, the upward shift is due to the increasing variance of the velocity magnitude (see Figure 2.4 (b) or refer to Table 2.1). Interestingly, for the superdiffusive regime, the exponent of these MSDs shows an increase from 1.25 to 1.4 (see Figure 2.4 (c)), indicating

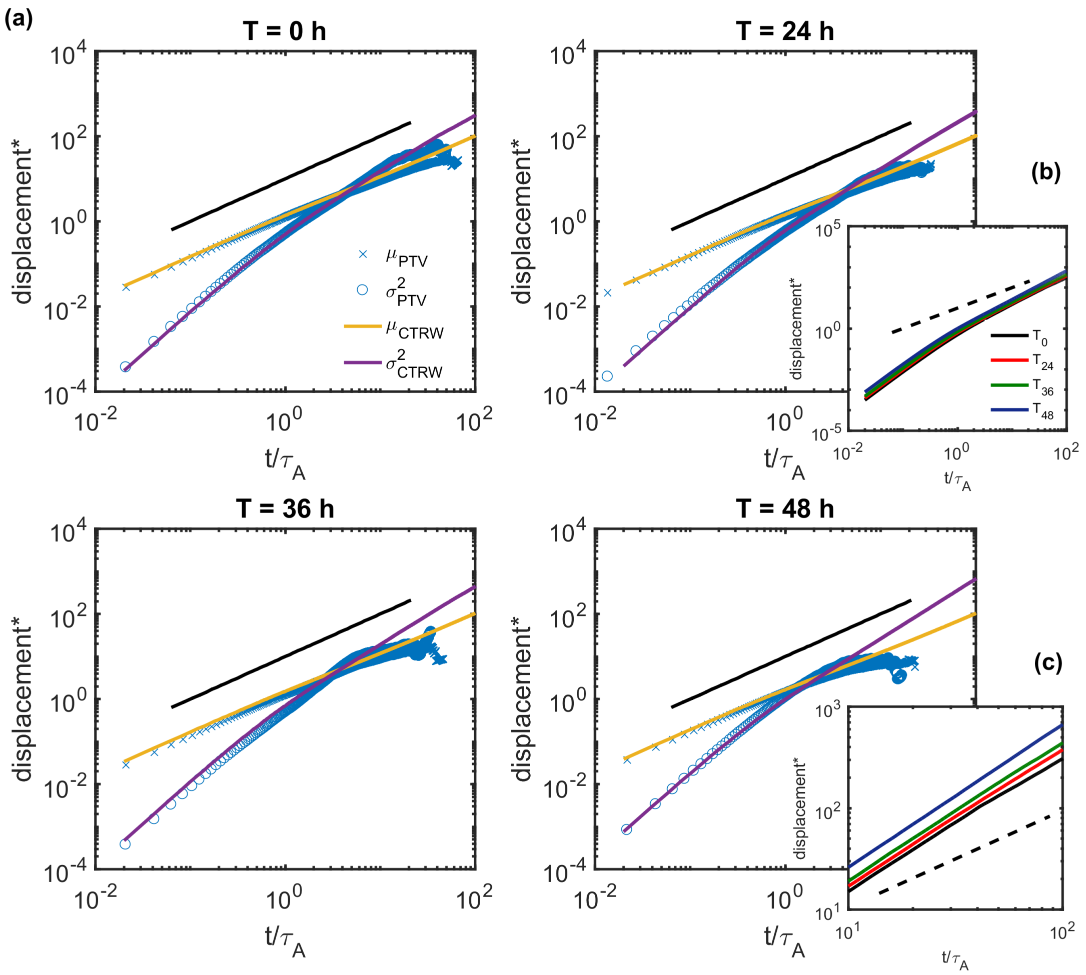

Figure 2.4: (a) Experimental (3D-PTV) and numerical (CTRW) mean m and mean-squared displacements σ^2 obtained for all time points. The spatial moments presented here are dimensionless, as they are rescaled by the corresponding length scales (λ or λ^2). The time is rescaled by the advective time scale τ_A. (b) CTRW mean-squared displacements for all the different time points. (c) Magnification of (b) illustrating a moderate increase in superdiffusive behavior with increasing biofilm growth. The continuous lines in (a) or (b) and (c), respectively, indicate Fickian scaling.

that the formation of preferential flow pathways and stagnation zones upon biofilm growth leads to an increase of anomalous transport.

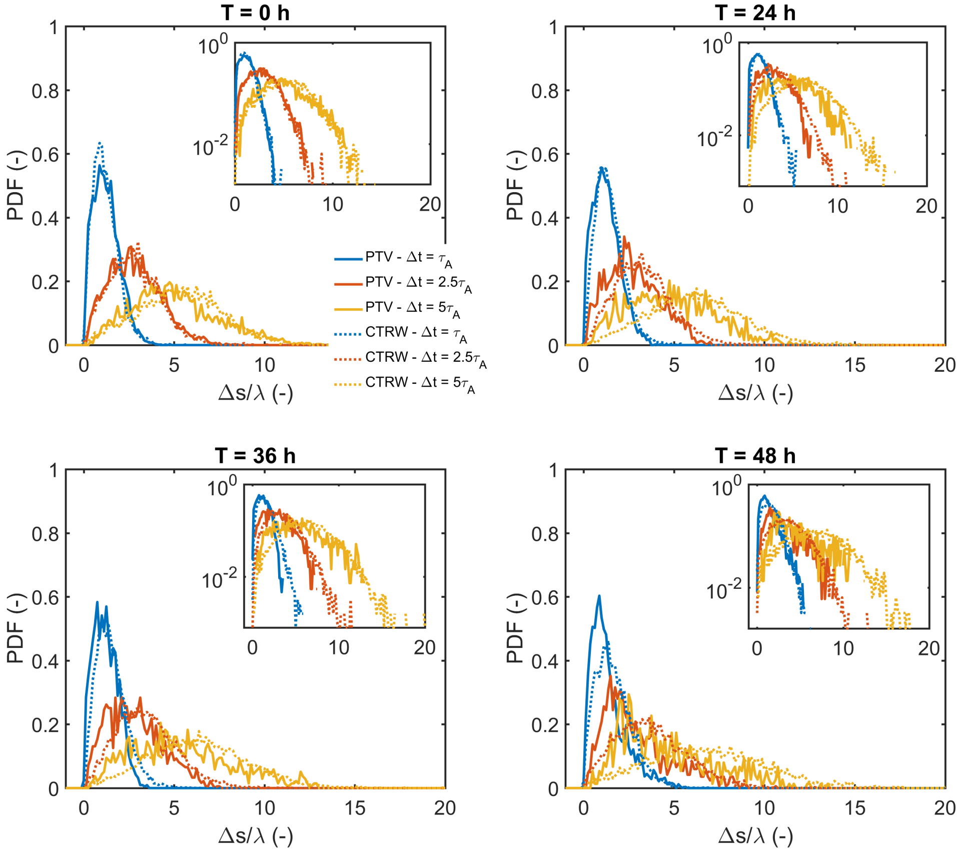

Figure 2.5: Conditional displacement probability density functions for the 3D-PTV and the CTRW data for all the different time points. The semi-logarithmic insets shows that the propagators never reach a fickian regime where they would follow a Gaussian distribution.

2.3.8 Conditional displacement PDFs

In order to further investigate how well the presented model allows to capture transport processes, we consider the conditional displacement PDFs along particle trajectories (also known as propagators) $P(s + \Delta s|s, \Delta t)$ from s to s' for a given time lag Δt. Figure 2.5 illustrates the 3D-PTV and the CTRW propagators obtained for all time points in the porous medium considered. These propagators were computed for normalized time lags corresponding to 1, 2.5 and 5 advective time scales. The semi-log propagators in the inset show that the transport regime remains superdiffusive for all the time lags considered for all time points, and that a Gaussian displacement distribution is not reached for the time lags defined. Interestingly, the skewness or third spatial moment of the propagators increases with progressive bio-clogging, as the hetereogeneity of the flow and anomalous transport in the system increase as well. The CTRW model performs very well for the clean porous medium (T = 0 h). For later time points, however, the mentioned skewness increase of the propagators is less well captured by the model.

2.4 Discussion

In this study, 3D-PTV measurements were performed during biofilm growth in a porous medium, allowing to quantify how biofilm growth changed pore-scale hydrodynamics and resulting transport behavior. The growth of biofilm induced an increase of anomalous transport in the considered system. A correlated continuous time random walk assuming a gamma distribution of the pore-scale velocity magnitudes enabled to model accurately the mean and mean-squared displacement and qualitatively the skewness of displacement probability density functions.

The average velocity and further hydrodynamic quantities follow an exponential evolution with biofilm growth, which for all quantities except the variance σ_v^2 can be described by an exponential time scale of ca. 0.015 h^-1. We conjuncture that this exponential behavior is due to the exponential growth of the bacteria in the considered system. During incubation, the effective growth coefficient of the bacteria was measured to be of ca 0.09, which is about 1 order of magnitude larger than the exponential coefficients observed for the hydrodynamic quantities. However, this difference might be attributed to the fundamental different growth kinetics of planktonic bacteria growing in a completely mixed reactor and sessile bacteria facing nutrient and electron acceptor gradients. Additionally, detachment of bacteria might also have induced a lower exponential growth coefficient. It is logical to expect that porosity, and consequently the average velocity, will increase at a rate that is imposed by the increase of biomass in the porous medium. The similar rates for geometrical parameters (correlation length λ and connectivity parameter α) are less trivial, but not unreasonable given that these metrics relate to changes of average pore-scale geometry (i.e. length scale and pore arrangement) induced by the biofilm locally and are proportional to the amount of biofilm present. On the other hand, for the velocity variance, which reflects an increased heterogeneity rather than bulk quantities, the rate is found about three times higher than for biomass growth. While we do not have an explanation for the threefold increase, the faster rate seems plausible as biofilms do not grow uniformly but form patches (Hassanpourfard et al., 2015; Nadell et al., 2017; Coyte et al., 2017; Carrel et al., 2017). This induces blockage of certain pores (which governs transitions in slow velocities) and preferential paths in other regions (which governs the high velocity tail) and the increase in this variability can not be described simply by the average.

As the pore-space is reduced upon biofilm growth, the velocities in narrowing pores increase on average. However, we also observe an increase of the probability of low velocities. This increase can be attributed to the narrowing pore size as according to Poiseuille's law for flow through a pipe (an idealization of a single pore throat). In such a case, the maximum velocity is proportional to the pore diameter squared for a constant pressure gradient. The increase of probability of low velocities due to the narrowing pore size suggests that the formation of almost stagnant zones, which marginally contribute to the total flow. Note however that locally, neither the mass flux nor the pressure gradient are fixed and therefore, the structural changes caused by the biofilm growth induce an increase of the variance of the velocity distributions, whose PDFs become increasingly non-Gaussian. Bijeljic et al. (2013); Datta et al. (2013); Siena et al. (2014); Matyka et al. (2016); Meyer and Bijeljic (2016) made similar observations for porous media with different pore network characteristics (porosity, tortuosity, pore size distribution, connectivity etc.), showing that the non-Gaussianity of the velocity PDFs was caused by the structural heterogeneity of the porous medium considered or by different degrees of saturation for partially saturated porous media. Additionally, several authors have also reported increasing exponents of the superdiffusive regime of the MSDs for porous media or fracture networks exhibiting increasing degrees of heterogeneity (Meyer and Bijeljic, 2016; Kang et al., 2017).

The results presented here were obtained for 4 different time points during the early stages of the bioclogging process. Due to the observed exponential evolution of the hydrodynamic quantities in the bioclogged system, the CTRW presented here could be parametrized for any time point whithin the duration of the experiment (i.e. the bacterial exponential growth phase). Note, however, that the described exponential evolution of the parameters of the CTRW could not go on indefinitely. Hassanpourfard et al. (2015); Bottero et al. (2013) experimentally and numerically respectively showed that for late bioclogging stages, the exponential development of the biofilm reaches a steady state (in terms of biofilm surface coverage or porosity, medium permeability etc.). Bottero et al. (2013) pointed out that this steady state was the result of biomass decay and detachment balancing biofilm growth. The presented CTRW does not allow to capture transport processes for late bioclogging stages, which still remains to be addressed.

Interestingly, the propagators obtained in Seymour et al. (2004, 2007) exhibited a substantially stronger peak for very small displacements than in the data presented in Figure 2.5. This could be partially atributed to the fact that the Péclet number of the data obtained with 3D-PTV can be considered to be infinite, as the diffusion experienced by the tracer particles is negligible, meaning that diffusive displacements are not captured in the data presented here. Another aspect lies within differences intrinsic to the experimental approaches used in both studies. Due to the fact that the 3D-PTV method used in this work only samples the effective porosity, the completely stagnant or so-called *dead end* pores are not being sampled. Additionally, the MRM method used by Seymour et al. (2004) samples flow within the biofilm as well, whereas here the tracer particles used are too large to penetrate the submicroscopic channels (Stoodley et al., 1994) of permeable biofilms (note that biofilms might have volumetric porosities of up to 90% (Wagner et al., 2010)). This might indicate that for low Péclet numbers common in porous media, the permeability of the porous biofilm itself might substantially influence transport of solutes (Davit et al., 2013; Deng et al., 2013). This was also shown to be the case for permeable benthic biofilms substantially contributing to transport and reaction processes in gravel bed streams (Aubeneau et al., 2015, 2016; Li et al., 2017).

2.5 Conclusion

In this work, we successfully monitored in 3D the progressive increase of anomalous transport with progressive biofilm growth. We observed an exponential evolution of different hydrodynamic quantities consistent with exponential growth kinetics of the biofilm. A two parameter gamma distribution provided a remarkable description of the bulk and the high tail of the velocity distribution. The shape parameter α representing the connectivity of the medium allowed to account for a shift from a mainly parallel arrangement of pores towards a more serial one, which is consistent with the observed formation of stagnation zones and preferential flow pathways. A correlated continuous time random walk based on a stochastic relaxation velocity model allowed to capture quantitatively the evolution of the first two spatial moments and the third moment qualitatively. Altogether these insights allow to describe and model the temporal influence of sessile biological activity on mass transport processes in porous media. We anticipate that the approach introduced here could also be applied to model transport in other porous media where the heterogeneity is either inherent to the original pore structure or develops dynamically as a consequence of physico-chemical processes.

2.6 Acknowledgments

We thank Toni Blunschi for manufacturing the flow cells, Peter Desmond for sharing the bacteria cultures, Daniel Braun, Lucien Biolley and Ela Burmeister for providing some of the hardware necessary for this study as well as Matthias Willmann for fruitful discussions. Financial support is gratefully acknowledged from the Swiss National Science Foundation (SNF grant numbers 144645 and 172916) for M.C. and M.H. as well as a SNF mobility grant for doctoral students for M.C.. V.L.M. acknowledges the financial support of the AXA Research fund. M.D. acknowledges the financial support of the European Research Council through the project MHetScale (Grant agreement No. 617511). The particle tracking data will be available from http://Dryad/URL/TBD upon acceptance.

Bibliography

Aubeneau, A. F., Drummond, J. D., Schumer, R., Bolster, D., Tank, J. L., and Packman, A. I. (2015). Effects of benthic and hyporheic reactive transport on breakthrough curves. *Freshwater Science*, 34(1):301–315. pages

Aubeneau, A. F., Hanrahan, B., Bolster, D., and Tank, J. (2016). Biofilm growth in gravel bed streams controls solute residence time distributions. *Journal of Geophysical Research: Biogeosciences*, 121(7):1840–1850. pages

Berkowitz, B., Scher, H., and Silliman, S. E. (2000). Anomalous transport in laboratory-scale, heterogeneous porous media. *Water Resources Research*, 36(1):149–158. pages

Bijeljic, B., Raeini, A., Mostaghimi, P., and Blunt, M. J. (2013). Predictions of non-fickian solute transport in different classes of porous media using direct simulation on pore-scale images. *Physical Review E*, 87(1):013011. PRE. pages

Bottero, S., Storck, T., Heimovaara, T. J., van Loosdrecht, M. C. M., Enzien, M. V., and Picioreanu, C. (2013). Biofilm development and the dynamics of preferential flow paths in porous media. *Biofouling*. pages

Bouwer, E. J. and Zehnder, A. J. B. (1993). Bioremediation of organic compounds — putting microbial metabolism to work. *Trends in Biotechnology*, 11(8):360–367. pages

Budwig, R. (1994). Refractive index matching methods for liquid flow investigations. *Experiments in Fluids*, 17(5):350–355. pages

Carrel, M., Beltran, M. A., Morales, V. L., Derlon, N., Morgenroth, E., Kaufmann, R., and Holzner, M. (2017). Biofilm imaging in porous media by laboratory x-ray tomography: Combining a non-destructive contrast agent with propagation-based phase-contrast imaging tools. *PLOS ONE*, 12(7):e0180374. pages

Costerton, J. W., Stewart, P. S., and Greenberg, E. P. (1999). Bacterial biofilms: A common cause of persistent infections. *Science*, 284(5418):1318–1322. pages

Coyte, K. Z., Tabuteau, H., Gaffney, E. A., Foster, K. R., and Durham, W. M. (2017). Microbial competition in porous environments can select against rapid biofilm growth. *Proceedings of the National Academy of Sciences*, 114(2):E161–E170. pages

Daccord, G. and Lenormand, R. (1987). Fractal patterns from chemical dissolution. *Nature*, 325(6099):41–43. 10.1038/325041a0. pages

Datta, S. S., Chiang, H., Ramakrishnan, T. S., and Weitz, D. A. (2013). Spatial fluctuations of fluid velocities in flow through a three-dimensional porous medium. *Physical Review Letters*, 111(6):064501. PRL. pages

Davit, Y., Byrne, H., Osborne, J., Pitt-Francis, J., Gavaghan, D., and Quintard, M. (2013). Hydrodynamic dispersion within porous biofilms. *Physical Review E*, 87(1):012718. pages

de Anna, P., Le Borgne, T., Dentz, M., Tartakovsky, A. M., Bolster, D., and Davy, P. (2013). Flow intermittency, dispersion, and correlated continuous time random walks in porous media. *Physical Review Letters*, 110(18):184502. PRL. pages

Deng, W., Cardenas, M. B., Kirk, M. F., Altman, S. J., and Bennett, P. C. (2013). Effect of permeable biofilm on micro- and macro-scale flow and transport in bioclogged pores. *Environmental Science & Technology*, 47(19):11092–11098. pages

Dentz, M., Kang, P. K., Comolli, A., Le Borgne, T., and Lester, D. R. (2016). Continuous time random walks for the evolution of lagrangian velocities. *Physical Review Fluids*, 1(7):074004. PRFLUIDS. pages

Dentz, M., Le Borgne, T., Englert, A., and Bijeljic, B. (2011). Mixing, spreading and reaction in heterogeneous media: A brief review. *Journal of Contaminant Hydrology*, 120–121:1–17. pages

Downie, H., Holden, N., Otten, W., Spiers, A. J., Valentine, T. A., and Dupuy, L. X. (2012). Transparent soil for imaging the rhizosphere. *PLoS ONE*, 7(9):e44276. pages

Durham, W. M., Tranzer, O., Leombruni, A., and Stocker, R. (2012). Division by fluid incision: Biofilm patch development in porous media. *Physics of Fluids*, 24(9):091107. pages

Edery, Y., Guadagnini, A., Scher, H., and Berkowitz, B. (2014). Origins of anomalous transport in heterogeneous media: Structural and dynamic controls. *Water Resources Research*, 50(2):1490–1505. pages

Gouze, P., Le Borgne, T., Leprovost, R., Lods, G., Poidras, T., and Pezard, P. (2008). Non-fickian dispersion in porous media: 1. multiscale measurements using single-well injection withdrawal tracer tests. *Water Resources Research*, 44(6):n/a–n/a. pages

Gujer, W. and Boller, M. (1986). Design of a nitrifying tertiary trickling filter based on theoretical concepts. *Water Research*, 20(11):1353–1362. pages

Gülan, U., Lüthi, B., Holzner, M., Liberzon, A., Tsinober, A., and Kinzelbach, W. (2012). Experimental study of aortic flow in the ascending aorta via particle tracking velocimetry. *Experiments in Fluids*, 53(5):1469–1485. pages

Haitao, X. (2008). Tracking lagrangian trajectories in position–velocity space. *Measurement Science and Technology*, 19(7):075105. pages

Hall-Stoodley, L., Costerton, J. W., and Stoodley, P. (2004). Bacterial biofilms: from the natural environment to infectious diseases. *Nat Rev Micro*, 2(2):95–108. pages

Hassanpourfard, M., Nikakhtari, Z., Ghosh, R., Das, S., Thundat, T., Liu, Y., and Kumar, A. (2015). Bacterial floc mediated rapid streamer formation in creeping flows. *Scientific Reports*, 5:13070. pages

Head, I. M., Jones, D. M., and Larter, S. R. (2003). Biological activity in the deep subsurface and the origin of heavy oil. *Nature*, 426(6964):344–352. 10.1038/nature02134. pages

Holzner, M., Morales, V. L., Willmann, M., and Dentz, M. (2015). Intermittent lagrangian velocities and accelerations in three-dimensional porous medium flow. *Physical Review E*, 92(1):013015. pages

Hoyer, K., Holzner, M., Lüthi, B., Guala, M., Liberzon, A., and Kinzelbach, W. (2005). 3d scanning particle tracking velocimetry. *Experiments in Fluids*, 39(5):923–934. pages

Jiménez-Martínez, J., Porter, M. L., Hyman, J. D., Carey, J. W., and Viswanathan, H. S. (2016). Mixing in a three-phase system: Enhanced production of oil-wet reservoirs by co2 injection. *Geophysical Research Letters*, 43(1):196–205. pages

Kang, P. K., de Anna, P., Nunes, J. P., Bijeljic, B., Blunt, M. J., and Juanes, R. (2014). Pore-scale intermittent velocity structure underpinning anomalous transport through 3-d porous media. *Geophysical Research Letters*, 41(17):6184–6190. pages

Kang, P. K., Dentz, M., Le Borgne, T., Lee, S., and Juanes, R. (2017). Anomalous transport in disordered fracture networks: Spatial markov model for dispersion with variable injection modes. *Advances in Water Resources*, 106:80–94. pages

Kazemifar, F., Blois, G., Kyritsis, D. C., and Christensen, K. T. (2016). Quantifying the flow dynamics of supercritical co2–water displacement in a 2d porous micromodel using fluorescent microscopy and microscopic piv. *Advances in Water Resources*, 95:352–368. pages

Klump, S., Tomonaga, Y., Kienzler, P., Kinzelbach, W., Baumann, T., Imboden, D. M., and Kipfer, R. (2007). Field experiments yield new insights into gas exchange and excess air formation in natural porous media. *Geochimica et Cosmochimica Acta*, 71(6):1385–1397. pages

Knecht, K., Schroth, M. H., Schulin, R., and Nowack, B. (2011). Development and evaluation of micro push–pull tests to investigate micro-scale processes in porous media. *Environmental Science & Technology*, 45(15):6460–6467. pages

Kone, T., Golfier, F., Orgogozo, L., Oltéan, C., Lefèvre, E., Block, J. C., and Buès, M. A. (2014). Impact of biofilm-induced heterogeneities on solute transport in porous media. *Water Resources Research*, 50(11):9103–9119. pages

Lazar, I., Petrisor, I. G., and Yen, T. F. (2007). Microbial enhanced oil recovery (meor). *Petroleum Science and Technology*, 25(11):1353–1366. pages

Le Borgne, T., Bolster, D., Dentz, M., de Anna, P., and Tartakovsky, A. (2011a). Effective pore-scale dispersion upscaling with a correlated continuous time random walk approach. *Water Resources Research*, 47(12). pages

Le Borgne, T., Dentz, M., and Carrera, J. (2008). Lagrangian statistical model for transport in highly heterogeneous velocity fields. *Physical Review Letters*, 101(9):090601. PRL. pages

Le Borgne, T., Dentz, M., Davy, P., Bolster, D., Carrera, J., de Dreuzy, J.-R., and Bour, O. (2011b). Persistence of incomplete mixing: A key to anomalous transport. *Physical Review E*, 84(1):015301. PRE. pages

Le Borgne, T. and Gouze, P. (2008). Non-fickian dispersion in porous media: 2. model validation from measurements at different scales. *Water Resources Research*, 44(6):n/a–n/a. pages

Leverenz, H. L., Tchobanoglous, G., and Darby, J. L. (2009). Clogging in intermittently dosed sand filters used for wastewater treatment. *Water Research*, 43(3):695–705. pages

Li, A., Aubeneau, A. F., Bolster, D., Tank, J. L., and Packman, A. I. (2017). Covariation in patterns of turbulence-driven hyporheic flow and denitrification enhances reach-scale nitrogen removal. *Water Resources Research*, pages n/a–n/a. pages

Linga, G., Mathiesen, J., and Renard, F. (2017). Self-similar distributions of fluid velocity and stress heterogeneity in a dissolving porous limestone. *Journal of Geophysical Research: Solid Earth*, 122(3):1726–1743. pages

Lüthi, B., Tsinober, A., and Kinzelbach, W. (2005). Lagrangian measurement of vorticity dynamics in turbulent flow. *Journal of Fluid Mechanics*, 528:87–118. pages

Maas, H. G., Gruen, A., and Papantoniou, D. (1993). Particle tracking velocimetry in three-dimensional flows. *Experiments in Fluids*, 15(2):133–146. pages

Malik, N. A., Dracos, T., and Papantoniou, D. A. (1993). Particle tracking velocimetry in three-dimensional flows. *Experiments in Fluids*, 15(4-5):279–294. pages

Matyka, M., Gołembiewski, J., and Koza, Z. (2016). Power-exponential velocity distributions in disordered porous media. *Physical Review E*, 93(1):013110. PRE. pages

Menke, H. P., Bijeljic, B., Andrew, M. G., and Blunt, M. J. (2015). Dynamic three-dimensional pore-scale imaging of reaction in a carbonate at reservoir conditions. *Environmental Science & Technology*, 49(7):4407–4414. pages

Meyer, D. W. and Bijeljic, B. (2016). Pore-scale dispersion: Bridging the gap between microscopic pore structure and the emerging macroscopic transport behavior. *Physical Review E*, 94(1):013107. PRE. pages

Michalec, F.-G., Souissi, S., and Holzner, M. (2015). Turbulence triggers vigorous swimming but hinders motion strategy in planktonic copepods. *Journal of The Royal Society Interface*, 12(106). pages

Morales, V. L., Dentz, M., Willmann, M., and Holzner, M. (20). Stochastic dynamics of intermittent pore-scale particle motion in three–dimensional porous media: Experiments and theory. *Geophysical Research Letters*, pages n/a–n/a. pages

Moroni, M. and Cushman, J. H. (2001). Statistical mechanics with three-dimensional particle tracking velocimetry experiments in the study of anomalous dispersion. ii. experiments. *Physics of Fluids (1994-present)*, 13(1):81–91. pages

Moroni, M., Kleinfelter, N., and Cushman, J. H. (2007). Analysis of dispersion in porous media via matched-index particle tracking velocimetry experiments. *Advances in Water Resources*, 30(1):1–15. pages

Nadell, C. D., Ricaurte, D., Yan, J., Drescher, K., and Bassler, B. L. (2017). Flow environment and matrix structure interact to determine spatial competition in pseudomonas aeruginosa biofilms. *eLife*, 6:e21855. pages

Noiriel, C., Gouze, P., and Madé, B. (2013). 3d analysis of geometry and flow changes in a limestone fracture during dissolution. *Journal of Hydrology*, 486:211–223. pages

Pintelon, T. R. R., Graf von der Schulenburg, D. A., and Johns, M. L. (2009). Towards optimum permeability reduction in porous media using biofilm growth simulations. *Biotechnology and Bioengineering*, 103(4):767–779. pages

Rubol, S., Freixa, A., Carles-Brangarí, A., Fernàndez-Garcia, D., Romaní, A. M., and Sanchez-Vila, X. (2014). Connecting bacterial colonization to physical and biochemical changes in a sand box infiltration experiment. *Journal of Hydrology*, 517:317–327. pages

Saha, D., Soos, M., Lüthi, B., Holzner, M., Liberzon, A., Babler, M. U., and Kinzelbach, W. (2014). Experimental characterization of breakage rate of colloidal aggregates in axisymmetric extensional flow. *Langmuir*, 30(48):14385–14395. pages

Sakthivadivel, R. and Einstein, H. (1970). Clogging of porous column of spheres by sediment. *Journal of the Hydraulics Division*, 96(2):461–472. pages

Schmidt, L., Fouxon, I., Krug, D., van Reeuwijk, M., and Holzner, M. (2016). Clustering of particles in turbulence due to phoresis. *Physical Review E*, 93(6):063110. PRE. pages

Seki, K., Thullner, M., Hanada, J., and Miyazaki, T. (2006). Moderate bioclogging leading to preferential flow paths in biobarriers. *Ground Water Monitoring and Remediation*, 26(3):68–76. pages

Seymour, J. D., Gage, J. P., Codd, S. L., and Gerlach, R. (2004). Anomalous fluid transport in porous media induced by biofilm growth. *Physical Review Letters*, 93(19):198103. pages

Seymour, J. D., Gage, J. P., Codd, S. L., and Gerlach, R. (2007). Magnetic resonance microscopy of biofouling induced scale dependent transport in porous media. *Advances in Water Resources*, 30(6–7):1408–1420. pages

Siena, M., Riva, M., Hyman, J. D., Winter, C. L., and Guadagnini, A. (2014). Relationship between pore size and velocity probability distributions in stochastically generated porous media. *Physical Review E*, 89(1):013018. PRE. pages

Stoodley, P., deBeer, D., and Lewandowski, Z. (1994). Liquid flow in biofilm systems. *Applied and Environmental Microbiology*, 60(8):2711–2716. pages

von der Schulenburg, D. A. G., Pintelon, T. R. R., Picioreanu, C., Van Loosdrecht, M. C. M., and Johns, M. L. (2009). Three-dimensional simulations of biofilm growth in porous media. *AIChE Journal*, 55(2):494–504. pages

Wagner, M., Taherzadeh, D., Haisch, C., and Horn, H. (2010). Investigation of the mesoscale structure and volumetric features of biofilms using optical coherence tomography. *Biotechnology and Bioengineering*, 107(5):844–853. pages

Yao, K.-M., Habibian, M. T., and O'Melia, C. R. (1971). Water and waste water filtration. concepts and applications. *Environmental science and technology*, 5(11):1105–1112. pages

Chapter 3

Biofilm Imaging in Porous Media by Laboratory X-ray Tomography: Combining a Non-Destructive Contrast Agent with Propagation-Based Phase-Contrast Imaging Tools

This chapter consists of a manuscript published in PLOS ONE, 2017:

M. Carrel[a,b,c,e], M.A. Beltran[a,b,d,f], V.L. Morales[a,f], N. Derlon[a,f], E. Morgenroth[a,f], R. Kaufmann[a,f], M. Holzner[a,f]. Biofilm Imaging in Porous Media by Laboratory X-ray Tomography: Combining a Non-Destructive Contrast Agent with Propagation-Based Phase-Contrast Imaging Tools. *PLOS ONE*
doi.org/10.1371/journal.pone.0180374

[a] Study concept and design; [b] Data acquisition and analysis; [c] Interpretation of data; [d] Developing the theoretical concept; [e] Drafting manuscript; [f] Critical revision

Abstract

X-ray tomography is a powerful tool giving access to the morphology of biofilms, in 3D porous media, at the mesoscale. Due to the high water content of biofilms, the attenuation coefficient of biofilms and water are very close, hindering the distinction between biofilms and water without the use of contrast agents. Until now, the use of contrast agents such as barium sulfate, silver-coated micro-particles or 1-chloronaphtalene added to the liquid phase allowed imaging the biofilm 3D morphology. However, these contrast agents are not passive and potentially interact with the biofilm when injected into the sample. Here, we use a natural inorganic compound, namely iron sulfate, as a contrast agent progressively bounded in dilute or colloidal form into the EPS matrix during biofilm growth. By combining a very long source-to-detector distance on a X-ray laboratory source with a Lorentzian filter implemented prior to tomographic reconstruction, we substantially increase the contrast between the biofilm and the surrounding liquid, which allows revealing the 3D biofilm morphology. A comparison of this new method with the method proposed by Davit et al. (2011), which uses barium sulfate as a contrast agent to mark the liquid phase was performed. Quantitative evaluations between the methods revealed substantial differences for the volumetric fractions obtained from both methods. Namely, contrast agent - biofilm interactions (e.g. biofilm detachment) occurring during barium sulfate injection caused a reduction of the biofilm volumetric fraction of more than 50% and displacement of biofilm patches elsewhere in the column. Two key advantages of the newly proposed method are that passive addition of iron sulfate maintains the integrity of the biofilm prior to imaging, and that the biofilm itself is marked by the contrast agent, rather than the liquid phase as in other available methods. The iron sulfate method presented can be applied to understand biofilm development and bioclogging mechanisms in porous materials and the obtained biofilm morphology could be an ideal basis for 3D numerical calculations of hydrodynamic conditions to investigate biofilm-flow coupling.

3.1 Introduction

Biofilms are ubiquitous sessile microorganisms embedded in a self-produced matrix consisting of extracellular polymeric substances (EPS) (Hall-Stoodley et al., 2004). The EPS matrix protects biofilms from their environment, so that they persistently develop and survive in industrial, natural or biomedical settings (Costerton et al., 1999). In water saturated soils, most microorganisms develop sessile lifestyles (Griebler and Lueders, 2009). Biofilms are of high interest in this context, because of their natural contribution to the bioremediation of aquifers (Meckenstock et al., 2015) or to reactive barriers (Blowes et al., 2000), to microbial enhanced oil recovery (Lappin-Scott et al., 1988) or to the sequestration of carbon dioxide (Ebigbo et al., 2010; Mitchell et al., 2013). However, the growth of biofilms in porous media and the consequent bioclogging of the pore spaces (Baveye et al., 1998) can also be detrimental as it can lead to the clogging of groundwater recharge wells (Bouwer, 2002) or deep geothermal systems (Sand, 2003). It can also lead to an enhanced non-Fickian spreading of solute contaminants in groundwater (Seymour et al., 2004), substantially complexifying the modelling and upscaling of mass transport in these systems (Davit et al., 2010; Golfier et al., 2009; Kapellos et al., 2010; Orgogozo et al., 2010; Pintelon et al., 2009; von der Schulenburg et al., 2009).

Biofilms have been described as microbial landscapes (Battin et al., 2007) stretching over a large range of spatial scales (Milferstedt et al., 2009) ranging from the micro- (individual cells), to the meso- (biofilm patches scale) or to the macroscale (reactor, aquifer scales). Accordingly, different experimental methods have been developed to investigate processes at different scales, from optical or confocal microscopes to characterize microscale development of biofilms in flow cells (Stoodley et al., 2005) or microfluidic devices (Rusconi et al., 2010), to studies using soil columns (Cunningham et al., 1991; Taylor and Jaffé, 1990) and characterizing the influence of biofilms on bulk system (macro-scale) properties (permeability reduction, dispersion, degradation rates of solutes etc.).

The mesoscale, which is the scale of interest in this study, is the scale where the biofilm structure is being shaped by the interplay of the hydromechanical and mass transfer processes. In porous media, this scale approximately corresponds to the pore-scale. Many investigations for porous media at that scale were performed using optical systems (Dupin and McCarty, 2000; Kone et al., 2014; Paulsen et al., 1997; Sharp et al., 1999; Thullner et al., 2002; Vayenas et al., 2002), but were limited to 2 dimensions. Lately, Optical Coherence Tomography (OCT) (Derlon et al., 2012; Wagner et al., 2010b; Xi et al., 2006) stood out as a very powerful method to investigate these processes at the mesoscale for many different systems. However, OCT uses low coherent light in the visible range and the opacity of 3D samples limits the penetration depth. Therefore, OCT cannot be used for 3D porous media samples. Magnetic Resonance Imaging (MRI) is a great tool to obtain both flow and biofilm stuctural information, it is limited in spatial resolution (generally resolution coarser than 50 μm) which makes it difficult to access the exact liquid and biofilm phases from the transverse relaxation times (T2) (Graf von der Schulenburg et al., 2008; Seymour et al., 2004; Wagner et al., 2010a; Vogt et al., 2013).

In the last few decades, X-ray microtomography (X-ray μCT) became a standard tool for imaging soil samples (Wildenschild et al., 2002; Wildenschild and Sheppard, 2013) and to image biofilm structures in 3D soil-like samples. Differentiating the biofilm from the liquid phase is a difficult task when using X-ray μCT due to the high water content of biofilms and the consequently very close X-ray attenuation coefficients of water and biofilms. As a result, it is common to use chemical agents to increase the contrast between the biofilm and liquid phases. Particulate barium sulfate ($BaSO_4$) suspensions were used as contrast agent to label non-biofilm colonized pores and imaged biofilm on a X-ray lab source (Davit et al., 2011). Silver-coated 10 μm microspheres deposited at the biofilm surface revealed the biofilm-liquid interface using synchrotron radiation (Iltis et al., 2011). Another approach suggested was based on the use of 1-chloronaphtalene, an immiscible liquid with water, as a contrast agent (Rolland du Roscoat et al., 2014; Ivankovic et al., 2016). Finally, numerical pore-scale biofilm growth modeling was performed based on biofilm structures obtained at different Reynolds numbers from X-ray synchrotron tomography using $BaSO_4$ as a contrast agent(Peszynska et al., 2016).

All the described methods based on X-ray μCT to image biofilms either used a particulate suspension or a chemical to mark the liquid phase that was introduced *a posteriori* in the biofilm containing sample. The rationales behind the approach using particulate $BaSO_4$ suspensions is first, that the $BaSO_4$ particles are micrometer-sized and behave passively. Second, that the biofilm inner channels are smaller than the micrometer-sized barium suflate particles (Stoodley et al., 1994) and therefore, that advection of the $BaSO_4$ particles within the biofilm is negligible. However, these rationales remind largely untested so far. Additionally, given that $BaSO_4$ is a relatively heavy compound ($\rho_{BaSO_4} = 3.62 g/cm^3$), sedimentation issues arise, which can be exacerbated by the aggregation of the particles and then lead to motion blur artifacts. The use of additives such as xantham gum stabilizes these solutions but also change the rheological properties, potentially inducing biofilm detachment (Davit et al., 2011). On the other hand, the approach based on silver-coated microspheres (Iltis et al., 2011) suffered from the heterogeneous distribution of the silver-coated microspheres and possible interactions between the dense microspheres suspensions and the biofilm were not investigated. The 1-chloronaphtalene used as a contrast enhancing agent (Rolland du Roscoat et al., 2014; Ivankovic et al., 2016) also has significant drawbacks, since this liquid is immiscible with water. Therefore, the non-wetting phase curvatures and contact angles may not contour exactly the interface with the aqueous biofilm phase. Additionally, it is not guaranteed that the capillary pressure requirements to invade all unclogged pores are met. Finally, 1-chloronaphtalene is a powerful pesticide whose interactions with biofilms have not been investigated yet.

In this study, instead of adding a potentially destructive contrast agent to the liquid phase, we use iron sulfate ($FeSO_4$), a non-toxic inorganic compound naturally present in soils. $FeSO_4$ is commonly used in biofilm studies (Möhle et al., 2007; Wagner et al., 2010b; Blauert et al., 2015). The rationale behind this approach is that some biofilms naturally exhibit high content of inorganic matter (e.g. mineral precipitates (Li et al., 2005)). $FeSO_4$ is a compound naturally present in some aquifers and it can even be artificially introduced to enhance the bioremediation of contaminants (arsenic, uranium) by enhancing their precipitation (Anderson et al., 2003; Omoregie et al., 2013). Here, the biofilm is cultured under the continuous addition of a solution containing $FeSO_4$ that is either bound in a dilute form within the EPS or forming colloidal matter on which the biofilm can develop. Both iron and sulfate concentrations used in this study are in the range of concentrations observed in the environment and in contaminated sites (Benner et al., 2002; Teixeira et al., 2014; Weiner, 2013). In order to increase the contrast and visualize the biofilm, we image the biofilm on a laboratory-based X-ray source using a relatively large source-to-detector (STD) distance. The large STD was used to exploit X-ray free space propagation in order to render visible refraction effects that take place as the X-rays travel through the sample, a technique commonly known as propagation-based phase contrast (PBI) (Paganin, 2006; Wilkins et al., 1996). In addition, a robust Fourier filter which has the form of a Lorentzian function is applied as a digital pre-processing tool to the acquired projections to enhance the contrast and to improve the signal-to-noise ratio (SNR) (Beltran et al., 2010, 2011). The presented method allows to image the 3D biofilm morphology in porous media at the mesoscale, using an X-ray lab source and a non-destructive contrast agent.

3.2 Materials and Methods

3.2.1 Porous media and Biofilm culturing

The porous media used in this study consisted of Nafion pellets (NR50 1100 EW, Ion Power, Munich, Germany) of 2.5 mm diameter similar to coarse sand grains. This material has similar physical and chemical properties to sand grains (e.g. particle size distribution or ion exchange capacity) and its optical refractive index in the visible domain is similar to that of water (Downie et al., 2012; Holzner et al., 2015). For the inoculation of the media, the Nafion pellets were immersed for 24 h in an aerated batch containing 500 mL of natural water sampled from a pond located on the ETH campus. After 24 h, a polymethyl methacrylate (PMMA) tubular reactor (inner diameter 10 mm, length 160 mm) was wet packed with the pellets and connected to the batch. A biofilm was cultivated for 7 days using the setup shown in Fig 3.1A. A 500 mL feed solution made of tap water containing 1 g/L of glucose and 100 mg/L was used and changed every 48 h. A volumetric flow rate of 5 mL/min was set which corresponds to a Darcy velocity q of 1.06 mm/s. The initial porosity (volumetric fraction of the liquid phase) ϕ is ca. 40%, which yields an average pore scale velocity $v_p \approx q/\phi = 2.65$ mm/s and corresponding Reynolds number $Re = qd/\nu \approx 2.5$ and Péclet number $Pe = qd/D_{H_2O} \approx 1000$. Upon biofilm growth, the porosity decreased by a twofold factor, meaning that the average pore scale velocity doubled.

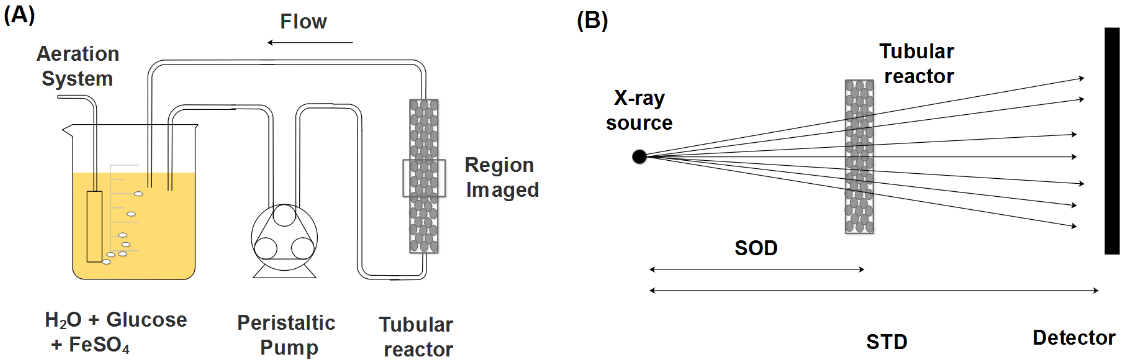

Figure 3.1: (A) Schematic of the experimental setup used for the biofilm culturing as well as the region of the tubular reactor used for biofilm imaging. (B) Schematic of the configuration used for the X-ray scans where the distances SOD and STD represent the source-to-object (SOD) and the source-to-detector distance (STD).

3.2.2 Contrast agents

A concentration of 100 mg/L of the contrast agent used in this study $FeSO_4x7(H_2O)$ (corresponding to 56 mg/L $FeSO_4$ (20.6 mg/L Fe and 35.4 mg/L SO_4) or 0.37 mmol/L $FeSO_4$)

was continuously added to the feed solution during the biofilm growth. The concentrations of both iron and sulfate compounds are in the range of concentrations observed in the environment (Benner et al., 2002; Teixeira et al., 2014; Weiner, 2013) or used for other experimental work (Blauert et al., 2015; Möhle et al., 2007; Wagner et al., 2010b). At that concentration and for the initial pH observed in this study (pH ≈ 7), the iron should be still soluble. However, the oxidation to Fe(III), which is less soluble and tends to form colloids, should occur quite rapidly (Weiner, 2013). In fact, iron flocs formed a few hours after the start-up of the system. Therefore, the inlet tubing was carefully set close to the water level, to limit the circulation of the flocs and to enhance their settling. The biofilm grown here exhibited a brownish color typical of iron oxides. Before the X-ray measurements, a volume of water corresponding to 8 times the initial pore volume was injected through the flow cell to ensure that no biofilm unbound iron was remaining in the liquid phase.

To investigate the influence of the colloidal and flocculated iron on porous medium flow and to monitor deposition of colloids inside the medium, we performed a control experiment. In that experiment, a $FeSO_4$ containing solution was recirculated through a packed tubular reactor with identical conditions as those stated above, but without inoculation.

In order to compare the results obtained from this new approach with an already existing method, we followed the approach presented by Davit et al. (2011), using a particulate Micropaque® (Guerbet, Zurich) $BaSO_4$ suspension as a contrast agent that was introduced into the liquid phase after the growth of the biofilm. $BaSO_4$ suspensions are used to image biofilms in porous media because of the high attenuation coefficient of barium. Another advantage is that the $BaSO_4$ particles are micrometer-sized and should therefore be physically size excluded from the EPS matrix (Stoodley et al., 1994). Micropaque® suspensions have a particle size distribution close to 1 μm (according to the manufacturer of the product, 25% $\leq$ particles larger than 2 μm, 20% $\leq 0.5 \mu m$ an average diameter of 1.25 μm). These suspensions also contain additional stabilizing agents (e.g. xanthan gum, polydimethylsiloxane (PDMS) or sodium citrate etc.) that prevent the aggregation and sedimentation of the particles but strongly influence the rheological properties of the suspension. Plouraboué et al. (2004) showed that the Micropaque® barium suflate suspensions exhibited a viscosity much higher than water and a shear-thinning behavior similar to that of blood (see Fig 1.b in Plouraboué et al. (2004)). Here, a Micropaque® suspension of 0.1 g/mL $BaSO_4$ concentration was injected in the tubular reactor at 10 % of the volumetric flow rate applied during the biofilm culturing in an attempt to avoid forced detachment due to the injection of the contrast agent. Due to dispersion and dilution effects, the distribution of the $BaSO_4$ in the reactor was inhomogeneous after 1 pore volume. Therefore, 2 times the initial pore volume of the tubular were injected to completely saturate the tubular reactor with the suspension. Although the injection was done carefully and at a flow rate 10 times smaller than the one used for water, significant biofilm detachment was visually observed during the injection.

3.2.3 X-ray imaging

Table 3.1 provides an overview of the different imaging conditions and image analysis approaches for the four datasets obtained from three different scans performed in the frame of this work. A first scan was performed with the sample containing the biofilm stained with $FeSO_4$ only. For this scan (used to obtain the $FeSO_4$ and $LFeSO_4$ datasets), the source-to-object distance (SOD) was of 130 mm and the source-to-detector distance (STD) was set to the largest possible distance, 2330 mm (see Fig 3.1. B). As mentioned previously, this fairly large STD distance was chosen to enhance the refraction effects occuring as the X-rays travel through the sample. The custom made tomographic setup was equipped with a microfocus X-ray tube (Viscom XT9160-TDX) and a 40 x 40 cm^2 flat panel detector (Perkin Elmer XRD 1621) with 200 x 200 μm^2 pixels. Since biofilms weakly absorb X-rays, the source had to be operated at a voltage of 50 kV and and a focused electron beam current (FEC) of 190 μA. 1441 projections with a field of view (FOV) of 1.85 x 1.85 cm^2 were gathered at 0.25° angle steps with two frames per projection at a resolution of 9 μm. For the second scan ($BaSO_4$ dataset), the same sample was used (see Table 3.1). The SOD distance was unchanged and the STD distance was reduced to 1017 mm, which would correspond to a reasonable distance for standard X-ray attenuation-based imaging. The voltage was set to 80 kV and the FEC to 120 μA. 1441 projections with a FOV of 4.3 x 4.3 cm^2 were gathered at 0.25° angle steps with three frames per projection at a resolution of 21 μm. The difference in resolution between both scans is due to the fact that the SOD stayed constant and the STD decreased, reducing the physical magnification. For the last scan (control dataset LControl), the settings were the same as for the first one. Due to the rather low contrast of the projections and variations in the source intensity the projections were normalised to reach a reasonable contrast in the 3D volume. This pre-processing and the reconstruction were performed on in-house developed software tools based on filtered back-projection (Feldkamp et al., 1984). The scanning times were of ca. 3 hours.

3.2.4 Image analysis

Image Preprocessing by means of a Lorentzian filter

A key step for the results produced with the $FeSO_4$ data is the application of an image processing Lorentzian filter in Fourier space to each radiographic projection before tomographic reconstruction. To evaluate the utility of the Lorenztian filter, the data from the first scan was reconstructed with and without applying this filter ($LFeSO_4$ resp. $FeSO_4$ datasets) and also applied to the control dataset (LControl, see Table 3.1). The filter presented here substantially reduces noise and enhances contrast. It is based on the original work of Paganin et al. (2002) where it was initially developed as a method to retrieve phase-and-amplitude information from inline propagation-based X-ray holograms using monochromatic beams and specifically for single-material samples. Here, the monochromaticity and single material assumptions are discarded and the algorithm is used *strictly* as an image processing tool, which exploits its high numerical stability under the presence of noise. This stability was shown in previous studies to greatly improve the contrast and

Table 3.1: Information relative to the different scans and datasets used in this work as well as the corresponding details concerning the data analysis.

Dataset	$FeSO_4$	$LFeSO_4$	$BaSO_4$	$LControl$
Tubular reactor Nr	1	1	1	2
Scan Nr	1	1	2	3
Biofilm Growth	Yes	Yes	Yes	No
Contrast agents	$FeSO_4$	$FeSO_4$	$FeSO_4$&$BaSO_4$	$FeSO_4$
Source to detector distance (mm)	2330	2330	1017	2330
Scan details	50 kV, 190 μA	50 kV, 190 μA	80 kV, 190 μA	50 kV, 190 μA
Scan resolution (μm)	9	9	21	9
Projection image processing prior to reconstruction	-	Lorentzian filter	-	Lorentzian filter
Image filtering prior to segmentation	-	3D curvature-driven diffusive filter	3D curvature-driven diffusive filter	3D curvature-driven diffusive filter
Segmentation approach	-	VG Max surface determination	Seeded region growing algorithm & VG Max surface determination	VG Max surface determination
Registered dataset	No	Yes	Yes	No

the signal quality both in simple projection imaging as well as tomography (Arhatari et al., 2010; Beltran et al., 2010, 2011; Burvall et al., 2011; Gureyev et al., 2006; Mayo et al., 2003; Myers et al., 2008). The Lorentzian filter used here has the following form:

$$\mathrm{I}^{\mathrm{Filt}} = \mathrm{F}^{-1}\left[\frac{1}{\alpha \mathbf{k}_{\perp}^{2}+1}\mathrm{F}\left\{\mathrm{I}^{\mathrm{Rad}}\right\}\right] \tag{3.1}$$

Here, $\mathrm{I}^{\mathrm{Rad}}$ is the acquired radiographic image at a particular orientation. $\mathrm{I}^{\mathrm{Filt}}$ is the filtered image once the Lorentzian filter is applied to $\mathrm{I}^{\mathrm{Rad}}$. The symbols F and F^{-1} are the forward and inverse Fourier transforms. $\mathbf{k}_{\perp} = (k_x, k_y)$ are the transverse Fourier space coordinates reciprocal to the real space coordinates $\mathbf{r}_{\perp} = (x, y)$. In other words, the operation in Eq. (4.23) is as follows: (i) Take the Fourier transform of the image $\mathrm{I}^{\mathrm{Rad}}$, which in this case serves as input data; (ii) multiply the result by the Fourier space Lorentzian function $\frac{1}{\alpha \mathbf{k}_{\perp}^{2}+1}$ and; (iii) take the inverse Fourier transform thus attaining the filtered image $\mathrm{I}^{\mathrm{Filt}}$; (iv) perform the tomographic reconstruction using the backprojection method mentioned earlier. The filter was implemented as a Matlab® routine available from (DigitalRocks, 2017). The non-negative real valued constant α is an important parameter of the filter. It is important to mention that in the original form of the algorithm (see Paganin et al. (2002)), the value of α was known *a priori* since it is meant specifically to deal with only single material specimens. However, for our purposes, we use it as a *tuning parameter* that may be adjusted according to how much noise one desires to remove without over-blurring key features (edges) in the reconstructions. To obtain a good estimate of α we use a strategy that takes a raw projection image from the CT set which is used as reference and then graphically compared to a filtered image. An example of this strategy is seen in Fig 3.2.

Here, we have an unfiltered radiographic image I^{Rad} in Fig 3.2A and a Lorentz filtered I^{Filt} version of the same image in Fig 3.2B and 3.2C obtained with values of α of $1.5 \cdot 10^{-6}$ and with $1.5 \cdot 10^{-5}$, respectively. In this work, an α value of $1.5 \cdot 10^{-6}$ was used. In Fig 3.2D, gray value profiles of images (A), (B) and (C) across the same horizontal line are shown enabling a graphical comparison. These profiles show how the blue curve corresponding to (B) displays significantly less noise than the red curve corresponding to (A). In addition to noise reduction we see that the blue profile corresponding to (B) also follows the same trend than the red one. This is illustrated more clearly in the inset showing a magnified region of the profiles. For the other value of α ($\alpha = 1.5 \cdot 10^{-5}$), both (C) and (D) (black), the effect of the over-blurring is evident. The balance of noise reduction and trend matching provides us a qualitative, yet clear visual indication whether our value chose for α is neither over- nor underestimated.

The effectiveness of the Lorentzian filter from a tomographic perspective is illustrated in Fig 3.3. Here, we show tomographic slices of the same region with (A) and without (C) applying the Lorentzian filter before reconstructing. From this example it is evident that applying the Lorentzian filter prior to reconstruction greatly improves the visualization of the biofilm/water interface in the tomographic reconstruction. Fig 3.3B and 3.3D show gray value profiles labeled P1 and P2 clearly illustrating a reduction of noise. Boundaries still remain well defined after the application of the Lorentzian filter.

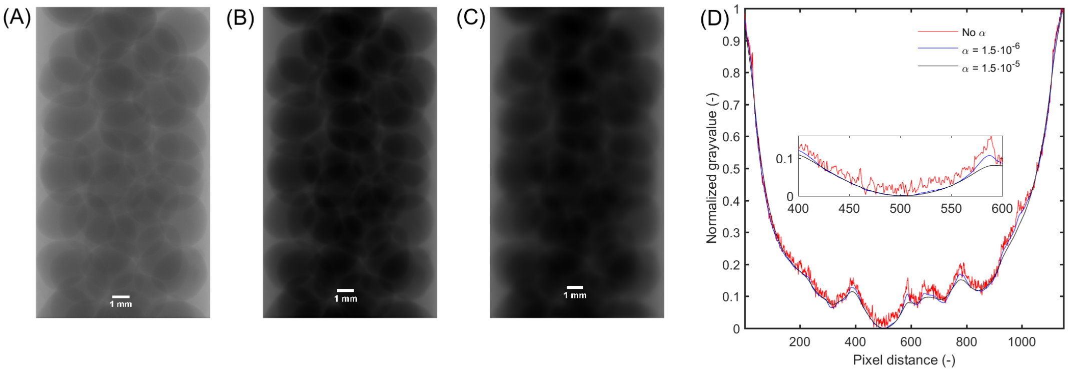

Figure 3.2: (A) raw projection image (unfiltered). (B) Lorentz filtered image of (A) using $\alpha = 1.5 \cdot 10^{-7}$. (C) Lorentz filtered image of A using $\alpha = 1.5 \cdot 10^{-8}$. The same dynamic range was used for (A), (B) and (C) for the sake of comparison. (D) displays horizontal normalized profiles at the location of the dashed line in (A), and (B) and (C) as well as for additional values of α. The inset shows a magnification of the gray value profile at the center of the tubular reactor. The scale bar in (A) is also valid on (B) and (C).

Segmentation

Since two different contrast agents were used, it was not possible to define one segmentation procedure and apply it to all datasets so that a single approach was defined for each contrast

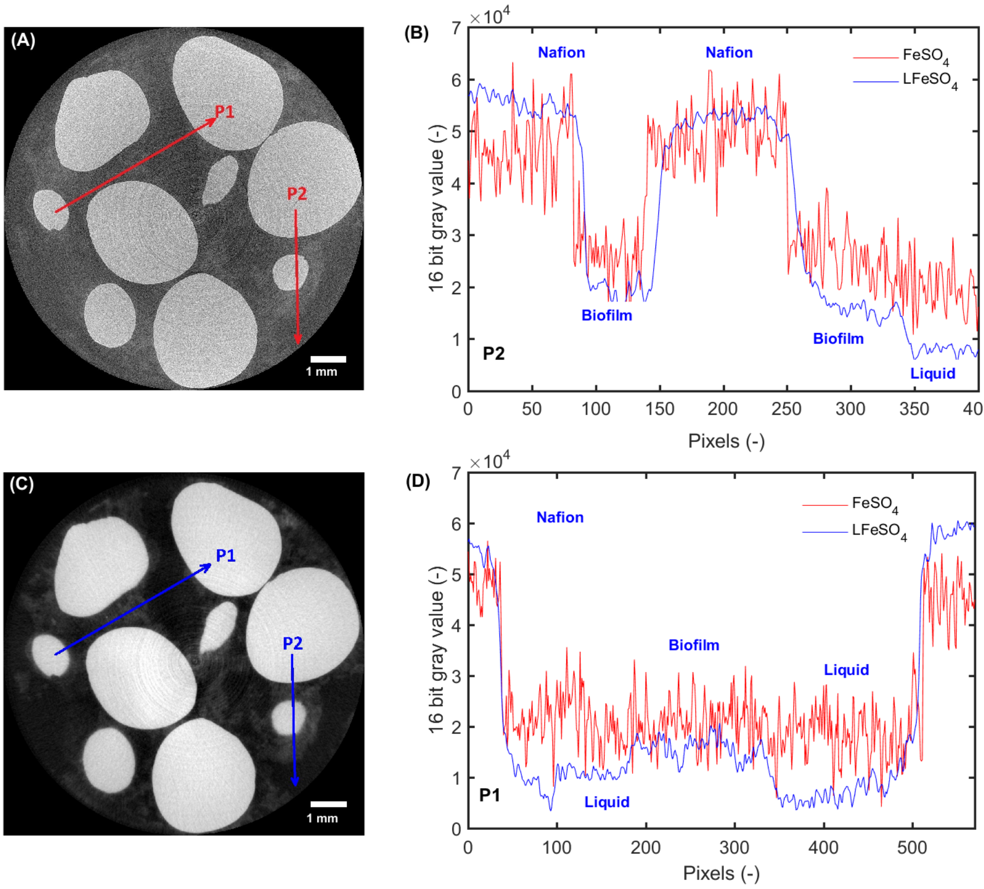

Figure 3.3: Slices from the $FeSO_4$ (A) and $LFeSO_4$ (C) datasets. For the sake of comparison, both images were normalized with 0.4 % of the pixels saturated. The two red resp. blue arrows indicate the location and direction at which the gray value profiles are extracted. The scale bar represents 1 mm. Gray value profile for the first (P1, (D) and the second location P2, (B)). The profiles are labeled with the different phases observed.

agent. After reconstruction of the $LFeSO_4$ dataset, the image contrast was enhanced so that the Nafion grains were mostly saturated. A curvature-driven diffusion filter was then run in Avizo® (5 iterations and standard parameters: sharpness = 0.9, anisotropy = 0.6), reducing the noise while preserving the edges. Fig 3.4A shows a slice (located at the middle of the stack) obtained after the filtering and Fig 3.4C (red) shows the 8 bit gray value histogram obtained for the whole stack. On that histogram, the peaks corresponding to the liquid and Nafion phases are clearly identifiable. The liquid phase peak exhibits a strong shoulder on its right side, that corresponds to the biofilm phase. The overlap between the liquid and biofilm regions as well as the strong tail exhibited by the biofilm shoulder are due to the heterogeneous gray value distribution of the biofilm region (see Fig 3.4A). In order to segment these two regions, we assumed two overlapping peaks for the biofilm and the liquid phase and fixed a threshold at the inflection point located between the liquid phase peak and the biofilm shoulder. The determination of this inflection point is related to some uncertainty (see Fig 1. in the Supplementary Information). We therefore performed a simple sensitivity analysis by defining three different thresholds at the center and lower resp. higher end of the shoulder region. These thresholds are illustrated in purple, resp. yellow and green in Fig 3.4C). The gray values used for the sensitivity analysis correspond to ca. 10% of the central gray value (purple). For all threshold values, a thresholding was performed in VG Max®. Then, a closing operation was done in order to fill in small voids that are considered as noise from each phase. A region growing algorithm was used to identify disconnected segments of biofilm or liquid (e.g. pores in the biofilm or floating biofilm bits) that were merged into the surrounding phase. Since we observed the formation and displacement of air bubbles during the flushing out of the remaining iron or the injection of $BaSO_4$, the air bubbles were segmented and merged into the liquid phase. The result of this segmentation is shown in Fig 3.4D).

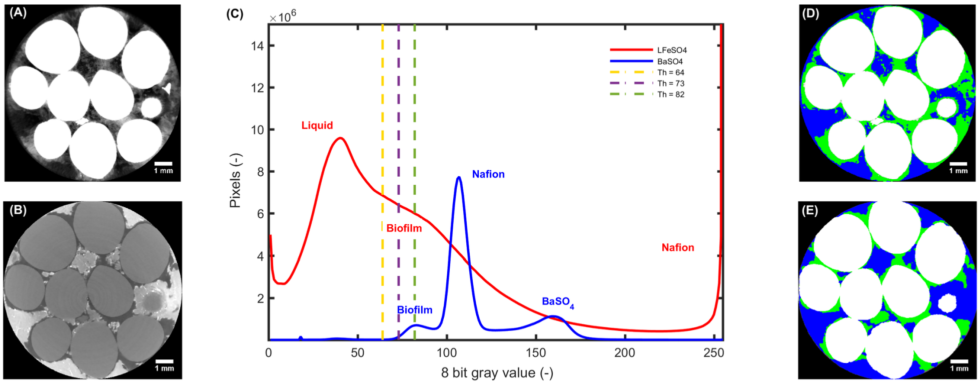

Figure 3.4: Middle slices (filtered prior to segmentation according information in Table 3.1) for the $LFeSO_4$ (A) and $BaSO_4$ (B) datasets. The corresponding 8 bit gray value histograms are shown in C) for the $BaSO_4$ (blue) dataset and for the $LFeSO_4$ (red) dataset after contrast enhancement and application of the 3D curvature-driven diffusive filter. For the $LFeSO_4$ dataset, the vertical dashed lines in yellow, purple and green correspond to isosurface values of 64, 73 and 82 used for the segmentation and the corresponding sensitivity analysis. The peaks corresponding to the different phases are annotated. (D) and (E) show the segmented datasets where the solid, liquid and biofilm phases are color coded in white, blue and green respectively. The scale bar represents 1 mm.

Fig 3.4B shows a slice (same location than for Fig 3.4A, in the middle of the stack) of the $BaSO_4$ dataset obtained after application of the same 3D curvature driven filter. The corresponding histogram of the $BaSO_4$ dataset (see Fig 3.4C, in blue) shows a peak for the Nafion grains (central peak) and two additional peaks for the biofilm and the liquid phase. As it it shown in Fig 3.4B, due to the high attenuation of $BaSO_4$, this dataset exhibited some beam hardening artifacts. These artifacts were overcome in the segmentation by using the ImageJ implementation (Leemann et al., 2010; Muench, 2015) of a seeded region growing algorithm (Adams and Bischof, 1994) providing satisfying segmentation of the solid phase (see Supplementary Information for details). The liquid and biofilm phases were then obtained by thresholding after using the segmented solid phase as a mask. Fig 3.4. E shows the corresponding segmented result. A sensitivity analysis was performed for that thresholding and is presented in the Supplementary Information. Finally, the control sample was imaged and segmented following the same approach as for the $LFeSO_4$ dataset.

Registration of the two different datasets

A registration (volumetric image alignment onto a single coordinate system) of the two different tomograms was performed in order to compare locally (e.g. conditional probabilities) the volumetric fractions obtained from the different datasets. To begin with, the resolution of both datasets was matched. Then, a coordinate alignment process was performed in Matlab® on the solid phases, because these are the most similar phases in both datasets. Here, the *imregister* function with default parameters was used for finding and optimizing an affine geometric transformation minimizing a mean square error metric. The optimization of the registration was performed using a regular step gradient descent method. All the results and analyses presented in the following were obtained from the registered datasets.

3.3 Results

Fig 3.4. (A) and (B) show slices of the $LFeSO_4$ and $BaSO_4$ datasets obtained after filtering with a 3D curvature-driven filter. On both images, the biofilm is visible (light gray zones in)A) and the darkest ones in (B) but it seems that there is substantially more biofilm on image (A). The biofilm gray values in (A) exhibit an important heterogeneity. On this image, it is possible to identify darker zones belonging to the liquid phase and lighter ones to the biofilm. Fig.3.4 (D) and (E) show the corresponding segmented slices where the segmented biofilm phases obtained with both contrast agents roughly overlap. However, on both the pre-processed (Lorentzian when used and 3D curvature-driven filtering) and segmented images, some biofilm regions locally do not match. Fig 3.5. shows 3D renderings of the solid phase (Nafion grains) and the segmented datasets which reveal that the volume fraction of the biofilm (green) is much smaller for the $BaSO_4$ dataset. Qualitatively, the biofilm appears more patchy for the $BaSO_4$ than for the $LFeSO_4$ dataset. For the latter, the biofilm exhibits complex corrugated shapes that are more interconnected. It appears that greater detail of the biofilm morphology is resolved when $LFeSO_4$ is used as a contrast enhancing agent.

Fig 3.6. shows volumetric fraction profiles along the streamwise direction for the $LFeSO_4$ and for the $BaSO_4$ datasets. The average total volumetric fractions obtained are given in the legend. The profiles obtained for the solid phase of both samples show a very good overlap and have volumetric fractions that are relatively close, at about 60% of the whole volume of the sample. The oscillations of these values present a wave length of ca. 2.5 mm approximately corresponding to the grain size diameter, indicating that there is some

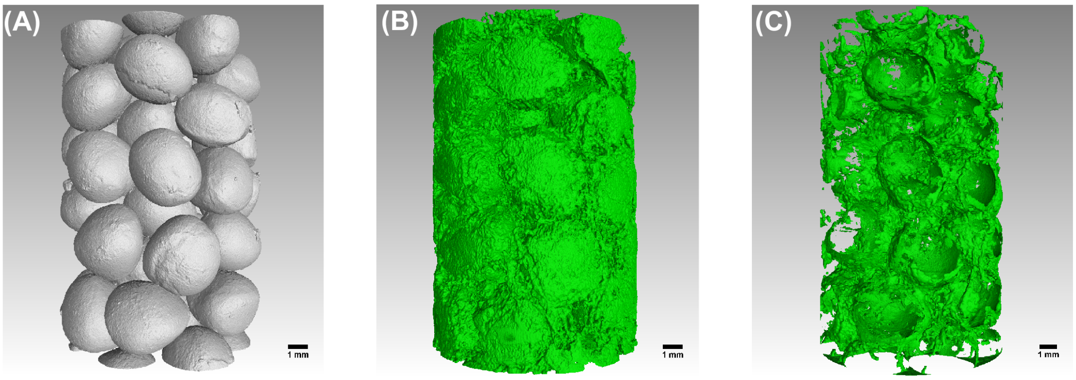

Figure 3.5: Three-dimensional renderings of the solid phase (left), of the sample imaged with $FeSO_4$ (center) and barium suflate (right) as a contrast-enhancing agents.

degree of order in the packing. While there is a good matching for the volumetric fractions profiles obtained for both solid phases, it is not the case for the remaining phases. For instance, the biofilm fraction obtained for the $LFeSO_4$ dataset is about three times larger than for the $BaSO_4$ dataset. The shaded region is delimited by the lower and higher thresholds used for the sensitivity analysis. Over the whole column, the biofilm volumetric fraction obtained with $FeSO_4$ is consistently larger than for the $BaSO_4$ dataset (about twice as much).

To study how the phases overlap in 3D space, we locally computed the conditional probabilities of the phase overlap between the two different datasets, e.g. the percentage of a first phase corresponding to the same phase in a second one ($P(A \mid B) = P(B \cap A)/P(B)$) (see Table 3.2). With more than 90 % in both cases, the overlap is very good for the solid phases. Again, the remaining phases exhibit substantial differences. For the biofilm phase, the intersection of voxels identified as biofilm in both $BaSO_4$ and $LFeSO_4$ datasets only correspond to ca. 25% against ca. 70% for the opposite case. This indicates two different aspects: first that locally the volumetric fraction of the biofilm obtained for the $LFeSO_4$ dataset is substantially higher than for the $BaSO_4$ dataset. Secondly, as biofilm patches detached upon the $BaSO_4$ injection, they might have reattached or filtered at some other locations within the column where there is no biofilm visible in the $LFeSO_4$ dataset.

Table 3.2: Conditioned probabilities that a given phase in the FeSO4 data locally belongs to the same phase in the BaSO4 data computed for the solid (S), liquid (L) and biofilm (BF) phases for the registered Lorentz filtered $FeSO_4$ and $BaSO_4$ datasets.

Conditional probability	Percentage
$P(S_{BaSO_4} \mid S_{LFeSO_4})$	93.85
$P(S_{LFeSO_4} \mid S_{BaSO_4})$	98.18
$P(L_{BaSO_4} \mid L_{LFeSO_4})$	88.20
$P(L_{LFeSO_4} \mid L_{BaSO_4})$	54.25
$P(BF_{BaSO_4} \mid BF_{LFeSO_4})$	24.74
$P(BF_{LFeSO_4} \mid BF_{BaSO_4})$	72.57

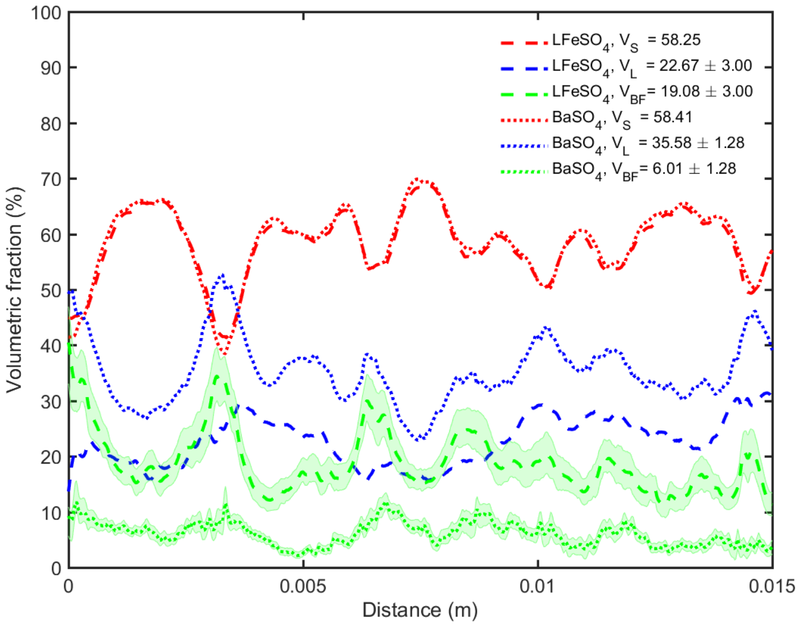

Figure 3.6: Profiles of the volumetric fractions (S: solid, L: liquid, BF: biofilm) obtained for the different datasets ($BaSO_4$: small dashes, $FeSO_4$: longer dashes). The shaded region is defined by the results obtained for the threshold sensitivity analysis. For the sake of clarity, the results of this sensitivity analysis are not added to the liquid phases. The average volumetric fractions (in percent) for the different phases (Solid V_S, Liquid V_L, Biofilm V_{BF}) obtained with the two different contrast-enhancing agents is given in the legend.

The control sample was treated in the same way than the $FeSO_4$ data set, except for the fact that it was not inoculated with the bacterial inoculum and that no growth medium was added for the 7 days. The image processing (filters, reconstruction and segmentation) used was also the same as the one used for the $FeSO_4$ data set. The aim of this control was to estimate the concentration of colloidal $FeSO_4$ in the biofilm itself. For the control, a colloidal volumetric fraction of about 10% was obtained, indicating that the iron equalled ca. 54% of the volumetric fraction of the biofilm. This indicates that the inorganic content of the biofilm cultivated here is fairly high.

3.4 Discussion

In this study, the combination of a non-destructive contrast agent, a long STD and Lorentzian filtering revealed intact 3D biofilm morphologies in porous media. This particular combination of contrast agent and imaging tools borrowed from phase contrast imaging allowed to substantially reduce noise and improve the contrast of the sample containing materials with small attenuation coefficient differences.

The different volumetric fraction obtained for the $BaSO_4$ and $FeSO_4$ contrast agents could be explained by the following reasons: uncertainty related to the segmentation or the registration, partial volume effects due to the different imaging resolution and interactions between the $BaSO_4$ suspension and the biofilm (e.g. penetration or invasion of the biofilm and biofilm detachment upon the introduction of the contrast agent). The volumetric fraction obtained for the biofilm is sensitive to the threshold considered, but in all cases stays consistently higher than the $BaSO_4$ volumetric fraction. The good agreement of both the average volumetric fractions and volumetric fractions profiles of the solid phase illustrated in Fig 3.6. allows us to rule out the uncertainty related to the registration or the partial volume effects as a main cause for the mentioned substantial differences. Therefore, penetration of the smallest $BaSO_4$ particles within the biofilm and biofilm detachment (as illustrated schematically in Fig 3.7.) appear to be at the root of the differences observed.

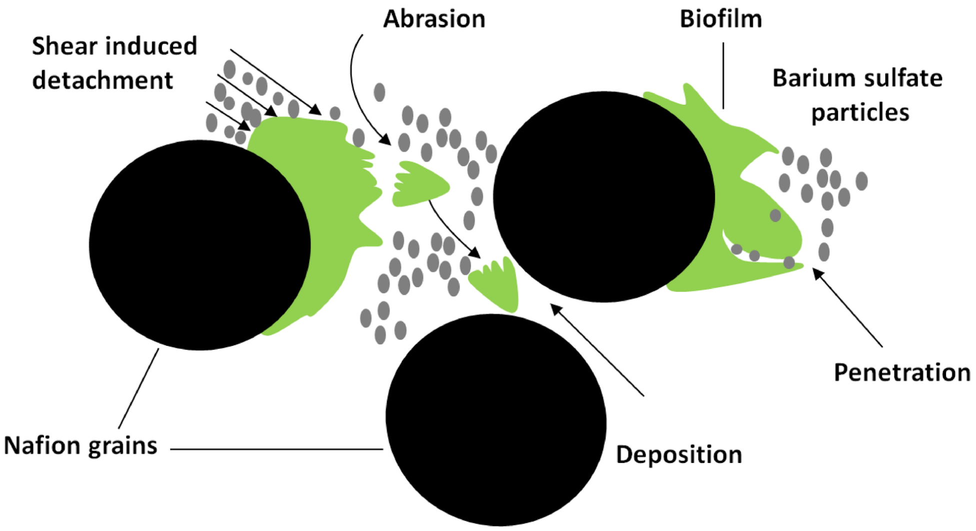

Figure 3.7: Schematic of biofilm detachment mechanisms during $BaSO_4$ injection.

About 20% of the $BaSO_4$ particles used have a diameter smaller than 0.5 μm and are smaller than the largest biofilm pores expected (Stoodley et al., 1994). In the present case, it is realistic to assume that a portion of the smallest $BaSO_4$ particles could enter the biofilm channels (see Fig 3.7.) and therefore labelling the parts of the biofilm as liquid.

As mentioned earlier, biofilm detachment was observed during the injection of $BaSO_4$ (see Supplementary Information). This observation was already noted previously in another study (Davit et al., 2011). We estimated the average wall shear stress exerted by the $BaSO_4$ suspension on the biofilm assuming a power law fluid flowing in a simplistic representation of an average pore in our system. Although the flow rate was 10 times smaller during the $BaSO_4$ injection than the growth flow rate, we found ca. 3 times higher wall shear stresses in the BaSO4 injection stage due to the high viscosity and shear thinning properties of the BaSO4 suspension and (see Supplementary Information). Given the extremely wide range of shear rates taking place in the actual porous medium (Holzner et al., 2015), locally the wall shear stresses ratio might be significantly higher, causing the detachment observed. In such a case, the rheological properties of the $BaSO_4$ suspension should not be neglected.

Derlon et al. (2008) and Rochex et al. (2009) showed that biofilm form stratified structures and that the biofilm resistance to shear or shear strength (Stoodley et al., 2002) is dependent on the wall-normal location within the biofilm. Möhle et al. (2007) showed that by increasing the biofilm shear strength, high concentrations of iron in biofilms had a positive effect on the biofilm stability. Here, lower shear strength regions of the biofilm probably detached upon $BaSO_4$ injection and the basal layers with higher shear strength remain attached. Abrasion of biofilm by particles is another known detachment mechanism (Derlon et al., 2008). It is not excluded that $BaSO_4$ particles-biofilm interactions also contributed to the detachment observed. Fig 3.7. illustrates the different mechanisms potentially causing the detachment. The shear and abrasion induced detachment explain the differences in the overall and local biofilm volumetric fractions observed. In Table 3.2, the low probability of the biofilm phase obtained with $BaSO_4$ to also belong to the biofilm phase obtained with $FeSO_4$ might also point to the deposition or filtration of some detached biofilm patches further upstream within the column.

Table 3.3 summarizes key points on which the method by Davit et al. (2011) and the method presented here can be evaluated. The $FeSO_4$-based method allows to image biofilms in porous media using a non-toxic and non-destructive contrast agent on a X-ray lab source with movable detector. The combination of long STD and Lorentzian filter allows to substantially increase the signal to noise ratio. As mentioned earlier, the colloidal fraction observed for the control dataset (LControl) is not negligible. Nevertheless, the detected biofilm fraction in the LFeSO4 experiment is much higher which confirms that the higher volumetric fraction observed in the latter case is due to biological activity, either due to the biofilm itself or to precipitation induced by bacterial activity, (e.g. iron oxidation, sulfide salts production, see Blowes et al. (2000) and Weiner (2013)). The $BaSO_4$-based method provides clear contrast between the different phases but interactions of the $BaSO_4$ suspension with the biofilm induce substantial biofilm detachment. In both cases, some uncertainty remains related to the segmentation, which could however be quantified.

Table 3.3: Evaluation of the presented method and another existing one for imaging biofilms in porous media.

	$LFeSO_4$	$BaSO_4$
Biofilm integrity	non-destructive	can cause detachment during $BaSO_4$ injection
Biofilm toxicity	none, but high inorganic content biofilm	none
Lab XCT requirements	movable detector	none
Imaging issues	High signal to noise ratio	Prone to beam hardening
Reconstruction requirements	Lorenztian filter	none
Segmentation	Thresholding	Combination of region growing and thresholding

3.5 Conclusion

In this paper, we presented an innovative method to image biofilms in porous media combining iron sulfate as a contrast agent, a long STD and a Lorentzian filter. The non-toxic and non-destructive contrast agent was continuously added to the biofilm during the biofilm growth. The combination of using a large STD together with application of a Lorentzian Fourier filter allowed to exploit refraction effects. The reconstructed data showed a substantial reduction in noise and an increase in the contrast between materials exhibiting low attenuation coefficients differences, revealing the biofilm morphology. We found that in the porous medium and for the present growth conditions, the biofilm exhibits complex corrugated structures. We compared this method with an existing method using $BaSO_4$ as as a contrast agent for the exact same sample and observed some differences in the biofilm morphology obtained due to interactions between the biofilm and the $BaSO_4$. Namely, due to abrasion and shear detachment, more than 50% of the biofilm was washed out by the contrast agent emphasizing the need for non-destructive contrast agents for biofilm imaging in porous media. The method presented in this study delivers 3D biofilm morphologies in porous media non-destructively on a X-ray lab source. Possible applications are studies addressing the interplay between biofilms, their morphology and local hydrodynamic and mass transport processes in realistic porous media models.

Acknowledgments

Financial support is acknowledged from the Swiss National Science Foundation (SNF grant number 144645) for M.C. and M.H. The authors thank Toni Blunschi for manufacturing the tubular reactor, Daniel Braun and Lucien Biolley for providing some of the hardware necessary for this study as well as Michele Griffa for some interesting discussions related to the segmentation. Part of this work has been performed by the use of the Empa Platform for Image Analysis (http://empa.ch/web/s499/software-/-imaging-platform) at Empa's Center for X-ray Analytics. The authors declare that there is no conflict of interest.

Bibliography

Adams, R. and Bischof, L. (1994). Seeded region growing. *IEEE Transactions on Pattern Analysis and Machine Intelligence*, 16(6):641–647. pages

Anderson, R. T., Vrionis, H. A., Ortiz-Bernad, I., Resch, C. T., Long, P. E., Dayvault, R., Karp, K., Marutzky, S., Metzler, D. R., Peacock, A., White, D. C., Lowe, M., and Lovley, D. R. (2003). Stimulating the in situ activity of geobacter species to remove uranium from the groundwater of a uranium-contaminated aquifer. *Applied and Environmental Microbiology*, 69(10):5884–5891. pages

Arhatari, B. D., Gates, W. P., Eshtiaghi, N., and Peele, A. G. (2010). Phase retrieval tomography in the presence of noise. *Journal of Applied Physics*, 107(3):034904. pages

Battin, T. J., Sloan, W. T., Kjelleberg, S., Daims, H., Head, I. M., Curtis, T. P., and Eberl, L. (2007). Microbial landscapes: new paths to biofilm research. *Nat Rev Micro*, 5(1):76–81. pages

Baveye, P., Vandevivere, P., Hoyle, B. L., DeLeo, P. C., and de Lozada, D. S. (1998). Environmental impact and mechanisms of the biological clogging of saturated soils and aquifer materials. *Critical Reviews in Environmental Science and Technology*, 28(2):123–191. pages

Beltran, M. A., Paganin, D. M., Siu, K. K. W., Fouras, A., Hooper, S. B., Reser, D. H., and Kitchen, M. J. (2011). Interface-specific x-ray phase retrieval tomography of complex biological organs. *Physics in Medicine and Biology*, 56(23):7353. pages

Beltran, M. A., Paganin, D. M., Uesugi, K., and Kitchen, M. J. (2010). 2d and 3d x-ray phase retrieval of multi-material objects using a single defocus distance. *Optics Express*, 18(7):6423–6436. pages

Benner, S. G., Blowes, D. W., Ptacek, C. J., and Mayer, K. U. (2002). Rates of sulfate reduction and metal sulfide precipitation in a permeable reactive barrier. *Applied Geochemistry*, 17(3):301–320. pages

Blauert, F., Horn, H., and Wagner, M. (2015). Time-resolved biofilm deformation measurements using optical coherence tomography. *Biotechnology and Bioengineering*, 112(9):1893–1905. pages

Blowes, D. W., Ptacek, C. J., Benner, S. G., McRae, C. W. T., Bennett, T. A., and Puls, R. W. (2000). Treatment of inorganic contaminants using permeable reactive barriers1. *Journal of Contaminant Hydrology*, 45(1–2):123–137. pages

Bouwer, H. (2002). Artificial recharge of groundwater: hydrogeology and engineering. *Hydrogeology Journal*, 10(1):121–142. pages

Burvall, A., Lundström, U., Takman, P. A. C., Larsson, D. H., and Hertz, H. M. (2011). Phase retrieval in x-ray phase-contrast imaging suitable for tomography. *Optics Express*, 19(11):10359–10376. pages

Costerton, J. W., Stewart, P. S., and Greenberg, E. P. (1999). Bacterial biofilms: A common cause of persistent infections. *Science*, 284(5418):1318–1322. pages

Cunningham, A. B., Characklis, W. G., Abedeen, F., and Crawford, D. (1991). Influence of biofilm accumulation on porous media hydrodynamics. *Environmental Science and Technology*, 25(7):1305–1311. pages

Davit, Y., Debenest, G., Wood, B. D., and Quintard, M. (2010). Modeling non-equilibrium mass transport in biologically reactive porous media. *Advances in Water Resources*, 33(9):1075–1093. pages

Davit, Y., Iltis, G., Debenest, G., Veran-Tissoires, S., Wildenschild, D., Gerino, M., and Quintard, M. (2011). Imaging biofilm in porous media using x-ray computed microtomography. *Journal of Microscopy*, 242(1):15–25. pages

Derlon, N., Massé, A., Escudié, R., Bernet, N., and Paul, E. (2008). Stratification in the cohesion of biofilms grown under various environmental conditions. *Water Research*, 42(8–9):2102–2110. pages

Derlon, N., Peter-Varbanets, M., Scheidegger, A., Pronk, W., and Morgenroth, E. (2012). Predation influences the structure of biofilm developed on ultrafiltration membranes. *Water Research*, 46(10):3323–3333. pages

DigitalRocks (2017). Biofilm imaging in porous media by laboratory x-ray tomography: Combining a non-destructive contrast agent with propagation-based phase-contrast imaging tools. `https://github.com/3dptv`. pages

Downie, H., Holden, N., Otten, W., Spiers, A. J., Valentine, T. A., and Dupuy, L. X. (2012). Transparent soil for imaging the rhizosphere. *PLoS ONE*, 7(9):e44276. pages

Dupin, H. J. and McCarty, P. L. (2000). Impact of colony morphologies and disinfection on biological clogging in porous media. *Environmental Science and Technology*, 34(8):1513–1520. pages

Ebigbo, A., Helmig, R., Cunningham, A. B., Class, H., and Gerlach, R. (2010). Modelling biofilm growth in the presence of carbon dioxide and water flow in the subsurface. *Advances in Water Resources*, 33(7):762–781. pages

Feldkamp, L. A., Davis, L. C., and Kress, J. W. (1984). Practical cone-beam algorithm. *Journal of the Optical Society of America A*, 1(6):612–619. pages

Golfier, F., Wood, B. D., Orgogozo, L., Quintard, M., and Buès, M. (2009). Biofilms in porous media: Development of macroscopic transport equations via volume averaging with closure for local mass equilibrium conditions. *Advances in Water Resources*, 32(3):463–485. pages

Graf von der Schulenburg, D. A., Akpa, B. S., Gladden, L. F., and Johns, M. L. (2008). Non-invasive mass transfer measurements in complex biofilm-coated structures. *Biotechnology and Bioengineering*, 101(3):602–608. pages

Griebler, C. and Lueders, T. (2009). Microbial biodiversity in groundwater ecosystems. *Freshwater Biology*, 54(4):649–677. pages

Gureyev, T. E., Paganin, D. M., Myers, G. R., Nesterets, Y. I., and Wilkins, S. W. (2006). Phase-and-amplitude computer tomography. *Applied Physics Letters*, 89(3):034102. pages

Hall-Stoodley, L., Costerton, J. W., and Stoodley, P. (2004). Bacterial biofilms: from the natural environment to infectious diseases. *Nat Rev Micro*, 2(2):95–108. pages

Holzner, M., Morales, V. L., Willmann, M., and Dentz, M. (2015). Intermittent lagrangian velocities and accelerations in three-dimensional porous medium flow. *Physical Review E*, 92(1):013015. pages

Iltis, G. C., Armstrong, R. T., Jansik, D. P., Wood, B. D., and Wildenschild, D. (2011). Imaging biofilm architecture within porous media using synchrotron-based x-ray computed microtomography. *Water Resources Research*, 47(2):W02601. pages

Ivankovic, T., Rolland du Roscoat, S., Geindreau, C., Séchet, P., Huang, Z., and Martins, J. M. F. (2016). Development and evaluation of an experimental protocol for 3-d visualization and characterization of the structure of bacterial biofilms in porous media using laboratory x-ray tomography. *Biofouling*, 32(10):1235–1244. pages

Kapellos, G. E., Alexiou, T. S., and Payatakes, A. C. (2010). Theoretical modeling of fluid flow in cellular biological media: An overview. *Mathematical Biosciences*, 225(2):83–93. pages

Kone, T., Golfier, F., Orgogozo, L., Oltéan, C., Lefèvre, E., Block, J. C., and Buès, M. A. (2014). Impact of biofilm-induced heterogeneities on solute transport in porous media. *Water Resources Research*, 50(11):9103–9119. pages

Lappin-Scott, H. M., Cusack, F., and Costerton, J. W. (1988). Nutrient resuscitation and growth of starved cells in sandstone cores: a novel approach to enhanced oil recovery. *Applied and Environmental Microbiology*, 54(6):1373–1382. pages

Leemann, A., Loser, R., and Münch, B. (2010). Influence of cement type on itz porosity and chloride resistance of self-compacting concrete. *Cement and Concrete Composites*, 32(2):116–120. pages

Li, L., Benson, C. H., and Lawson, E. M. (2005). Impact of mineral fouling on hydraulic behavior of permeable reactive barriers. *Ground Water*, 43(4):582–596. pages

Mayo, S. C., Davis, T. J., Gureyev, T. E., Miller, P. R., Paganin, D., Pogany, A., Stevenson, A. W., and Wilkins, S. W. (2003). X-ray phase-contrast microscopy and microtomography. *Optics Express*, 11(19):2289–2302. pages

Meckenstock, R. U., Elsner, M., Griebler, C., Lueders, T., Stumpp, C., Aamand, J., Agathos, S. N., Albrechtsen, H.-J., Bastiaens, L., Bjerg, P. L., Boon, N., Dejonghe, W., Huang, W. E., Schmidt, S. I., Smolders, E., Sørensen, S. R., Springael, D., and van Breukelen, B. M. (2015). Biodegradation: Updating the concepts of control for microbial cleanup in contaminated aquifers. *Environmental Science and Technology*, 49(12):7073–7081. pages

Möhle, R. B., Langemann, T., Haesner, M., Augustin, W., Scholl, S., Neu, T. R., Hempel, D. C., and Horn, H. (2007). Structure and shear strength of microbial biofilms as determined with confocal laser scanning microscopy and fluid dynamic gauging using a novel rotating disc biofilm reactor. *Biotechnology and Bioengineering*, 98(4):747–755. pages

Milferstedt, K., Pons, M. N., and Morgenroth, E. (2009). Analyzing characteristic length scales in biofilm structures. *Biotechnology and Bioengineering*, 102(2):368–379. pages

Mitchell, A. C., Phillips, A., Schultz, L., Parks, S., Spangler, L., Cunningham, A. B., and Gerlach, R. (2013). Microbial caco3 mineral formation and stability in an experimentally simulated high pressure saline aquifer with supercritical co2. *International Journal of Greenhouse Gas Control*, 15:86–96. pages

Muench, B. (2015). Seeded region growing algorithm. Accessed: 2016-08-23. pages

Myers, G. R., Gureyev, T. E., Paganin, D. M., and Mayo, S. C. (2008). The binary dissector: phase contrast tomography of two- and three-material objects from few projections. *Optics Express*, 16(14):10736–10749. pages

Omoregie, E. O., Couture, R.-M., Van Cappellen, P., Corkhill, C. L., Charnock, J. M., Polya, D. A., Vaughan, D., Vanbroekhoven, K., and Lloyd, J. R. (2013). Arsenic bioremediation by biogenic iron oxides and sulfides. *Applied and Environmental Microbiology*, 79(14):4325–4335. pages

Orgogozo, L., Golfier, F., Buès, M., and Quintard, M. (2010). Upscaling of transport processes in porous media with biofilms in non-equilibrium conditions. *Advances in Water Resources*, 33(5):585–600. pages

Paganin, D. (2006). *Coherent x-ray optics*, page 411. Oxford University Press. pages

Paganin, D., Mayo, S. C., Gureyev, T. E., Miller, P. R., and Wilkins, S. W. (2002). Simultaneous phase and amplitude extraction from a single defocused image of a homogeneous object. *Journal of Microscopy*, 206(1):33–40. pages

Paulsen, J. E., Oppen, E., and Bakke, R. (1997). Biofilm morphology in porous media, a study with microscopic and image techniques. *Water Science and Technology*, 36(1):1. pages

Peszynska, M., Trykozko, A., Iltis, G., Schlueter, S., and Wildenschild, D. (2016). Biofilm growth in porous media: experiments, computational modeling at the porescale, and upscaling. *Advances in Water Resources*, 95:288–301. pages

Pintelon, T. R. R., Graf von der Schulenburg, D. A., and Johns, M. L. (2009). Towards optimum permeability reduction in porous media using biofilm growth simulations. *Biotechnology and Bioengineering*, 103(4):767–779. pages

Plouraboué, F., Cloetens, P., Fonta, C., Steyer, A., Lauwers, F., and Marc-Vergnes, J. P. (2004). X-ray high-resolution vascular network imaging. *Journal of Microscopy*, 215(2):139–148. pages

Rochex, A., Massé, A., Escudié, R., Godon, J.-J., and Bernet, N. (2009). Influence of abrasion on biofilm detachment: evidence for stratification of the biofilm. *Journal of Industrial Microbiology & Biotechnology*, 36(3):467–470. pages

Rolland du Roscoat, S., Martins, J. M. F., Séchet, P., Vince, E., Latil, P., and Geindreau, C. (2014). Application of synchrotron x-ray microtomography for visualizing bacterial biofilms 3d microstructure in porous media. *Biotechnology and Bioengineering*, 111(6):1265–1271. pages

Rusconi, R., Lecuyer, S., Guglielmini, L., and Stone, H. A. (2010). Laminar flow around corners triggers the formation of biofilm streamers. *Journal of The Royal Society Interface*, 7(50):1293–1299. pages

Sand, W. (2003). Microbial life in geothermal waters. *Geothermics*, 32(4–6):655–667. pages

Seymour, J. D., Gage, J. P., Codd, S. L., and Gerlach, R. (2004). Anomalous fluid transport in porous media induced by biofilm growth. *Physical Review Letters*, 93(19):198103. pages

Sharp, R. R., Cunningham, A. B., Komlos, J., and Billmayer, J. (1999). Observation of thick biofilm accumulation and structure in porous media and corresponding hydrodynamic and mass transfer effects. *Water Science and Technology*, 39(7):195. pages

Stoodley, P., Cargo, R., Rupp, J. C., Wilson, S., and Klapper, I. (2002). Biofilm material properties as related to shear-induced deformation and detachment phenomena. *Journal of Industrial Microbiology and Biotechnology*, 29(6):361–367. pages

Stoodley, P., deBeer, D., and Lewandowski, Z. (1994). Liquid flow in biofilm systems. *Applied and Environmental Microbiology*, 60(8):2711–2716. pages

Stoodley, P., Dodds, I., De Beer, D., Scott, H. L., and Boyle, J. D. (2005). Flowing biofilms as a transport mechanism for biomass through porous media under laminar and turbulent conditions in a laboratory reactor system. *Biofouling*, 21(3-4):161–168. pages

Taylor, S. and Jaffé, P. (1990). Biofilm growth and the related changes in the physical properties of a porous medium: 1. experimental investigation. *Water Resources Research*, 26(9):2153–2159. pages

Teixeira, S., Vieira, M. N., Marques, J. E., and Pereira, R. (2014). Bioremediation of an iron-rich mine effluent by lemna minor. *International Journal of Phytoremediation*, 16(12):1228–1240. pages

Thullner, M., Zeyer, J., and Kinzelbach, W. (2002). Influence of microbial growth on hydraulic properties of pore networks. *Transport in Porous Media*, 49(1):99–122. pages

Vayenas, D. V., Michalopoulou, E., Constantinides, G. N., Pavlou, S., and Payatakes, A. C. (2002). Visualization experiments of biodegradation in porous media and calculation of the biodegradation rate. *Advances in Water Resources*, 25(2):203–219. pages

Vogt, S. J., Sanderlin, A. B., Seymour, J. D., and Codd, S. L. (2013). Permeability of a growing biofilm in a porous media fluid flow analyzed by magnetic resonance displacement-relaxation correlations. *Biotechnology and Bioengineering*, 110(5):1366–1375. pages

von der Schulenburg, D. A. G., Pintelon, T. R. R., Picioreanu, C., Van Loosdrecht, M. C. M., and Johns, M. L. (2009). Three-dimensional simulations of biofilm growth in porous media. *AIChE Journal*, 55(2):494–504. pages

Wagner, M., Manz, B., Volke, F., Neu, T. R., and Horn, H. (2010a). Online assessment of biofilm development, sloughing and forced detachment in tube reactor by means of magnetic resonance microscopy. *Biotechnology and Bioengineering*, 107(1):172–181. pages

Wagner, M., Taherzadeh, D., Haisch, C., and Horn, H. (2010b). Investigation of the mesoscale structure and volumetric features of biofilms using optical coherence tomography. *Biotechnology and Bioengineering*, 107(5):844–853. pages

Weiner, E. R. (2013). *Applications of Environmental Aquatic Chemistry*, page 592. CRC Press. pages

Wildenschild, D. and Sheppard, A. P. (2013). X-ray imaging and analysis techniques for quantifying pore-scale structure and processes in subsurface porous medium systems. *Advances in Water Resources*, 51:217–246. pages

Wildenschild, D., Vaz, C. M. P., Rivers, M. L., Rikard, D., and Christensen, B. S. B. (2002). Using x-ray computed tomography in hydrology: systems, resolutions, and limitations. *Journal of Hydrology*, 267(3–4):285–297. pages

Wilkins, S., T.E., G., Gao, D., Pogany, A., and Stevenson, A. (1996). Phase-contrast imaging using polychromatic hard x-rays. *Nature (London)*, 384(6607):335–338. pages

Xi, C., Marks, D., Schlachter, S., Luo, W., and Boppart, S. A. (2006). High-resolution three-dimensional imaging of biofilm development using optical coherence tomography. *Journal of Biomedical Optics*, 11(3):034001–034001–6. pages

Chapter 4

Supplementary material to Chapter 3

4.1 Segmentation of the $LFeSO_4$ data set

Fig.4.1 shows an extract of the histogram of the $LFeSO_4$ data set after the Lorentzian filtering and the pre-processing step (contrast enhancement and 3D curvature-driven diffusive filter). The second derivative of the histogram is taken to determine the gray value that separates the biofilm phase from the liquid phase (see Fig. 4.1, green curve). The facts that the second derivative intersects several times the horizontal axis shows that there is some uncertainty related to the inflection point determination. The yellow, purple and green dashed vertical lines represent the three different 8 bit gray value thresholds of 64, 73 and 82 chosen in order to take this uncertainty into account. These three different threhsolds allow to assess the uncertainty of the inflection point determination on the final segmentation. Fig.4.2 shows contours of the interface between the liquid and biofilm at the three selected gray values on a vertical cross section of the sample. Fig.4.2A) is used as reference for an unobstructed view of the cross section. Fig. 4.2 B-D shows the contour at gray value thresholds of 64, 73 and 82, respectively.

4.2 Segmentation of the $BaSO_4$ data set

Fig.4.3 shows the histograms of the $BaSO_4$ data set (blue curve) and after substraction of the solid phase segmented with the seeded region growing algorithm (dashed blue). Due to the beam hardening artifacts caused by high attenuation of the $BaSO_4$ suspension, the

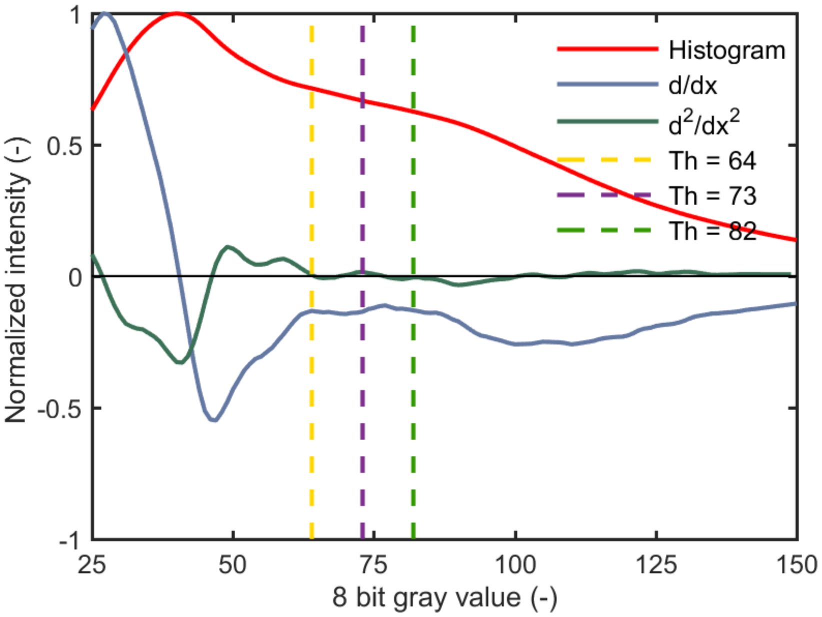

Figure 4.1: Extract of the gray value histogram for the $LFeSO_4$ data set (red). The first and second derivative of the histogram are shown in gray respectively dark green. The yellow, purple and light green dashed vertical lines at 8 bit gray value of 64, 73 and 82 represent the uncertainty zone considering the inflection point determination.

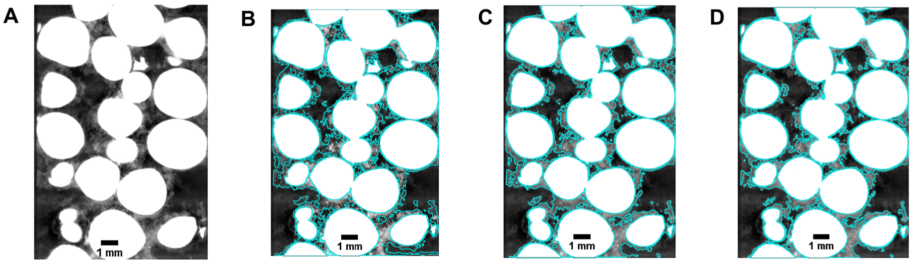

Figure 4.2: A) raw image of the $FeSO_4$ data set. B), C) and D) : biofilm phases obtained for the $FeSO_4$ data set based on 8 bit gray value thresholds of 64, resp. 73 and 82.

gray value distribution corresponding to $BaSO_4$ occupied pores (i.e., liquid) was strongy tailed. A threshold was visually defined for a value of 110 and a sensitivity analysis on that threshold value was performed. Similar to Fig.4.2, Fig.4.4 shows a cross section of the sample, with contours of the interface between the liquid and biofilm at three threshold gray values. Variation of the thresholded yielded in overall volumetric fraction variations of 1.28%. Thresholds outside this interval have also been tried but lead to inconsistent delineations of the biofilm-liquid boundary.

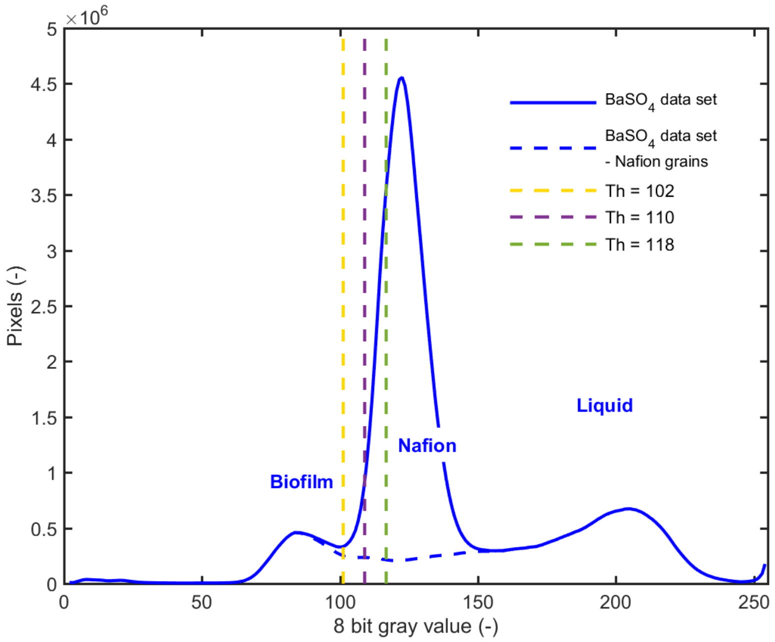

Figure 4.3: Histogram of the whole $BaSO_4$ data set (blue) and after the substraction of the solid phase obtained with the seeded region growin algorithm (dashed blue). The yellow, purple and green vertical lines represent the 8 bit gray value threhsolds of 102, 110 and 118 used for the sensitivity analysis.

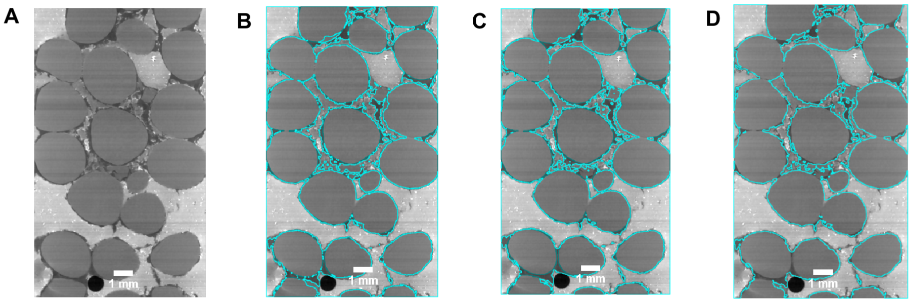

Figure 4.4: A) raw image of the $BaSO_4$ data set. B), C) and D) : liquid phases obtained for the $BaSO_4$ data set based on 8 bit gray value thresholds of 102, resp. 110 and 118.

4.3 Effect of the rheological properties of the $BaSO_4$ on the wall shear stress

Here, we evaluate the influence of the rheological properties of the $BaSO_4$ suspension on the wall shear stress induced on the biofilm during the injection of the contrast agent. In order to do so, we consider a pore of diameter D of 2.5 mm representative of the average pore size in the tubular reactor used in this study. We set the volumetric flow rate, so that the Reynolds number obtained in this system is of 2.5 as for the tubular reactor. We assume steady laminar flow and use cylindrical coordinates (R, θ, z). In that case, the wall shear stress τ_0 is a function of the pressure gradient dp/dz and of the pore's diameter D (Irgens, 2014):

$$\tau_0 = \frac{1}{4}\left|\frac{dp}{dz}\right| D \tag{4.1}$$

In this system, for the flow of the growth medium, the velocity profile is a parabolic function of the radius Irgens (2014):

$$v(r) = \frac{1}{16\eta_{H_2O}}\left|\frac{dp}{dz}\right|(D^2 - r2) \tag{4.2}$$

where R is the radius of the cylinder and we assume the growth medium to have the same dynamic viscosity than water. The volumetric flow rate is obtained by integration Irgens (2014):

$$Q = \frac{\pi}{128}\left|\frac{dp}{dz}\right|\frac{D^4}{\eta_{H_2O}} \tag{4.3}$$

Plouraboué et al. (2004) showed that the $BaSO_4$ suspension exhibit a shear-thinning. We model the rheology of the suspension as a power law fluid with::

$$\eta_{BaSO_4}(\dot{\gamma}) = K\dot{\gamma}^{n-1} \tag{4.4}$$

where the dynamic viscosity η is a function of the shear rate $\dot{\gamma}$. We use the data of Plouraboué et al. (2004) to approximate the flow consistency index $K = 0.048$ and the power law index $n = 0.6592$.

The velocity profile in pore is obtained combining the equation of motion in cylindrical coordinates and the definition of the dynamic viscosity made in Eq.4.4 (for details, see Irgens (2014)),:

$$v(r) = \frac{nD}{2(1+n)}\left(\left|\frac{dp}{dz}\right|\frac{D}{4K}\right)^{1/n}\left[1 - \left(\frac{2r}{D}\right)^{1/n+1}\right] \tag{4.5}$$

For the $BaSO_4$ suspension, the flow rate is obtained after integration yielding:

$$Q = \frac{\pi D^3}{8}\frac{n}{1+3n}\left(\left|\frac{dp}{dz}\right|\frac{D}{4K}\right)^{1/n} \tag{4.6}$$

In the experiments, the volumetric flow rate used for the injection of the $BaSO_4$ was 10 times smaller than during the biofilm culturing. For the pore considered here, the resulting pressure gradient is 2.7 times larger for the $BaSO_4$ suspension than for the growth medium. As the wall shear stress scales linearly with the pressure gradient (see Eq.4.1), the increase in pressure gradient results in an increase in shear stress by nearly a factor of 3 in the presence of BaSO4. The corresponding streamwise velocity profiles are shown in Fig.4.5. The gradients exhibited by the $BaSO_4$ velocity profiles are substantially smaller than for the growth medium (H_2O). It has to be considered that for the shear rates observed, the dynamic viscosity obtained using the power law fluid model is around 80 times higher than for water, explaining the high wall shear stresses obtained despite of the small velocity gradients. This increase of wall shear stress could explain the detachment observed.

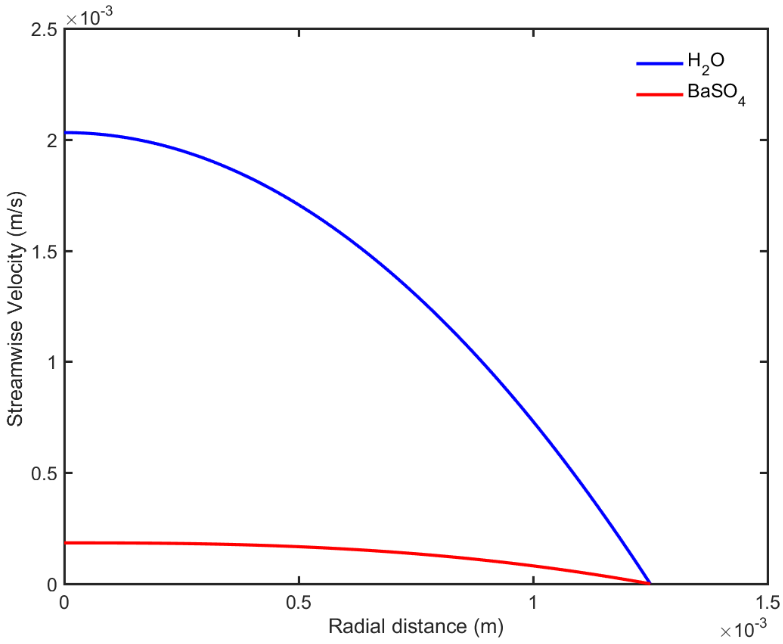

Figure 4.5: Velocity profile obtained for a flow in a representative pore for the growth solution and for the $BaSO_4$ suspension.

Moreover, it has to be noted that pore-scale velocities in porous media have an extremely wide distribution (Holzner et al., 2015) and can deviate substantially from the mean velocity and consequently, the ratio of mean shear stress values exerted on the biofilm by the $BaSO_4$ or the growth medium can be much higher than the factor of 3 obtained here. In such a case, the rheological properties of the $BaSO_4$ should not be neglected as they could substantially contribute to the biofilm detachment.

4.4 Biofilm detachment upon injection of the $BaSO_4$ suspension

Fig. 4.6 shows an image of the biofilm tubular reactor before the $BaSO_4$ injection A) and during the injection B) and C). The biofilm shows a reddish color typical of biofilms with high iron oxides content. B) and C) show the heterogeneous distribution of the BaS_4 concentration along the column shortly after starting the injection, as some pores are saturated and others not, due to mixing and dispersion. During the injection, we visually observed biofilm detachment and patches moving through the column. The black arrow in Fig. 4.6 shows a biofilm patch that at early times was free of BaSO4 but at later times it was not, which suggests sloughing or BaSO4 penetration into the biofilm between the acquisition of the images B) and C).

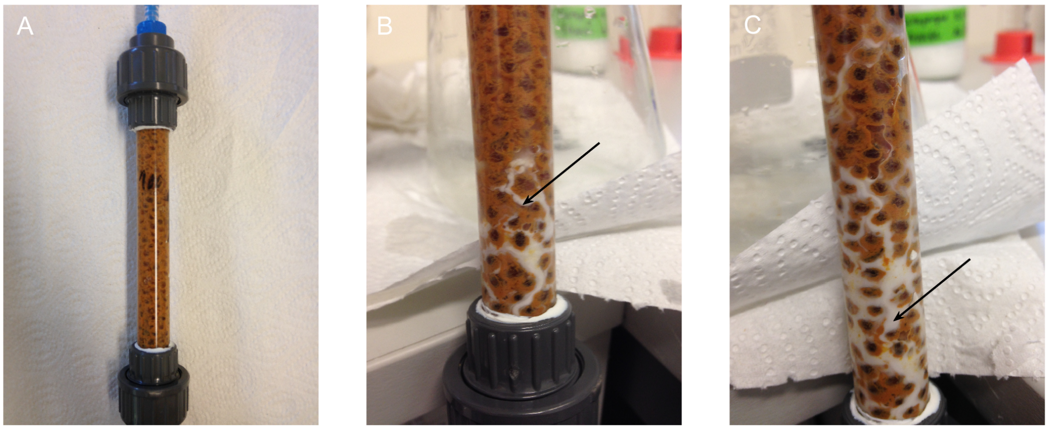

Figure 4.6: A) Biofilm tubular reactor used in this study. B) and C) images of the biofilm during the injection. The arrow is showing a biofilm patch beeing detached.

4.5 Theoretical derivation of the Lorentzian filter from first principles

This appendix briefly reviews the theory phase retrieval (Paganin *et al.* Paganin et al. (2002) method) in the context of propagation-based phase contrast imaging (PBI). It was put to together with the aim of: (i) Assisting readers who are non-experts in the field of coherent X-ray imaging with a brief summary therefore avoiding extensive literature review; (ii) Re-derive Paganin *et al.* Paganin et al. (2002) single-image phase-retrieval method and demonstrate that one can arrive at the same form by including polychromatic effect from first principles and; (iii) Show how the method can adapted and utilized as an image processing tool as a “Lorentzian Fourier filter".

We begin by stating the Transport-of-Intensity equation (TIE) Teague (1983). The TIE

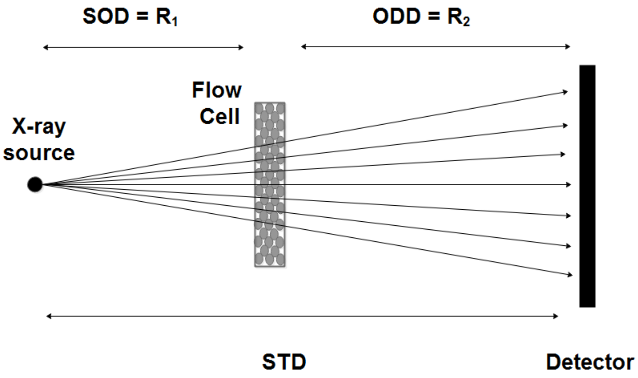

Figure 4.7: Schematic of the configuration used for the X-ray scans where the distances SOD , ODD and STD represent the source-to-object (SOD), object-to-detector and the source-to-detector distance (STD), adapted from Paganin et al. (2002).

is often used as starting point for paraxially-propagating monochromatic beams, which we will later generalize by accounting for polychomaticity. It is a second order elliptic partial differential equation that describes the local conservation of optical energy as wavefields evolve from one plane $z = \mathrm{R}_1$ to another infinitesimally separated parallel plane $z = \mathrm{R}_2$. It has the structure of a continuity equation and can be viewed as such. The form is given by

$$\nabla_\perp \cdot \left[\mathrm{I}(\mathbf{r}_\perp, E, \mathrm{R}_1)\nabla_\perp \phi(\mathbf{r}_\perp, E, \mathrm{R}_1)\right] = -k\frac{\partial}{\partial z}\mathrm{I}(\mathbf{r}_\perp, E, z) \tag{4.7}$$

Here, $\mathrm{I}(\mathbf{r}_\perp, E, \mathrm{R}_1)$ (with the aid of Fig. 4.7 is the wavefield's intensity at the plane exiting the sample $z = \mathrm{R}_1$ and $\phi(\mathbf{r}_\perp, E, \mathrm{R}_1)$ is the wavefield's phase at that same plane. The cartesian coordinates $\mathbf{r}_\perp = (x, y)$ are used to describe the field plane transverse to the optic axis z. $E = hc/\lambda$ is the photon energy of the beam which has been kept arbirary for the moment. $k = 2\pi/\lambda$ is the wavenumber and the term $\frac{\partial}{\partial z}\mathrm{I}(\mathbf{r}_\perp, E, z)$ represents the first order derivative of the intensity along the propagation axis z (see Fig 4.7).

For normally incident plane-wave illumination of an optically thin homogeneous object, the intensity and phase at the contact plane $z = \mathrm{R}_1$ is given by:

$$\mathrm{I}(\mathbf{r}_\perp, E, \mathrm{R}_1) = \mathrm{I}_0 \exp[-\mu(E)\mathrm{T}(\mathbf{r}_\perp)] \tag{4.8}$$

and

$$\phi(\mathbf{r}_\perp, E, \mathrm{R}_1) = -k\delta(E)\mathrm{T}(\mathbf{r}_\perp) \tag{4.9}$$

where, $\mu(E) = 2k\beta(E)$ is the linear attenuation coefficient and $\delta(E)$ is the decrement from unity of the of complex refractive index $n(E) = 1 - \delta(E) + i\beta(E)$ (Als-Nielsen and Des, 2011). We emphasize that both quantities are dependent on the Energy E of the incident X-radiation. $\mathrm{T}(\mathbf{r}_\perp)$ is projected thickness function of the object. I_0 is the incident intensity of the incoming beam. Substituting Eqs. 4.8 and 4.9 into Eqn. 4.7 then the left-hand-side of the resulting expressions appears as:

$$\frac{-k\mathrm{I}_0\delta(E)}{\mu(E)}\nabla_\perp^2 \exp[-\mu(E)\mathrm{T}(\mathbf{r}_\perp)] \tag{4.10}$$

Now, the right-hand-side of Eqn. 4.7 can be approximated as the difference of two-closely spaced intensity images, namely $\mathrm{I}(\mathbf{r}_\perp, E, \mathrm{R}_2)$ and $\mathrm{I}(\mathbf{r}_\perp, E, \mathrm{R}_1)$ separated by the object-to-detector distance (ODD) R_2 as depicted in Fig 4.7. That is,

$$\frac{\partial}{\partial z}\mathrm{I}(\mathbf{r}_\perp, E, z) \approx \frac{\mathrm{I}(\mathbf{r}_\perp, E, \mathrm{R}_2) - \mathrm{I}(\mathbf{r}_\perp, E, \mathrm{R}_1)}{\mathrm{R}_2} \tag{4.11}$$

Substituting Eqn. 4.8 into Eqn. 4.11 then equating to Eqn. 4.10 the intensity at the detector plane ($z = \mathrm{R}_2$) for an arbitrary E is given by:

$$\mathrm{I}(\mathbf{r}_\perp, E, \mathrm{R}_2) = \mathrm{I}_0\left[1 - \frac{\mathrm{R}_2\delta(E)}{\mu(E)}\nabla_\perp^2\right]\exp[-\mu(E)\mathrm{T}(\mathbf{r}_\perp)] \tag{4.12}$$

One can make further simplifications by Taylor expanding the exponential term up to first order in $\mathrm{T}(\mathbf{r}_\perp)$ giving:

$$\mathrm{I}(\mathbf{r}_\perp, E, \mathrm{R}_2) \approx \mathrm{I}_0 + \mathrm{I}_0\left[\mathrm{R}_2\delta(E) - \mu(E)\nabla_\perp^2\right]\mathrm{T}(\mathbf{r}_\perp) \tag{4.13}$$

The differential equation has now become linear in $\mathrm{T}(\mathbf{r}_\perp)$ and is considerably simpler. Therefore, at this point it proves convenient to further generalize by taking accounting for polychromatic radiation. This is done by integrating the intensity $\mathrm{I}(\mathbf{r}_\perp, E, \mathrm{R}_2)$ at the detector plane over all possible incoming X-ray energies of the source spectrum. All energy spectrums of radiation sources, whether they are synchrotron, X-ray tubes, or free-electron lasers have an associated spectrum distribution function $h(E)$. This implies that every photon E has an associated statistical number of counts h Als-Nielsen and Des (2011). Therefore, the intensity at the detector plane accounting for polychromatic radiation is given by the following integration:

$$\mathrm{I}^{\mathrm{Poly}}(\mathbf{r}_\perp, \mathrm{R}_2) = \frac{\int_{E_{min}}^{E_{max}} \mathrm{I}(\mathbf{r}_\perp, E, \mathrm{R}_2)h(E)dE}{\int_{E_{min}}^{E_{max}} h(E)dE} \tag{4.14}$$

Here, we have $E = E_{min}$ which is the lower bound corresponding to the lowest photon energy and E_{max} which is the upper bound corresponding to the highest photon energy.

Notice that the expression has been normalized by the total number of counts which is a non-negative real valued constant $\bar{\gamma} > 0$, that is:

$$\int_{E_{min}}^{E_{max}} h(E)dE = \bar{\gamma} \tag{4.15}$$

Upon substitution of Eqn. (4.13) of into Eqn. (4.14) the integral involving the differential element dE only acts on $\delta(E)$ and $\mu(E)$ thus enabling these integrals to be separated. Hence, the expression for the intensity at $z = \mathrm{R}_2$ under polychromatic incident illumination still remains linear

$$\mathrm{I}^{\mathrm{Poly}}(\mathbf{r}_\perp, \mathrm{R}_2) = \mathrm{I}_0 + \mathrm{I}_0 \left[\mathrm{R}_2\bar{\delta}_M - \bar{\mu}_M \nabla_\perp^2\right] \mathrm{T}(\mathbf{r}_\perp) \tag{4.16}$$

Here, it is important to make note that now that $\delta(E)$ and $\mu(E)$ have now become $\bar{\delta}_M$ and $\bar{\mu}_M$ as a result of separating the integrals which contain the variable E. In essence, these introduced terms are the weighted averages of $\delta(E)$ and $\mu(E)$ over the range of energies of the source spectrum of the beam. Also, like in Eqn. (4.15) these “weighted average" integrals give non-negative real valued constants as defines below:

$$\begin{aligned} \bar{\delta}_M &= \frac{\int_{E_{min}}^{E_{max}} \delta(E)h(E)dE}{\int_{E_{min}}^{E_{max}} h(E)dE} \\ \bar{\mu}_M &= \frac{\int_{E_{min}}^{E_{max}} \mu(E)h(E)dE}{\int_{E_{min}}^{E_{max}} h(E)dE} \end{aligned} \tag{4.17}$$

As a result one can now solve for $\mathrm{T}(\mathbf{r}_\perp)$ by Fourier transforming both sides of Eqn. (4.16) then making use of the Fourier derivative theorem to give

$$\mathrm{T}(\mathbf{r}_\perp) = \mathrm{F}^{-1}\left[\frac{1}{\mathrm{R}_2\bar{\delta}_M \mathbf{k}_\perp^2 + \bar{\mu}_M} \mathrm{F}\left\{1 - \frac{\mathrm{I}^{\mathrm{Poly}}(\mathbf{r}_\perp, \mathrm{R}_2)}{\mathrm{I}_0}\right\}\right] \tag{4.18}$$

where, F are F^{-1} are forward and inverse Fourier transforms, respectively. $\mathbf{k}_\perp = (k_x, k_y)$ are the transverse Fourier conjugate coordinates dual to $\mathbf{r}_\perp = (x, y)$. The following Fourier transform convention have been used:

$$\begin{aligned} G(\mathbf{k}_\perp) &= \int g(\mathbf{r}_\perp)\exp(-2\pi i \mathbf{k}_\perp \cdot \mathbf{r}_\perp) d\mathbf{r}_\perp \\ g(\mathbf{r}_\perp) &= \int G(\mathbf{k}_\perp)\exp(2\pi i \mathbf{k}_\perp \cdot \mathbf{r}_\perp) d\mathbf{k}_\perp \end{aligned} \tag{4.19}$$

where, $G(\mathbf{k}_\perp) = \mathrm{F}\left\{g(\mathbf{r}_\perp)\right\}$. From here additional manipulations can be made to prove that one can arrive at exact form of Paganin *el al.* Paganin et al. (2002) original single-image phase-retrieval algorithm however this time including polychromatic effects. The left hand side of Eqn. (4.18) can be separated into two terms:

$$\mathrm{T}(\mathbf{r}_\perp) = \mathrm{F}^{-1}\left[\frac{1}{\mathrm{R}_2\bar{\delta}_M\mathbf{k}_\perp^2 + \bar{\mu}_M} \times \widehat{\delta}(\mathbf{k}_\perp)\right] - \mathrm{F}^{-1}\left[\frac{1}{\mathrm{R}_2\bar{\delta}_M\mathbf{k}_\perp^2 + \bar{\mu}_M}\mathrm{F}\left\{\frac{\mathrm{I}^{\mathrm{Poly}}(\mathbf{r}_\perp, \mathrm{R}_2)}{\mathrm{I}_0}\right\}\right] \tag{4.20}$$

where, $\widehat{\delta}(\mathbf{k}_\perp) = \mathrm{F}\left\{1\right\}$ is the Dirac delta. Using the Dirac delta sifting theorem the 1st term on the right hand side reduces to:

$$\begin{aligned}\mathrm{F}^{-1}\left[\frac{1}{\mathrm{R}_2\bar{\delta}_M\mathbf{k}_\perp^2 + \bar{\mu}_M} \times \widehat{\delta}(\mathbf{k}_\perp)\right] &= \int \frac{\exp(2\pi i\mathbf{k}_\perp \cdot \mathbf{r}_\perp)}{\mathrm{R}_2\bar{\delta}_M\mathbf{k}_\perp^2 + \bar{\mu}_M}\widehat{\delta}(\mathbf{k}_\perp)d\mathbf{k}_\perp \\ &= \frac{1}{\bar{\mu}_M} \end{aligned} \tag{4.21}$$

This makes Eqn. 4.20 become:

$$1 - \bar{\mu}_M\mathrm{T}(\mathbf{r}_\perp) = \mathrm{F}^{-1}\left[\frac{\bar{\mu}_M}{\mathrm{R}_2\bar{\delta}_M\mathbf{k}_\perp^2 + \bar{\mu}_M}\mathrm{F}\left\{\frac{\mathrm{I}^{\mathrm{Poly}}(\mathbf{r}_\perp, \mathrm{R}_2)}{\mathrm{I}_0}\right\}\right] \tag{4.22}$$

We recall the first order Taylor expansion Taylor expansion approximation of an exponential function.

$$1 - \bar{\mu}_M\mathrm{T}(\mathbf{r}_\perp) \approx \exp\left[-\bar{\mu}_M\mathrm{T}(\mathbf{r}_\perp)\right] \tag{4.23}$$

Making use of this approximation in “reverse" is the final step which leads to the proof that Paganin *et al.* Paganin et al. (2002) original form can be obtained and can also be applied to PBI images acquired with polychromatic radiation sources such as the one used to collect the data for this study. The original form being

$$\mathrm{T}(\mathbf{r}_\perp) = -\frac{1}{\bar{\mu}_M}\ln\left[\mathrm{F}^{-1}\frac{1}{\frac{\mathrm{R}_2\bar{\delta}_M}{\bar{\mu}_M}\mathbf{k}_\perp^2 + 1}\mathrm{F}\left\{\frac{\mathrm{I}^{\mathrm{Poly}}(\mathbf{r}_\perp, \mathrm{R}_2)}{\mathrm{I}_0}\right\}\right] \tag{4.24}$$

As intuitively predicted, this derivation reveals that all that is required to implement the method in the context of polychromaticity is to replace the values of δ and μ with $\bar{\delta}_M$ and $\bar{\mu}_M$.

The algorithm is a simple convolution of the normalized intensity image with the Fourier filter $\frac{1}{\alpha\mathbf{k}_\perp^2+1}$, where the value $\alpha = \frac{\mathrm{R}_2\bar{\delta}_M}{\bar{\mu}_M}$ is known *a priori* and is the reason why the the method is stable under presence of noise. It is this feature which makes the algorithm practically advantageous even as image processing tool, which we do in this study by treating the collected PBI images as “unfiltered" radiographs (i.e. $\mathrm{I}^{\mathrm{Rad}} = \frac{\mathrm{I}^{\mathrm{Poly}}(\mathbf{r}_{\perp},\mathrm{R}_2)}{\mathrm{I}_0}$) and the retrieved images as “filtered" radiographs (i.e. $\mathrm{I}^{\mathrm{Filt}} = \exp\left[-\bar{\mu}_M \mathrm{T}(\mathbf{r}_{\perp})\right]$) as stated in Eqn (1) in the main manuscript.

Bibliography

Als-Nielsen, J. and Des, M. (2011). *Elements of Modern X-ray Physics.* John Wiley and Sons, Inc. pages

Holzner, M., Morales, V. L., Willmann, M., and Dentz, M. (2015). Intermittent lagrangian velocities and accelerations in three-dimensional porous medium flow. *Physical Review E*, 92(1):013015. pages

Irgens, F. (2014). *Rheology and Non-Newtonian fluids*, page 190. Springer International Publishing. pages

Paganin, D., Mayo, S. C., Gureyev, T. E., Miller, P. R., and Wilkins, S. W. (2002). Simultaneous phase and amplitude extraction from a single defocused image of a homogeneous object. *Journal of Microscopy*, 206(1):33–40. pages

Plouraboué, F., Cloetens, P., Fonta, C., Steyer, A., Lauwers, F., and Marc-Vergnes, J. P. (2004). X-ray high-resolution vascular network imaging. *Journal of Microscopy*, 215(2):139–148. pages

Teague, M. R. (1983). Deterministic phase retrieval: a green's function solution. *Journal of the Optical Society of America*, 73(11):1434–1441. pages

Chapter 5

Biofilms in 3D porous media: delineating the influence of the pore network geometry, flow and mass transport on biofilm development

This chapter consists of a manuscript submitted to: Water Research

M. Carrel[a,b,c,d], V. Morales[a,b,e], M. Beltran[a,b], N. Derlon[a,e], E. Morgenroth[a,e] , R. Kaufmann[a,e] and M. Holzner[a,c,e]. Biofilms in 3D porous media: delineating the influence of the pore network topology, flow and mass transport on biofilm development. Submitted to *Water Research*

[a] Study concept and design; [b] Data acquisition and analysis; [c] Interpretation of data; [d] Drafting manuscript; [e] Critical revision

Abstract: This study investigates the response between pore-scale hydrodynamics, mass transfer, pore structure and biofilm morphology during progressive biofilm colonization of a porous medium. Hydrodynamics and structural information are experimentally measured with 3D particle tracking velocimetry and X-ray Computed Tomography, respectively. Registration of the data sets allows to delineate the interplay between porous medium geometry, hydrodynamic and mass transfer processes on the architecture of the developing biofilm. A local analysis revealed wide distributions of wall shear stresses and concentration boundary layer thicknesses. The spatial distribution of the biofilm patches

revealed that the wall shear stresses controlled the biofilm adhesion, development and biofilm thickness. Neither external nor internal mass transfer limitations were noticeable in the considered system, consistent with the excess supply of nutrient and electron acceptors. The wall shear stress remained fairly constant in the vicinity of the biofilm but increased substantially elsewhere. This points at the complex feedback of a developing biofilm on the pore-scale hydrodynamics.

5.1 Introduction

Biofilms are communities of bacteria attaching and developing on surfaces and embedded in a matrix of extracelluar polymeric substances (EPS) and persistently developing in environmental, medical and industrial settings (Hall-Stoodley et al., 2004).

For all these different applications, biofilm growth can have a positive or detrimental impact. Therefore an understanding of the development of these bacterial communities in respect to the local geometry of the pore network, the pore-scale hydrodynamics and mass transport processes is a prerequisite for optimal biofilm control. The investigation of these processes requires access to wall shear stresses and concentration boundary layer distributions (Stoodley et al., 1998; Picioreanu et al., 2000).

The development of biofilms in porous media is a process involving a wide range of scales, from micro- over meso- to macroscale (Battin et al., 2007). For instance, microscale hydrodynamics were shown to control the initial attachment of individual bacteria to surfaces (Rusconi et al., 2014). The macroscale is the scale relevant for the integrated understanding of larger engineering or natural systems (reactors, aquifers). The mesoscale links the micro- and the macroscale, as it is the scale at which flow and mass transport interact with and define the biofilm structures (Eberl et al., 2000). The focus of this study is the mesoscale in porous media or pore-scale. Growth of biofilms in this context is interesting due to the complexity of the geometry of pore networks, yielding pore-scale velocities and length scales (i.e. pore radii) ranging over orders of magnitude. Porous media can be considered as networks of connected three-dimensional roughness elements or corners representative of e.g. soils or filters but also of many other microscale environments in which biofilms develop in natural or industrial settings.

Biofilm development in these structures was revealed to result in highly diverse and complex phenomena by previous studies. For instance, the growth of biofilms was identified to induce the formation of preferential flow paths and the interplay between biofilm growth, detachment, decay and lysis was numerically shown to cause the intermittent shifting of these flow paths Bottero et al. (2013). Locally, the intricate geometry of the pore network and the evolving flow field during biofilm growth influence competition between bacterial communities, as slow growing or non EPS-producing bacteria can outcompete fast growing or EPS-producing ones (Coyte et al., 2017; Nadell et al., 2017). Most previous studies on biofilm growth at the pore-scale considered mainly porous media with two-dimensional pore-networks either experimentally (Drescher et al., 2013; Qian et al., 2017) or numerically (Kapellos et al., 2007). The dynamics of biofilm development were shown to be substantially different for 2D or fully 3D porous media (von der Schulenburg et al.,

2009) and up to now, there still remains a lack of both experimental pore-scale flow and structural information about biofilm development in 3D porous media.

Experimental data on pore-scale biofilm properties and hydrodynamics is also important to validate or refine existing biofilm models. For instance many 1D biofilm models used to quantify reaction rates in biofilm reactors (trickling filters, moving bed biofilm reactors etc.) require information regarding the average biofilm thickness or specific surface area (Boltz et al., 2010). 2D and 3D continuum models rely on another relevant parameter, which is the biofilm shear strength, i.e. the resistance of biofilms to shear exerted by the surrounding fluid (von der Schulenburg et al., 2009; Bottero et al., 2013). Biofilm shear strengths values used in these models are often taken from the literature, thus calling for on-site measurements in 3D porous media. This is reinforced by the wide distributions of shear strengths mentioned in recent studies (e.g. Stewart (2014)), which can be attributed to the natural heterogeneous distribution of material properties of biofilms (Stewart and Franklin, 2008), but also to the distribution of wall shear stresses exerted by fluid flow on biofilms as a consequence of velocity gradients in the biofilm vicinity (Stewart, 2014). Additionally, very often the wall shear stresses exerted on the biofilm are roughly approximated based on the initial hydrodynamic conditions (Derlon et al., 2008; Blauert et al., 2015), thus not accounting for the feedback of the biofilm on the flow, which increases the uncertainty of the assumed biofilm shear strength.

The goal of this paper is to experimentally investigate the influence of pore-scale variables relative to hydrodynamic and mass transfer processes (e.g. wall shear stress and concentration boundary layer distributions) on biofilm development in 3D porous media. A biofilm is grown in a 3D porous medium for 36 hours under a constant flow rate and with nutrients and electron acceptors supplied in excess. The hydrodynamics are measured at the pore-scale with three-dimensional particle tracking velocimetry (3D-PTV) in a clean porous medium and after biofilm growth. The structure of the porous medium and the morphology and spatial distribution of the biofilm are obtained with X-ray micro Computed Tomography (X-ray μCT) after biofilm growth. This allowed to capture the wide distributions of length scales, pore-scale velocities, wall shear stresses and concentration boundary layer thicknesses and unraveled the different contributions of these to the morphology of the nascent biofilm. Underlying research questions are:

- In a porous medium with a wide range of pore radii, which are the pores preferentially colonized by the growing biofilm?
- How does the growth of the biofilm depend on the local wall shear stress and local mass transfer processes?
- Does the expected wide ranges of wall shear stresses occurring in porous media allow to define a maximal biofilm shear strength? If it does, this new approach would provide an indirect, non-invasive method to estimate shear strength that constitutes an alternative with respect to invasive methods such as tensile strength tests (Möhle et al., 2007).
- What is the influence of the growing biofilm on the pore-scale hydrodynamics?

5.2 Material and Methods

5.2.1 Porous Medium

The porous medium used in this work consists of nafion pellets (Ion Power, Munich, Germany), a material with physico-chemical properties similar to that of sand grains (Downie et al., 2012). The diameter d_N of the pellets is roughly monodisperse and distributed around 2.5 mm. Nafion is a polymer whose optical refractive index can easily be matched (RIM) with aqueous solutions yielding models of transparent soil (Downie et al., 2012). Here, a decent RIM was obtained with a glucose concentration of 11 % w/v. The nafion pellets underwent three time the following treatment allowing to enhance transparency. Ca. 20 g. of pellets were first heated up at 65°C for 1 h while stirred at 200 rpm under a reflux cooler and then were cooled for 30 min at room temperature and stored overnight at 4°C.

5.2.2 Biofilm Culturing

The 11% w/v glucose solution used as a growth medium in this study was prepared with tap water. In order to enhance bacterial growth, nitrogen and phosphorus were added to a molar ratio C:N:P of 1000:1:1. This low ratio is due to the high glucose concentration that was not only serving as a carbon source but also provided the refractive index matching with the nafion grains. Nitrogen was added under the form of $NaNO_3$. Nitrate was here serving both as nitrogen source and electron acceptor. Phosphorus was added as K_2HPO_4 and $NaH_2PO_4 \cdot 2(H_2O)$ accounting for 1/3 resp. 2/3 of the total phosphorus molecular ratio, yielding inflow concentrations of 8.14 mg NO_3-N/L and 18.9 mg PO_4-P/L.

The mixed species bacterial inoculum used in this study was isolated from river water samples. The frozen bacterial inoculum contained in 2 mL Eppendorf tubes was added to 100 mL of the growth medium incubated for 20-24 h at 30°C and stirred at 200 rpm until reaching midlogarithmic phase (OD_{600} 0.52 ± 0.096). The incubation procedure was repeated three times for the bacteria to adapt to the synthetic carbon source of the growth medium. For the last incubation cycle, the nafion grains were added to the growth medium to allow initial bacterial attachment. Upon the incubation, a custom built PMMA flow-cell (38 x 38 x 16 mm^3) was wet packed with the nafion grains. 10 L growth medium bottles were connected to the flow cell with silicon tubing (VWR, Dietikon, Switzerland) previously washed with 70% ethanol and thoroughly rinsed with DI water. The 10 L growth medium bottles were replaced every 12 h and were spiked with 100 mL of the inoculum. A peristaltic pump (Ismatec, Glattbrugg, Switzerland) was used to set a volumetric flow rate of 10 mL/min that was kept constant over the course of the experiment. As illustrated in Figure 5.1 (a), a syringe was used as a bubble trap as well as to dampen the pulsatile flow created by the peristaltic pump. Nitrate and oxygen concentration were sampled in the effluent every 12 hours and revealed a high bacterial activity but no actual nutrient limitations (4.41 ± 0.67 mg NO_3-N/L and 4.84 ± 0.55 mg O_2/L respectively).

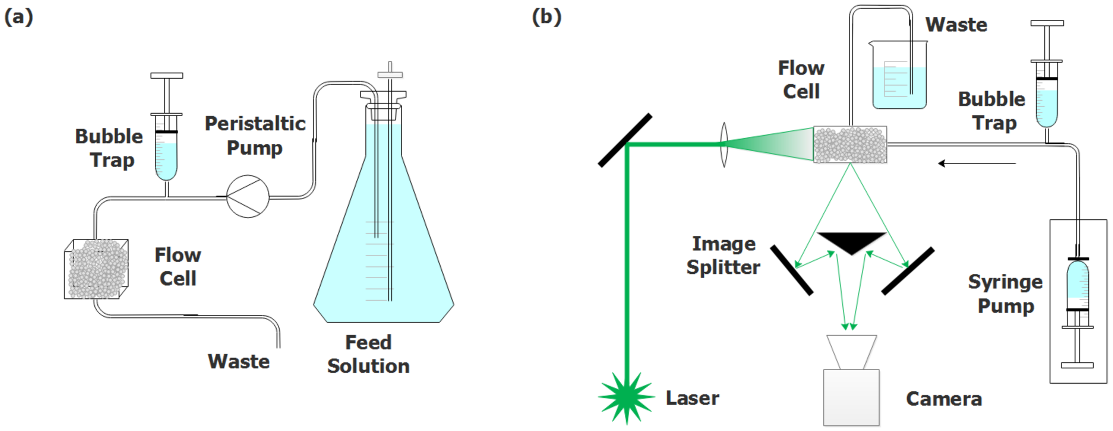

Figure 5.1: Schematic illustration of the experimental set up used for biofilm culturing in (a) and for the 3D-PTV measurements in (b).

5.2.3 Three-Dimensional Particle Tracking Velocimetry

The three-dimensional particle tracking velocimetry (3D-PTV) method applied in this work allows to detect and track particle tracers, thereby providing among others, the position, velocity and acceleration of the tracers along trajectories. This method was developed to study turbulent flows (Hoyer et al., 2005) but was lately adapted to study flows in porous media (Holzner et al., 2015). In order to perform the 3D-PTV measurements, the flow cell was connected to a 120 mL syringe mounted on a syringe pump (Lambda Vit-Fit, Lambda, Baar, Switzerland). The volumetric flow rate was set to 10 mL/min, yielding a Darcy velocity q of 0.27 mm/s and an average interstitial pore velocity v_P of 1 mm/s. The corresponding Reynolds number was then with $Re = v_P d_N / \nu \cong 0.5$ still within the validity of Darcy's Law ($Re \leq 10$). Fluorescent Red Polyethylene Microspheres (Cospheric, Santa Barbara, CA USA) with a density of 1 g/cm^3 and with a diameter d_P of ca. 70 µm were added to the flow. As these particles are neutrally buoyant, inertial effects are not of concern and the particles follow the flow reliably (Holzner et al., 2015).

For each 3D-PTV run, the tracer particle concentration added is of 0.02 g/L, corresponding to a volume fraction of 0.002% low enough to ensure that particle-particle interactions were not of concern. The fluorescent tracer particles were illuminated with a 100 W pulsed Nd:YLF laser (Darwin Duo, Quantronix, Hamden, USA). Figure 5.1 (b) shows the setup used for the 3D-PTV experiments. The flow cell was imaged from both the front and back sides with a Photron Fastcam SA5 with a resolution of 1024x1024 at 50 fps using an image splitter providing 4 stereoscopic views. Between 30 and 200 particles were tracked per frame, yielding $\mathcal{O}(10^6)$ data points for every measurement (4549 and 4193 trajectories for the time points T = 0 and T = 36 h respectively) and trajectories of an accuracy of ca. 50 μm (Holzner et al., 2015). Finally, invoking the stationarity of the pore-scale flow and neglecting structural changes induced by biofilm growth over the time scale of the 3D-PTV experiments (ca. 30 min) we obtain an average inter-particle distance of 50 μm which sets the spatial resolution of the PTV data.

5.2.4 X-ray microtomography

Biofilms form porous structures (up to 90 % porosity) (Wagner et al., 2010) with high water content and densities very close to that of water. Thus, the application of X-ray microtomography to biofilm imaging requires the addition of contrast agents. Here, we follow the approach presented by Davit et al. (2011) and use a suspension of 0.05 g/mL particular barium sulfate ($BaSO_4$) particles (Micropaque, Guerbet, Zürich, Switzerland) as a contrast agent. Davit et al. (2011) noted biofilm detachment occurring during the $BaSO_4$ injection. Carrel et al. (2017) suggested to use iron sulfate ($FeSO_4$) as a contrast agent by continuously adding it to the biofilm during culturing and thus avoiding detachment. However, this approach could not be applied here without negatively affecting the RIM. Therefore, $BaSO_4$ was used as a contrast agent. In order to minimize biofilm-contrast agent interactions, the injection of the $BaSO_4$ was done overnight (12 h) at a volumetric flow rate 500 times smaller than the growth flow rate.

X-ray scans of the biofilm samples were performed at EMPA on a custom built scanner consisting of a tungsten microfocus source with cone-beam configuration and a 40 x 40 cm^2 flat panel detector. Four frames of 1441 projections were acquired over 3 hours at a voltage of 80 keV and focused electron beam current of 125 μA. Reconstruction was performed as presented in (Carrel et al., 2017). The resolution of the obtained tomograms was of ca. 27 μm. A first scan was imaged prior to the injection of the contrast agent, in order to obtain the initial porous media and a second was imaged after the injection of the contrast agent, in order to obtain the biofilm coated porous media.

The reconstructed tomograms exhibited beam-hardening artifacts which were attributed to the polychromatic nature of the X-rays, the high absorption coefficient of Barium and the non-homogeneous distribution of the contrast agent within it. These artifacts were mostly localized near the sides of the anisotropic flow cell while for the central region good quality could be obtained. Therefore, a central zone of the flow cell was segmented, where the artifacts were weaker (with dimensions of 20 x 20 x 16 mm, i.e. 25% of the total flow cell volume). A contrast enhancement step was effectuated using FIJI. A non-local mean filter was then run in Avizo. Segmentation was done using Avizo and consisted of watershed segmentation refined with morphological operations (closing of the solid grains and of the biofilm and opening of the air bubbles). The air bubbles that entered the flow cell during the injection of the contrast agent were assigned to the liquid phase. Biofilm patches smaller than 10 voxels were considered to be noise and dropped for the analyses presented hereinafter. Finally, the procedure presented in Pérez-Reche et al. (2012) was used to perform a network analysis extracting the pore radii along the skeleton of the void space.

5.2.5 Registration

The X-ray segmented data set and the 3D-PTV trajectories were registered (e.g. transformed into one coordinate system) in order to allow a local investigation of the biofilm -

flow coupling. The registration was performed using a custom registration algorithm. In a first step, the Lagrangian 3D-PTV flow information was mapped on a Eulerian grid of 81 μm size, corresponding to three times the resolution of the X-ray data. The resolution of the X-ray tomograms (27 μm) was decreased accordingly for the ease of calculation (binning based on voxel averages). Consecutively, a linear transformation was obtained by a discrete pseudo - digital volume correlation maximizing the following criterion:

$$r_{ijl} = \frac{\sum_m \sum_n \sum_o \left[\mathcal{V}_X(m+i, n+j, o+l)\right]\left[\mathcal{V}_P(m,n,o)\right]}{\sum_m \sum_n \sum_o \mathcal{V}_P(m,n,o)} \tag{5.1}$$

where i, j and l are the components of the displacement vector $\mathcal{D}(i,j,l)$, $\mathcal{V}_X$ is the segmented liquid phase of the volumetric X-ray data set and $\mathcal{V}_P$ is the amount of 3D-PTV Lagrangian data mapped on the Euleria grid. The final r_{ijl} obtained for the different data sets were of 88.67% for the clean porous media and of 76.78 % for the bioclogged packing, meaning that about 11.33% and 23.22% respectively of the 3D-PTV data was intersecting with the X-ray data. The uncertainty related to the registration can be inferred to partial volume effects due to the decreased resolution of the tomograms and to the accuracy of the 3D-PTV. Figure 5.2 (a-d) allows to visually assess the quality of the registration.

5.2.6 Calculation of local wall shear stress and concentration boundary layer thickness

The registered data provided the basis for a local analysis of hydrodynamic and mass transfer processes. A first variable of interest is the wall shear stress τ_w, defined as $\tau_w = \mu \left|\frac{\partial v}{\partial n}\right|_{n=0}$ where μ is the dynamic viscosity of the fluid and $\left|\frac{\partial v}{\partial n}\right|_{n=0}$ a velocity gradient defined by the velocity magnitude v and the vector n normal to the triangulated faces of the solid phase (nafion grains) or of the biofilm and evaluated at their surface. In order to evaluate this velocity gradient, the Lagrangian data was first binned on a Eulerian grid of 100 μm mesh size. As the interparticle distance of the 3D-PTV data was of ca. 50 μm on average, the Eulerian velocity field obtained after binning was not perfectly filled, i.e. there are empty voxels which were not sampled by any fluid particle.. The velocity gradients were then interpolated from the Eulerian velocity field on the normal of the solid surface (nafion grains or biofilm), providing access to the wall shear stress distribution. τ_w is approximated here assuming a no-slip boundary condition at the biofilm surface and thus, non-permeable biofilms. However, several authors showed that biofilms are permeable and have networks of submicroscopic channels (Davit et al., 2013). Since the permeability of biofilms is generally fairly low (Deng et al., 2013), we assume that its influence on the approximation of the wall shear stresses is negligible. Faces where not enough 3D-PTV data was available to perform the required interpolation of the velocity gradient at the grain or biofilm surfaces due to the presence of empty voxels were not considered.

A second variable of interest allowing to assess the influence of mass transfer conditions on biofilm development is the concentration boundary layer thickness δ_c. The mass transfer coefficient $k_s = D_s/\delta_c$ indicates the speed at which substrate or electron acceptors diffuse over the concentration boundary layer thickness δ_c from the bulk of the pore network towards the surface of the grain. Therefore, nutrient limitations are less prone to occur for small concentration boundary layer thicknesses. In order to estimate δ_c, we first consider that it is linked to the hydraulic boundary layer thickness δ_v as $\delta_c = \delta_v / Sc^{1/3}$, where the Schmidt number $Sc = \nu / D$ expresses the ratio of momentum diffusivity to mass diffusivity. The thicknesses δ_c and δ_v are commonly defined as lengths stretching normally from the substratum to the 99th percentile of fully developed concentration or velocity profiles respectively. Here, due to the intricate substratum geometries and velocity profiles, the hydraulic boundary layer thickness δ_v is approximated by considering the length scale associated with molecular diffusion of momentum as induced by shear as $\delta_v = \sqrt{\nu / \frac{dv}{dn}}$. This means that the concentration boundary layer thickness δ_c is proportional to ${\tau_w}^{-1/2}$.

5.3 Results

5.3.1 Registered Data

Figure 5.2 presents the results of the registered 3D-PTV and X-ray data for the central region of the flow cell for the initial clean porous medium (T = 0 h) in (a) and after 36 h of biofilm culturing in (b). Figure 5.2 (c) and (d) are local close-ups of (a) and (b). The trajectories in Figure 5.2 are color-coded with the velocity magnitude, illustrating the intermittency of velocities along trajectories typical of porous media flows (de Anna et al., 2013). The increasingly darker coding of the velocities along trajectories reflects the average velocity increase according to mass conservation due to the porosity reduction and the constant flow kept. Additionally, biofilm growth induced substantial changes on the pore-scale flow field (compare Figure 5.2 (a) and (b)).

On Figure 5.2 (b) heterogeneous biofilm patches are distributed in between solid grains. Note that in (b), the flow information is not distributed homogeneously. This could either be caused by flow tracers not sampling stagnation zones or because the view of the particles was obstructed by biofilm patches. The close-ups (c) and (d) show local changes of the flow field upon biofilm growth. The biofilm patches illustrated in (d) exhibit a fairly high aspect ratio and an orientation approximately aligned with the initial flow direction. Upon biofilm growth, the channel on the left of the central grain presented in (d) appears to be shut down, indicating that the local obstruction caused by a the growth of a patch in a pore implies non-local hydrodynamic changes. Figure 5.2 (e) and (f) present triangulations of the patches presented in the close-ups and bounding boxes fitted to each individual patches. The bounding boxes allowed to extract geometric features of the patches such as their aspect ratio.

5.3.2 Influence of biofilm growth on pore scale statistics

In order to quantitatively describe the influence of biofilm growth on the pore-scale hydrodynamics, we conduct a statistical analysis on relevant variables in the clean and bioclogged porous medium for the central region considered. Figure 5.3 (a) presents the probability density functions (PDF) of the velocity magnitude for the clean and bioclogged porous

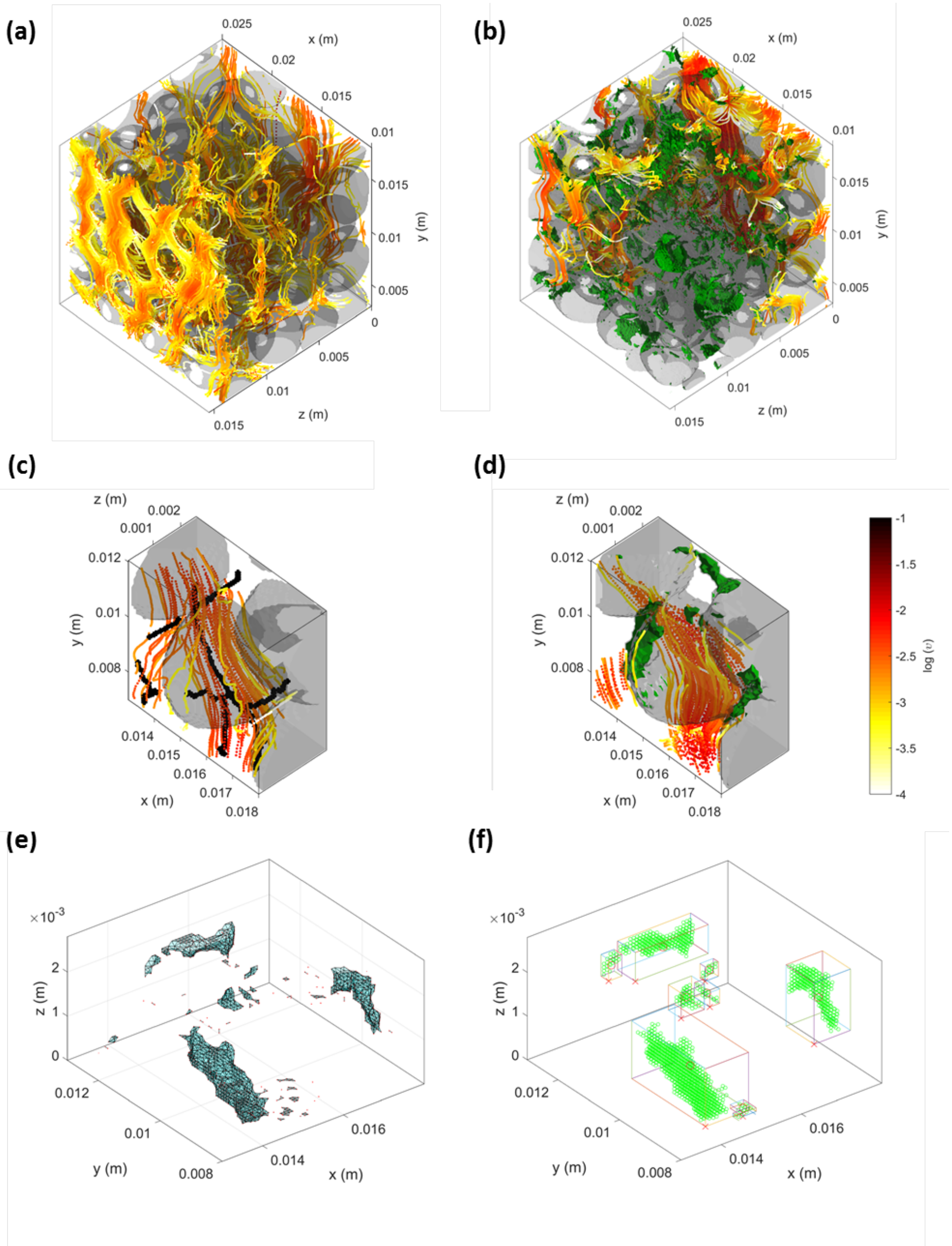
(a)
0.025
x (m)
0.02
0.015
0.01
0.015
0.01
y (m)
0.005
0
0.005
0.01
z (m)
0.015
(b)
0.025
x (m)
0.02
0.015
0.01
0.015
0.01
y (m)
0.005
0
0.005
0.01
z (m)
0.015
(c)
z (m)
0.002
0.001
0.012
0.01
y (m)
0.008
0.014
0.015
0.016
x (m)
0.017
0.018
(d)
z (m)
0.002
0.001
0.012
0.01
y (m)
0.008
0.014
0.015
0.016
x (m)
0.017
0.018
-1
-1.5
-2
-2.5
log (ε)
-3
-3.5
-4
(e)
×10^-3
2
z (m)
1
0
0.012
0.01
y (m)
0.008
0.014
0.016
x (m)
(f)
×10^-3
2
z (m)
1
0
0.012
0.01
y (m)
0.008
0.014
0.016
x (m)

Figure 5.2: (a) and (b) show the registered data 3D-PTV and X-ray of the central zone of the sample prior to biofilm culturing and after 36 hours of biofilm growth. The solid surfaces (nafion grains and biofilm) are here representing a color-coded (nafion grains in gray and biofilm in green) Delaunay triangulation of the segmented X-ray data. (c) and (d) show a local magnification of a pore before and after biofilm colonization. Note that the black points in (c) represent the skeleton along which the pore radii were computed. The colorbar in (d) shows the scale of the velocity magnitude color-coding used for (a)-(d). The skeletons are not shown in (a), (b) and (d) for the sake of clarity. (e) shows the biofilm patches illustrated in (d). (f) shows the same patches and bounding boxes from which the aspect ratio of the patches were computed. Note that the biofilm patches of sizes smaller than 10 voxels visible in (e) and removed in 5.2 (f).

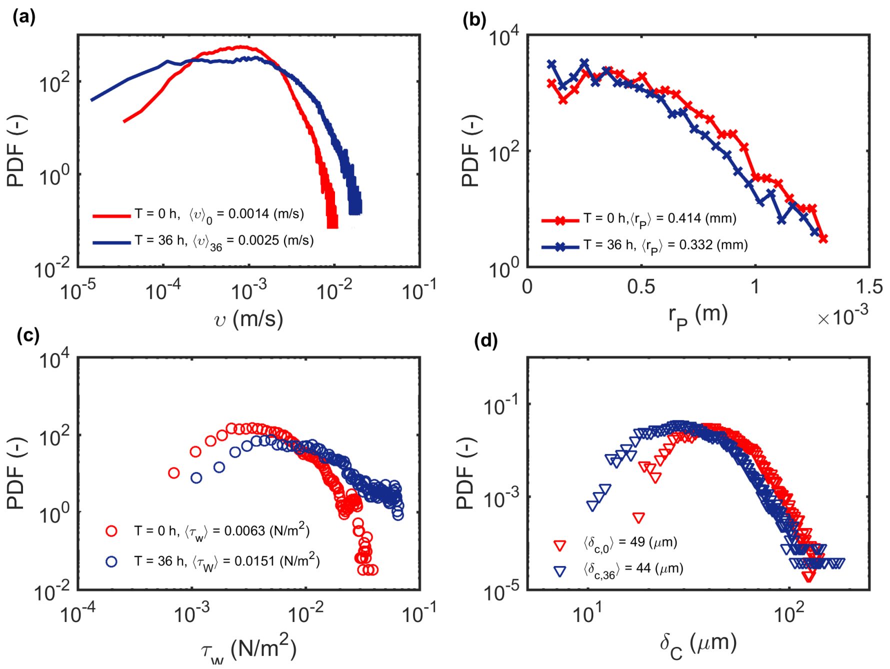

Figure 5.3: (a) shows probability density functions of the velocity magnitude for different time points during biofilm growth. The probability density functions of the pore radii are presented in (b) whereas (c) and (d) show the probability density functions of the measured wall shear stresses and of concentration boundary layer thicknesses for the clean and bioclogged porous media, respectively.

medium. Upon biofilm growth, there is a slight increase of the average velocity and a substantial increase of the high and low tailings of the PDF. These increased tailings are typical of flow fields for pore networks of increasing heterogeneity (Siena et al., 2014; Morales et al., 2017). This indicates that the growing biofilm affects the pore network and underpins the formation of preferential flow paths (increased high velocity tail) and slow velocity zones (increased low tail of the PDF). The impact of the biofilm on the pore network is further confirmed by Figure 5.3 (b) showing the pore radii distribution for the clean and bioclogged packings. With biofilm growth, the average pore radius decreases from 0.414 mm to 0.332 mm. Note that these distributions have an exponential tail typical of pore radii distribution in porous media (Holzner et al., 2015).

The wall shear stress distributions obtained are presented on Figure 5.3 (c) and stretch over more than two order of magnitudes. With biofilm growth, subsequent reduction of the pore space and average velocity increase due to mass conservation, the wall shear stresses obtained after biofilm growth increase substantially. Figure 5.3 (d) shows the distribution of the concentration boundary layer thicknesses δ_c for the clean and bioclogged porous media. As a consequence of the wall shear stress increase observed previously, the concentration boundary layer thickness decreases accordingly, meaning that on average, mass transfer

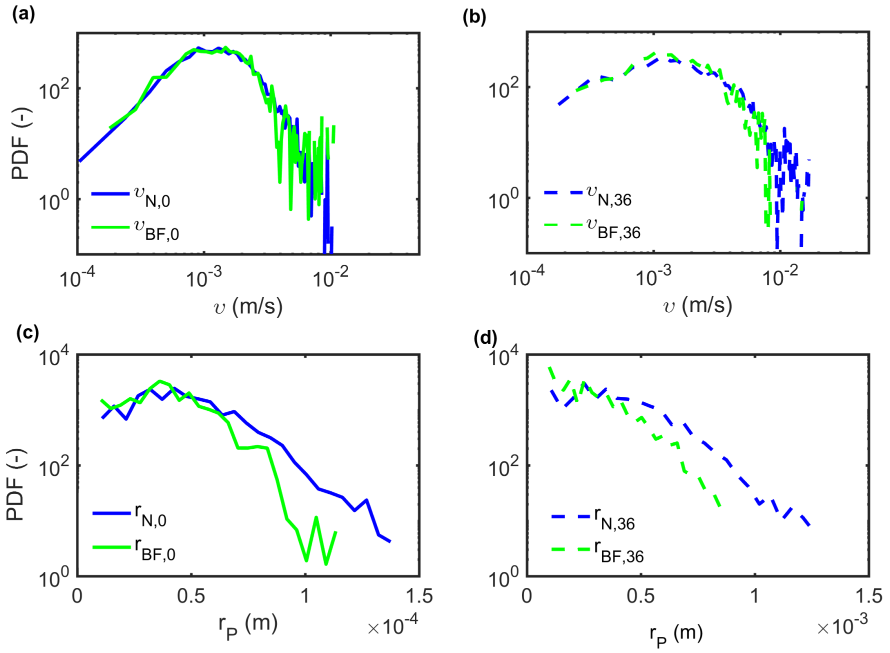

Figure 5.4: (a) and (b) show the PDFs of the pore-scale velocity magnitudes for the clean and bioclogged porous medium, whereas (c) and (d) show the corresponding pore radii PDFs. BF and N here indicates if the considered data is located in a one pore radius distance to the biofilm or nafion grains.

was increased during biofilm growth.

5.3.3 Local statistical analysis

When considering the distributions of variables describing the geometry of the pore network and the local hydrodynamics presented in Figure 5.3, it is interesting to investigate how these variables locally influence the biofilm or are themselves changed by the developing biofilm. Therefore, we distinguish between channels of the pore network in which biofilms are present within a distance of one pore radius. For the initial time point, this distinction is performed for nafion faces on which biofilm (BF) will develop or not (N). For the bioclogged data, the distinction is done depending on whether biofilm had developped (BF) on the channel or the nafion grains remained uncolonized (N).

Figure 5.4 (a) and (b) show the PDFs of the pore-scale velocity magnitude in the vicinity of the nascent and developed biofilm patches and in the remaining channels. The PDFs do not show any clear differences, indicating that the pore-scale velocity do not directly influence the biofilm development. Figure 5.4 (c) and (d) shows the same comparison for the pore radii. Here a noticeable difference emerges, as the pore radii where the biofilm initially develops are on average smaller than the remaining ones. Additionally, the pore radii in the biofilm vicinity after biofilm culturing show a substantial increase of very

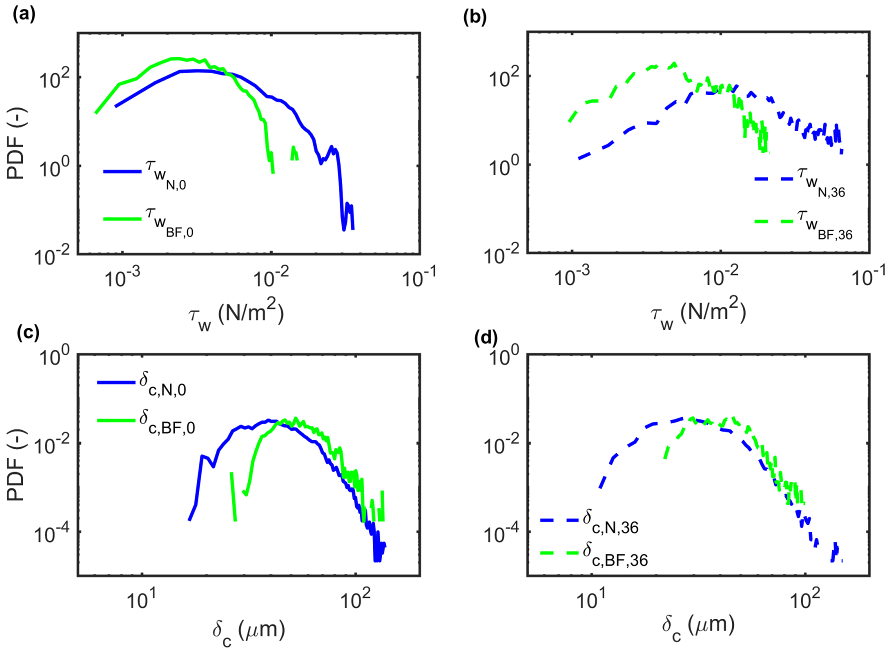

Figure 5.5: (a) and (b) shows the PDFs of wall shear stresses for the clean and bioclogged porous medium. (c) and (d) presents the corresponding concentration boundary layer thicknesses PDFs. BF and N here indicates if the considered data is located within a one pore radius distance to the biofilm or nafion grains.

small radii (see Figure 5.4 (d)), indicating an increase of small-scale pore geometry in the vicinity of the biofilm and therefore also, an increase of the biofilm specific surface area, a key parameter for the estimation of mass transfer within biofilms (Horn and Lackner, 2014).

The distributions of the wall shear stress values obtained for the faces of the clean nafion grains (solid) and for the faces at the base of the nascent biofilm are shown on Figure 5.5 (a) and (b). Interestingly, even if there is a fairly wide distribution in both cases, a clear difference between the two types of faces is noticeable. Thereby, the maximal wall shear stress for the faces that will not be colonized by the biofilm are about twice as large as the faces at the basis of the nascent biofilm. This difference remains after biofilm growth, as the distributions remain clearly different. Substantial differences are also observed for the concentration boundary layer thicknesses depicted in 5.5 (c) and (d). No biofilm seems to have colonized or developed in the regions of the smallest concentration boundary layers, which also corresponded to the high wall shear stress regions. This shows clearly that the wall shear stress controls biofilm development since smaller δ_c means faster mass transfer rates, which would favor biofilm growth.

5.3.4 Morphology of the biofilm patches

Figure 5.6 (a) shows the PDF of the biofilm patch size and (b) shows the distribution of biofilm patch sizes as a function of the average pore radii of the clean porous medium in which the patches grew over the course of the experiment. Interestingly, the biofilm patch sizes seem to follow a power law distribution. The biofilm patch size increases with the pore radii, which is expected since biofilm patches are confined by the radii. The largest biofilm patches are found for average radii of 0.47 mm, slightly over the average radius of the porous medium ($\langle r_P \rangle = 0.41$ mm). The largest radii appear to be associated with rather small biofilm patches. The wide distribution of the biofilm patch sizes indicates that there is no simple direct relation between the patch size and the pore radii. Figure 5.6 (c) shows the PDF of the biofilm patches aspect ratio and (d) shows the distribution of the biofilm patch sizes as a function of the aspect ratio. The aspect ratio are also widely distributed, with an average at 3.9. Figure 5.6 (d) shows that the maximal size of the biofilm patches decreases with increasing aspect ratio. The PDF of the biofilm thickness is presented in (e), where the biofilm thickness is defined as the distance between center of the biofilm faces to the center of the closest grain faces. The wide range of biofilm thicknesses observed reflects the patchiness of the biofilm morphologies visible in Figure 5.2 (e) and (f). Figure 5.6 shows the distribution of the biofilm thickness as a function of the initial wall shear stress. Interestingly, the maximal biofilm thickness measured decreases with increasing wall shear stresses.

5.3.5 Relation between pore-scale velocities and radii

Figure 5.7 shows joint PDFs of the normalized velocity and of the normalized pore radius. (Holzner et al., 2015) conjectured the dependence of the pore-scale velocity v on the pore radius r_P according to the power law:

$$v_m = v_0 (r_P / r_0)^{\alpha}, \qquad -2 \leqslant \alpha \leqslant 2 \tag{5.2}$$

where v_0 and r_0 represent characteristic velocities and pore radii. The exponent alpha is a parameter reflecting the pore network geometry and stretches from -2 for a completely serial pore arrangement to 2 for a completely parallel one. These power law scalings are indicated on Figure 5.7 (a) and (b) as a dotted-dashed and a dashed line respectively. The white circles show the conditional average of $v/\langle v \rangle$ on $r_P/\langle r_P \rangle$ and the continuous line shows a power law fitted to the conditional average, whose exponent is indicated on the top right corner of the respective figures. The width of the joint PDFs of $v/\langle v \rangle$ and $r_P/\langle r_P \rangle$ increases with biofilm growth but are found within the scalings corresponding to completely parallel or serial pore arrangements. The exponents measured decrease slightly from 0.257 to 0.063, reflecting the influence of the growing biofilm on the pore network.

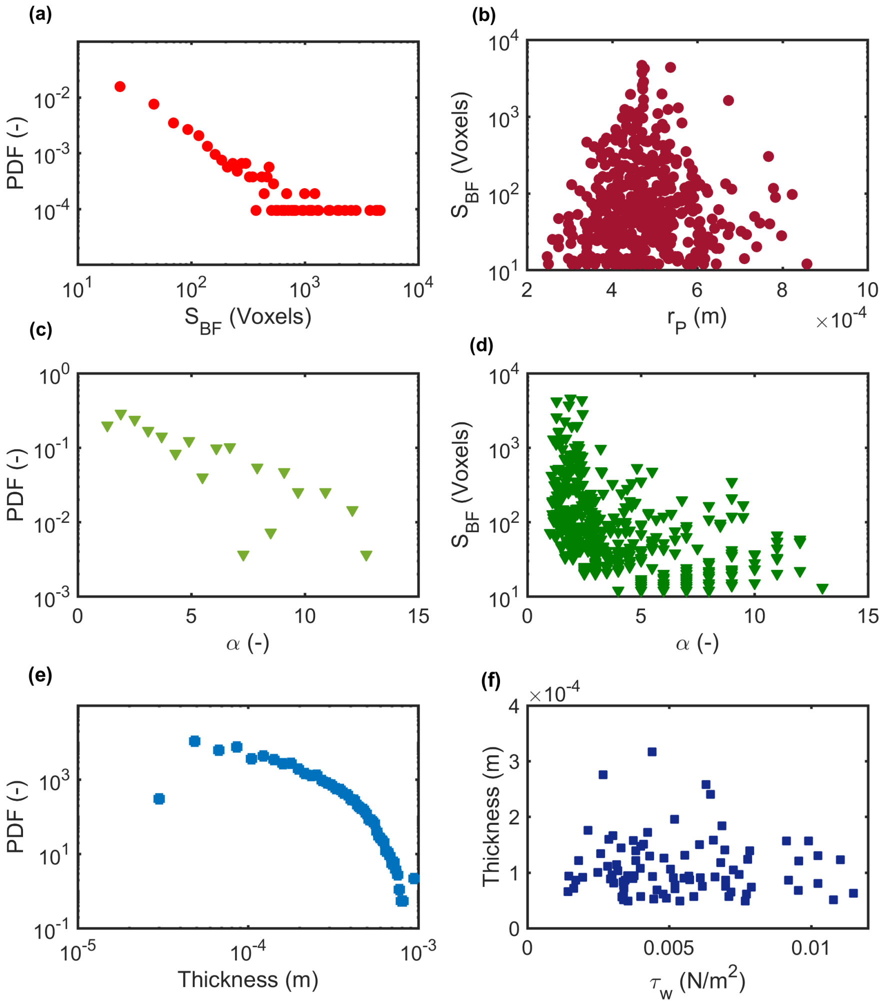

Figure 5.6: (a) shows the PDF of the biofilm patch sizes in the porous media and (b) the distribution of biofilm patch sizes as a function of the pore radius. (c) shows the distribution of aspect ratio and (d) the patch size distribution as a function of the aspect ratio. (e) shows the distribution of the biofilm thickness and (f) shows the biofilm thickness as a function of the wall shear stress.

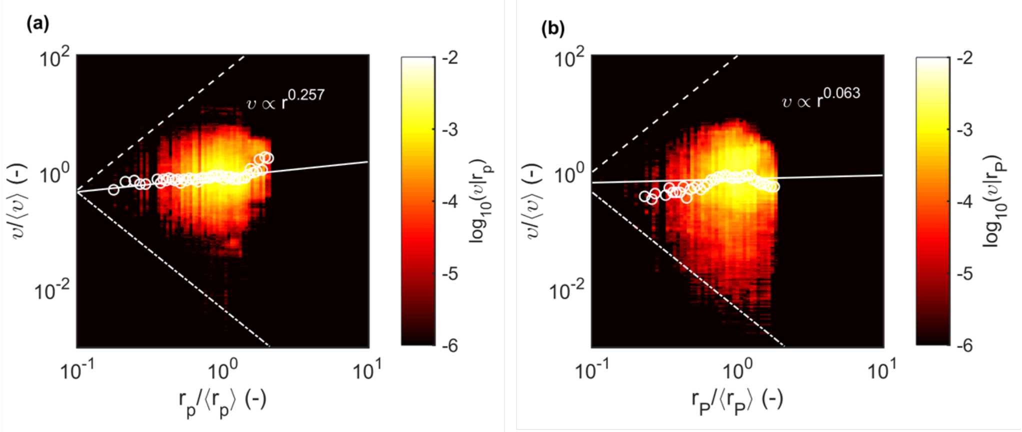

Figure 5.7: (a) and (b) show the joint PDFs of $v/\langle v\rangle$ and $r_P/\langle r_P\rangle$ for the clean and bioclogged porous media. The dashed and dashed-dotted lines show power laws with exponents of 2 and -2 respectively. The white circles are conditional averages of $v/\langle v\rangle$ on $r_P/\langle r_P\rangle$ and the continous line is a regression of the conditonal average. The exponents of the regression are indicated.

5.4 Discussion

5.4.1 Which variable does locally control biofilm development?

The overarching goal of this study is to provide experimental evidence allowing to delineate the influence of porous medium geometry, flow and mass transfer on the growth of biofilm in a 3D porous medium. The results obtained show that for geometries representative of many environments in which biofilms develop, biofilms are exposed to wide distributions of wall shear stresses and concentration boundary layer thicknesses. As it was shown in Figure 5.5 (a) and (b), more biofilm developed in low wall shear stress regions and after 36 h of biofilm growth, the wall shear stresses observed in the regions were biofilm developed stay clearly lower than the wall shear stresses observed in the remaining porous medium. On the other hand, mass transfer did not seem to play any role, consistent with presence of nutrient and electron acceptors in excess. If it would have had, less biofilm would have developed in the high concentration boundary layer thickness regions (see Figure 5.5 (c) and (d)).

The average of the wall shear stress distributions presented in Figure 5.5 (a) and (b) in the vicinity of the biofilm and at the surface of the bare grains shows a ca. 1.8 fold increase over the course of the experiment (see Table 5.1). The increase of the maximal wall shear stress measured is substantially higher (2.5) for the bare grains than for at the biofilm surface (1.4). The fact that the increase of the maximal values measured for the biofilm and for the bare grains is not identical might indicate that there is a maximal shear stress in the system that the biofilm cannot withstand. Here, this would imply a the biofilm shear or cohesive strength is of ca. 0.02 (N/m^2). Note that the biofilm shear strength

Table 5.1: Average and maximal values of the wall shear stress measured at the location of the nascent biofilm and at the surface of the biofilm as well as at the surface of the solid grains at the start and end of the experiment. The distinction was here performed by considering the data in one radius distance of the solid (nafion grains (N) or biofilm (BF) faces). I_F stands for the increase factor between the initial corresponding value and the value obtained after biofilm growth.

	$\langle\tau_w\rangle$ (N/m^2)			max(τ_w) (N/m^2)		
	T = 0 h	T = 36 h	I_F	T = 0 h	T = 36 h	I_F
BF	0.0037	0.0067	1.8	0.0152	0.0214	1.4
N	0.0065	0.0129	1.9	0.0391	0.0981	2.5

itself might also be distributed, as a consequence of the high physiological heterogeneity exhibited by biofilms (Stewart, 2014).

The largest biofilm patch sizes were found in pores of radii close to the average radii, but the wide distribution observed for the patch sizes did not indicate that the local geometry of the pore network was substantially influencing biofilm development. The maximal thickness of the biofilm patches decreased with increasing wall shear stress, showing that for the given porous medium and under the growth conditions considered, the wall shear stress plays a predominant role on controlling biofilm development.

5.4.2 Local vs. Non-local mass transfer

The local growth of biofilm was shown in this study to induce non-local changes in terms of hydrodynamics. A similar reasoning could be applied in terms of transport processes as well. Previous studies distinguished between external and internal mass transfer, where external refers to the local diffusion from the bulk through the concentration boundary layer in the biofilm and internal to diffusion within the biofilm itself. In the present study, neither non-local nor local mass transfer limitations did influence biofilm growth in the current study due to their presence in excess. However, in the case of nutrient or electron acceptor limitations and for a substratum exhibiting an intricate geometry as the one studied here, mass transfer might substantially influence biofilm growth both on a locally and on a non-locally. Locally, as in this study, biofilm growth will be defined by the diffusion of nutrients over the concentration boundary layer (external mass transfer). Non-locally, biofilm growth enhances the formation of stagnation zones, so that mass transfer limitations might also arise as a consequence of decreasing advection along these channels (non-local mass transfer) and due to dispersive processes resulting in non-local concentration differences in between channels. Furthermore, biofilm growth was shown to increase these dispersive effects (Seymour et al., 2004).

5.4.3 Influence of biofilm growth on the pore-scale radii and velocity distributions

The fact that the wall shear stresses remain fairly low in the vicinity of the biofilms might also be due to the impact of the growing biofilm on the pore-scale hydrodynamics. Coyte et al. (2017) showed that the local development of a tiny biofilm patch inducing an additional pressure drop at a given location of the pore network can result in substantial non-local changes in the larger scale flow picture. In the present study, the flow rate was kept constant over the course of the experiment. Invoking mass conservation and assuming that the biofilm is homogeneously distributed over a typical cylindrical pore (Thullner and Baveye, 2008) would mean that the average velocity would increase in an inverse quadratic relation relative to the pore radius ($v \propto Q/(\pi r^2)$, see dashed-dotted lines on Figure 5.7). However, as the data presented in this study show, the biofilm is not homogeneously distributed at the grain surface. Furthermore, even if the flow rate is kept constant and the pressure gradient thus increases at the flow cell scale, locally, it is also possible to have zones with only small pressure gradient variations. For similar pressure gradients, according to Poiseuille's law, the velocity is proportional to the square of the radius ($v \propto r^2$, see dashed lines on Figure 5.7), so that low velocity regions or stagnant zones might form with biofilm growth. These considerations suggests that predicting the local impact of the growth of biofilm on the pore-scale hydrodynamics is far from trivial, as for example, pore-scale velocities could increase or decrease quadratically with the pore radius variation. The complex influence of biofilm development on pore-scale hydrodynamics is illustrated by the radius-velocity relation presented in Figure 5.7. The experimental data presented in this study shows that there is a formation of high velocity regions, as also indicated by the high velocity tails of the velocity magnitude PDFs. But the pore radii decrease in the vicinity of the biofilm and there was also a substantial increase of the low tail of the velocity PDF.

5.5 Conclusions

In this study, experimental pore-scale hydrodynamic and structural data as well as biofilm morphologies in a progressively bioclogged porous medium are presented, with the aim of delineating the influence of the geometry of a 3D porous medium, wall shear stresses and mass transfer on the architecture of a growing biofilm. The main conclusions are:

- The maximal biofilm patch sizes are found in pores of average radii.
- The influence of wall shear stress and mass transfer on the growing biofilm could be assessed locally and showed that for the complex geometry considered, wall shear stresses and concentration boundary layer thicknesses are widely distributed.
- The wall shear stress measurements revealed that the attachment and development of biofilm patches was controlled by the local wall shear stress. As a consequence, the biofilm thickness decreased with increasing wall shear stress.

- Mass transfer processes did not influence biofilm growth, which can be explained by the excess of carbon source and electron acceptor so that neither external nor internal mass transfer limitations occurred.

- A maximal biofilm shear strength for the current system could be estimated at about 0.02 N/m^2.

Additionally, the development of biofilm substantially influenced the pore-scale hydrodynamics, as shown by the substantial increase of the average pore-scale velocities and wall shear stresses as a consequence of the porosity reduction upon biofilm growth. The developing biofilm also changed the connectivity of the pore network from on average more serial to more parallel. Using this method, the growth conditions used in the current study could be tailored to practical applications, providing key experimental data such as biofilm thickness or specific surface area allowing to optimize models aiming at upscaling mass transfer processes at the scale of a sand or trickling filter. Finally, with the fast pace of development of 3D printing technology (in terms of printable materials, geometries and scales accessible), the 3D printing of nafion (James et al., 2015) might soon allow similar investigations in other geometries (non-granular porous media, membrane feed spacer channels) and at scales relevant for other practical applications.

5.6 Acknowledgments

We thank Toni Blunschi for manufacturing the flow cells, Daniel Braun, Lucien Biolley and Ela Burmeister for providing some of the hardware necessary for this study and Peter Desmond for sharing the bacteria cultures. We acknowledge the contribution of Andris Wyss in the frame of a semester project. The authors thank Matthias Willmann for stimulating discussions and Stefan Hartmann for help with the X-ray μCT measurements. Part of this work has been performed by the use of the Empa Platform for Image Analysis (http://empa.ch/web/s499/software-/-imaging-platform) at Empa's Center for X-ray Analytics. Financial support is gratefully acknowledged from the Swiss National Science Foundation (SNF grant number 144645 and 172916) for M.C. and M.H. as well as a SNF mobility grant for doctoral students for M.C.. V.L.M. acknowledges the financial support of the AXA Research fund.

Bibliography

Battin, T. J., Sloan, W. T., Kjelleberg, S., Daims, H., Head, I. M., Curtis, T. P., and Eberl, L. (2007). Microbial landscapes: new paths to biofilm research. *Nat Rev Micro*, 5(1):76–81. pages

Blauert, F., Horn, H., and Wagner, M. (2015). Time-resolved biofilm deformation measurements using optical coherence tomography. *Biotechnology and Bioengineering*, 112(9):1893–1905. pages

Boltz, J., Morgenroth, E., and Sen, D. (2010). Mathematical modelling of biofilms and biofilm reactors for engineering design. *Water Science and Technology*, 62(8):1821–1836. pages

Bottero, S., Storck, T., Heimovaara, T. J., van Loosdrecht, M. C. M., Enzien, M. V., and Picioreanu, C. (2013). Biofilm development and the dynamics of preferential flow paths in porous media. *Biofouling*. pages

Carrel, M., Beltran, M. A., Morales, V. L., Derlon, N., Morgenroth, E., Kaufmann, R., and Holzner, M. (2017). Biofilm imaging in porous media by laboratory x-ray tomography: Combining a non-destructive contrast agent with propagation-based phase-contrast imaging tools. *PLOS ONE*, 12(7):e0180374. pages

Coyte, K. Z., Tabuteau, H., Gaffney, E. A., Foster, K. R., and Durham, W. M. (2017). Microbial competition in porous environments can select against rapid biofilm growth. *Proceedings of the National Academy of Sciences*, 114(2):E161–E170. pages

Davit, Y., Byrne, H., Osborne, J., Pitt-Francis, J., Gavaghan, D., and Quintard, M. (2013). Hydrodynamic dispersion within porous biofilms. *Physical Review E*, 87(1):012718. pages

Davit, Y., Iltis, G., Debenest, G., Veran-Tissoires, S., Wildenschild, D., Gerino, M., and Quintard, M. (2011). Imaging biofilm in porous media using x-ray computed microtomography. *Journal of Microscopy*, 242(1):15–25. pages de Anna, P., Le Borgne, T., Dentz, M., Tartakovsky, A. M., Bolster, D., and Davy, P. (2013). Flow intermittency, dispersion, and correlated continuous time random walks in porous media. *Physical Review Letters*, 110(18):184502. PRL. pages

Deng, W., Cardenas, M. B., Kirk, M. F., Altman, S. J., and Bennett, P. C. (2013). Effect of permeable biofilm on micro- and macro-scale flow and transport in bioclogged pores. *Environmental Science & Technology*, 47(19):11092–11098. pages

Derlon, N., Massé, A., Escudié, R., Bernet, N., and Paul, E. (2008). Stratification in the cohesion of biofilms grown under various environmental conditions. *Water Research*, 42(8–9):2102–2110. pages

Downie, H., Holden, N., Otten, W., Spiers, A. J., Valentine, T. A., and Dupuy, L. X. (2012). Transparent soil for imaging the rhizosphere. *PLoS ONE*, 7(9):e44276. pages

Drescher, K., Shen, Y., Bassler, B. L., and Stone, H. A. (2013). Biofilm streamers cause catastrophic disruption of flow with consequences for environmental and medical systems. *Proceedings of the National Academy of Sciences*, 110(11):4345–4350. pages

Eberl, H. J., Picioreanu, C., Heijnen, J. J., and van Loosdrecht, M. C. M. (2000). A three-dimensional numerical study on the correlation of spatial structure, hydrodynamic conditions, and mass transfer and conversion in biofilms. *Chemical Engineering Science*, 55(24):6209–6222. pages

Hall-Stoodley, L., Costerton, J. W., and Stoodley, P. (2004). Bacterial biofilms: from the natural environment to infectious diseases. *Nat Rev Micro*, 2(2):95–108. pages

Holzner, M., Morales, V. L., Willmann, M., and Dentz, M. (2015). Intermittent lagrangian velocities and accelerations in three-dimensional porous medium flow. *Physical Review E*, 92(1):013015. pages

Horn, H. and Lackner, S. (2014). *Modeling of Biofilm Systems: A Review*, pages 56–76. Springer International Publishing. pages

Hoyer, K., Holzner, M., Lüthi, B., Guala, M., Liberzon, A., and Kinzelbach, W. (2005). 3d scanning particle tracking velocimetry. *Experiments in Fluids*, 39(5):923–934. pages

James, D. C., Nicklaus, W. T., Matteo, A., and Kam, K. L. (2015). Fused filament 3d printing of ionic polymer-metal composites (ipmcs). *Smart Materials and Structures*, 24(12):125021. pages

Kapellos, G. E., Alexiou, T. S., and Payatakes, A. C. (2007). Hierarchical simulator of biofilm growth and dynamics in granular porous materials. *Advances in Water Resources*, 30(6–7):1648–1667. pages

Möhle, R. B., Langemann, T., Haesner, M., Augustin, W., Scholl, S., Neu, T. R., Hempel, D. C., and Horn, H. (2007). Structure and shear strength of microbial biofilms as determined with confocal laser scanning microscopy and fluid dynamic gauging using a novel rotating disc biofilm reactor. *Biotechnology and Bioengineering*, 98(4):747–755. pages

Morales, V. L., Dentz, M., Willmann, M., and Holzner, M. (2017). Stochastic dynamics of intermittent pore-scale particle motion in three–dimensional porous media: Experiments and theory. *Geophysical Research Letters*, pages n/a–n/a. pages

Nadell, C. D., Ricaurte, D., Yan, J., Drescher, K., and Bassler, B. L. (2017). Flow environment and matrix structure interact to determine spatial competition in pseudomonas aeruginosa biofilms. *eLife*, 6:e21855. pages

Picioreanu, C., van Loosdrecht, M. C. M., and Heijnen, J. J. (2000). A theoretical study on the effect of surface roughness on mass transport and transformation in biofilms. *Biotechnology and Bioengineering*, 68(4):355–369. pages

Pérez-Reche, F. J., Taraskin, S. N., Otten, W., Viana, M. P., Costa, L. d. F., and Gilligan, C. A. (2012). Prominent effect of soil network heterogeneity on microbial invasion. *Physical Review Letters*, 109(9):098102. PRL. pages

Qian, J., Horn, H., Tarchitzky, J., Chen, Y., Katz, S., and Wagner, M. (2017). Water quality and daily temperature cycle affect biofilm formation in drip irrigation devices revealed by optical coherence tomography. *Biofouling*, 33(3):211–221. pages

Rusconi, R., Guasto, J. S., and Stocker, R. (2014). Bacterial transport suppressed by fluid shear. *Nat Phys*, 10(3):212–217. pages

Seymour, J. D., Gage, J. P., Codd, S. L., and Gerlach, R. (2004). Anomalous fluid transport in porous media induced by biofilm growth. *Physical Review Letters*, 93(19):198103. pages

Siena, M., Riva, M., Hyman, J. D., Winter, C. L., and Guadagnini, A. (2014). Relationship between pore size and velocity probability distributions in stochastically generated porous media. *Physical Review E*, 89(1):013018. PRE. pages

Stewart, P. S. (2014). Biophysics of biofilm infection. *Pathogens and Disease*, 70(3):212–218. pages

Stewart, P. S. and Franklin, M. J. (2008). Physiological heterogeneity in biofilms. *Nat Rev Micro*, 6(3):199–210. pages

Stoodley, P., Lewandowski, Z., Boyle, J. D., and Lappin-Scott, H. M. (1998). Oscillation characteristics of biofilm streamers in turbulent flowing water as related to drag and pressure drop. *Biotechnology and Bioengineering*, 57(5):536–544. pages

Thullner, M. and Baveye, P. (2008). Computational pore network modeling of the influence of biofilm permeability on bioclogging in porous media. *Biotechnology and Bioengineering*, 99(6):1337–1351. pages von der Schulenburg, D. A. G., Pintelon, T. R. R., Picioreanu, C., Van Loosdrecht, M. C. M., and Johns, M. L. (2009). Three-dimensional simulations of biofilm growth in porous media. *AIChE Journal*, 55(2):494–504. pages

Wagner, M., Taherzadeh, D., Haisch, C., and Horn, H. (2010). Investigation of the mesoscale structure and volumetric features of biofilms using optical coherence tomography. *Biotechnology and Bioengineering*, 107(5):844–853. pages

Chapter 6

Supplementary material to Chapter 5

6.1 Quantitative analysis of the refractive index matching

In the present study, an 11 % w/v glucose solution (anyhdrous D-glucose, VWR, Dietikon, Switzerland) was used to provide the RIM. In order to determine the glucose concentration allowing to obtain an optimal RIM, we performed test series with spectrophotometer cuvettes (1 cm depth) filled with nafion and saturated with aqueous solutions of different glucose concentrations. A quantitative evaluation of the RIM was done by acquiring images of nine straight lines located on the backside of the cuvettes. The images of the lines were segmented and fitted by linear regressions. The metric allowing to evaluate the quality of the RIM was defined as a scaled root mean square error (SRMSE) of the regressions obtained:

$$SRMSE = \sqrt{\sum_{i=1}^{n}(y_i - \hat{y}_i)^2} \cdot C_F \tag{6.1}$$

with y_i being the position of the left extremity of the segmented line, $\hat{y}_i$ the estimate obtained from the regression and C_F a conversion factor (m/pixel) from image space to object space.

Figure 6.1 illustrates the approach used for the RIM quantification for saturation of the cuvette with water in (a) and with a glucose concentration of 11% w/v in (b). In both cases, the first images show the cropped straight line, the second the segmented straight line and the last one the left extremity of the segmented straight line and the corresponding regression. A visual inspection of the RIM obtained for the 11% w/v concentration reveals a very good matching, which is confirmed by the quantitative approach based on the SRMSE. Figure 6.1 (c) shows the SRMSE obtained for different concentrations between 0 and 20 % w/v. As the figure shows, the minimal SRMSE was obtained for a glucose concentration of 11 % w/v. Figure 6.1 (d) shows the evolution of the SRMSE during the growth of the biofilm obtained using the same approach. Upon growth of biofilm in the system, remained fairly constant, as it is shown by the obtained SRMSE in figure 6.1 (d). The 11 % w/v glucose solution was therefore used as a working fluid.

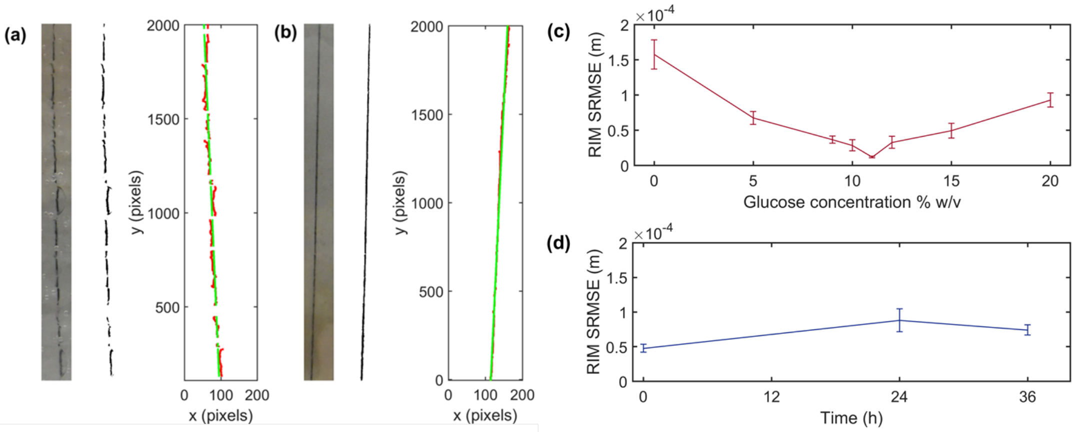

Figure 6.1: Cropped lines, segmented lines and corresponding linear regressions obtained for glucose concentrations of 0 (a) and 11 % w/v (b). (c) SRMSE values obtained for different glucose concentrations. (d) temporal evolution of the SRMSE during biofilm culturing.

6.1.1 Three-dimensional Particle Tracking Velocimetry

The Stokes Number of the particles, quantifying a possible role of inertia is defined as the ratio between the particle response time scale $t_P = \frac{(\rho_F - \rho_P) d_P^2}{18 \mu_F} \approx 10^{-7}$ s with ρ_F and ρ_P being the density of the fluid resp. the tracer particles and μ the dynamic viscosity of the fluid and the advective time scale (defined here as $t_A = d_N / v_P \approx 1s$), is $\mathcal{O}(10^{-7})$. This confirms that inertial effects are not of concern and that particles follow the flow reliably. For each 3D-PTV run, the tracer particle concentration is of 0.02 g/L, yielding a volume fraction of 0.002%. At this low concentration, the average inter-particle distance is of 4.5 mm. Therefore, particle-particle interactions within the very dilute suspension can be considered to be negligible. 0.2 ppm of surfactant (Tween, Cospheric, Santa Barbara, USA) were added and allowed to avoid particle agglomeration. The tracer particle diameter to nafion pellet diameter d_P / d_N is of ca. 35. For ratios of that order, filtration of tracer particles can be assumed to be negligible (Sakthivadivel and Einstein, 1970).

The fluorescent tracer particles were illuminated with a 100 W pulsed Nd:YLF laser (Darwin Duo, Quantronix, Hamden, USA). A Photron Fastcam SA5 with a resolution of $1024x1024$ pixels operated at 50 fps in combination with an image splitter was used to provide 4 stereoscopic views of particles within the porous medium. The redundant stereoscopic views proved to be useful upon biofilm growth, as in some views, the particles were obstructed by biofilm patches and two unobstructed views are sufficient to reconstruct 3D particle positions. In order to obtain an optimal distribution of the 3D-PTV data throughout the flow cell, the flow cell was imaged from both sides. A red filter was mounted on the camera objective. Each 3D-PTV measurement allowed to gather 10918 frames.

The data pre-processing consisted of a running image substraction with a lag of 50 images and a high pass filter. An open source 3D-PTV software (PTV, 2017) was used to detect the particles and the intersection of the epipolar lines allowed to establish correspondences between the particles in the different stereoscopic views. To cope with the slight decrease of the RIM due to biofilm growth, the tolerance to the epipolar line was set to twice the particle diameters (Willneff, 2003), which corresponds to the SRMSE observed after 48 h of biofilm growth. Between ca. 30 and 200 particles were tracked per frame, yielding $\mathcal{O}(10^6)$ data points for every measurement (4549 and 4193 trajectories for the time points T = 0 and T = 36 h respectively). The resulting accuracy of the raw particles coordinates is of ca 250 μm. In order to reconnect trajectories interrupted due to noise originating from light scattering due to local variations in the optical refractive index of the nafion grains or the biofilm, the particles were tracked in 6D position-velocity space (Haitao, 2008). Subsequently, a Savitzky-Golay filter using a quadratic polynomial fitted to 21 frames was applied to smooth Lagrangian trajectories in time (Saha et al., 2014). This filtering allowed to increase the accuracy along the trajectories down to ca. 50 μm (Holzner et al., 2015). Trajectories shorter than 21 frames or 1 mm total displacement were discarded. Finally, invoking the stationarity of the pore-scale flow and neglecting structural changes induced by biofilm growth over the time scale of the 3D-PTV experiments (ca. 1 h) allows to reduce the average inter-particle distance to ca. 50 μm.

6.2 Segmentation and registration

Figure 6.2 (a) and (b) show slices of the raw data respectively the segmented data obtained for the X-ray scan performed without the addition of contrast agent and reflecting the initial state of the porous medium, prior to biofilm culturing. Figure 6.2 (c) and (d) present similar slices obtained after the addition of the contrast agent, allowing to access the biofilm morphology. In Figure 6.2 (e) and (f), 3D-PTV data was registered and added superposed on the x-ray slices.

6.3 Information concerning the shear stress computation

Figure 6.3 (a) shows a close up of a pore body. The red arrows represent normal vectors to the triangulated faces representing the surface of the nafion grains. Figure 6.3 (b) shows

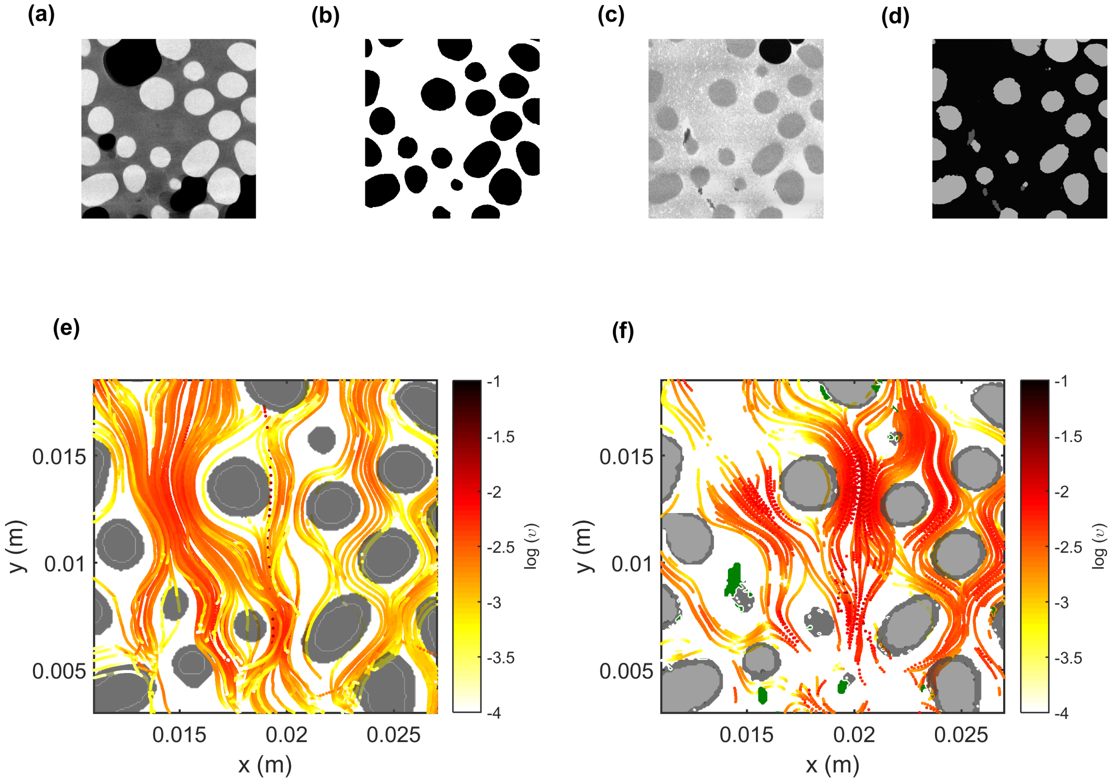

Figure 6.2: (a) and (b) show the raw and segmented slices obtained from the X-ray scan performed without the addition of contrast agent. (c) and (d) show similar slices obtained after the addition of the contrast agent. (e) and (f) show slices of the registered 3D-PTV and X-ray data.

velocity color-coded particle trajectories obtained with 3D-PTV in the pore presented in (a). The blue line is a normal vector of one the faces on which the velocity gradient is evaluated to estimate wall shear stress. The black dots represent the location of the pore medial lines. The Lagrangian or trajectory data presented in (b) is mapped on two example transects on a grid of 100 μm meshsize, providing a Eulerian flow field as presented in Figure 6.3 (c). The wall shear stress is finally obtained by interpolating the velocity gradient on the normal vectors of the solid surface faces based on the Eulerian flow field.

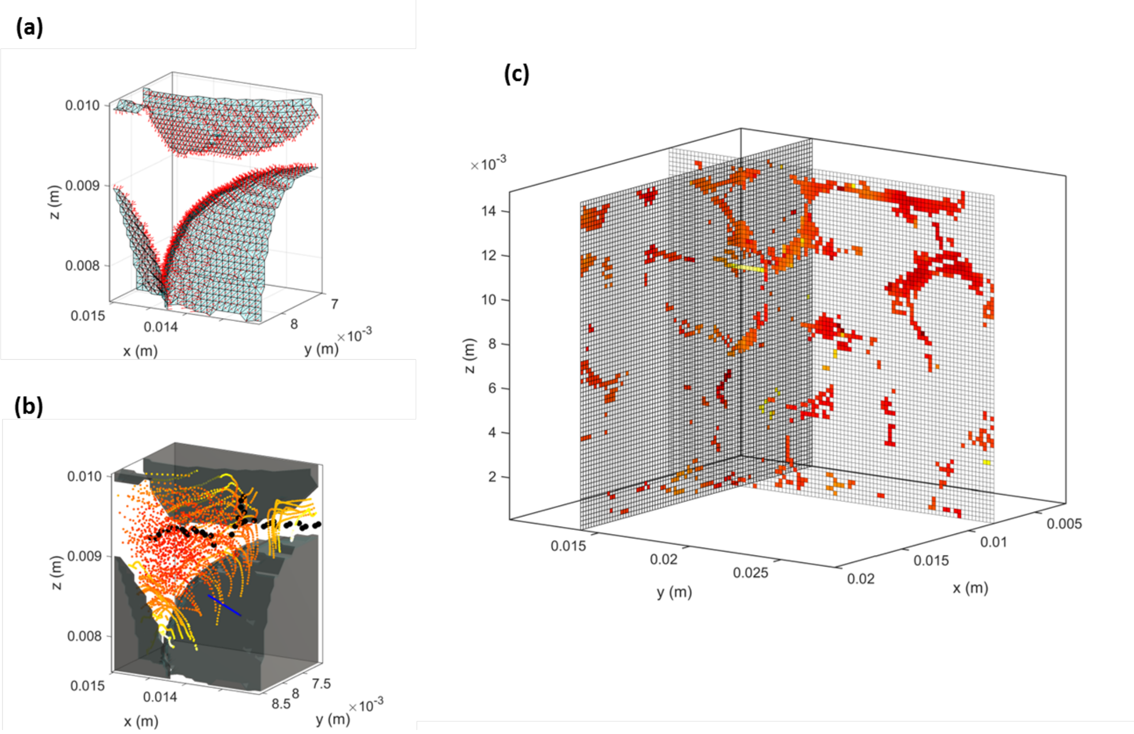

Figure 6.3: (a) Close up of a pore with the surface of the nafion grain in blue and normal to the faces obtained by Delaunay triangulation in red. (b) Nafion grains in dark gray, velocity-coded Lagrangian flow data and location of the pore central lines in black. A normal to one of the faces is shown in blue. (c) shows the Eulerian flow field obtained by mapping the Lagrangian data on a grid of 100 μm meshsize.

Bibliography

(2017). GitHub repository of the 3D-PTV software used in this study. `https://github.com/3dptv`. [Online; accessed February 21, 2018]. pages

Haitao, X. (2008). Tracking lagrangian trajectories in position–velocity space. *Measurement Science and Technology*, 19(7):075105. pages

Holzner, M., Morales, V. L., Willmann, M., and Dentz, M. (2015). Intermittent lagrangian velocities and accelerations in three-dimensional porous medium flow. *Physical Review E*, 92(1):013015. pages

Saha, D., Soos, M., Lüthi, B., Holzner, M., Liberzon, A., Babler, M. U., and Kinzelbach, W. (2014). Experimental characterization of breakage rate of colloidal aggregates in axisymmetric extensional flow. *Langmuir*, 30(48):14385–14395. pages

Sakthivadivel, R. and Einstein, H. (1970). Clogging of porous column of spheres by sediment. *Journal of the Hydraulics Division*, 96(2):461–472. pages

Willneff, J. (2003). *A spatio-temporal matching algorithm for 3D particle tracking velocimetry*, page 123. Institut für Geodäsie und Photogrammetrie an der Eidgenössichen Technischen Hochschule Zürich. pages

Chapter 7

Synthesis

7.1 Conclusion

This dissertation presents a pore-scale experimental investigation of the dynamics of biofilm development in porous media. Experimental techniques were developed to investigate progressive bioclogging in a three-dimensional porous medium.

The first part of this thesis shows that the progressive biofilm growth in a porous medium substantially influences pore-scale hydrodynamics. In particular, different hydrodynamic quantities such as the average pore-scale velocity magnitude, its variance or the velocity correlation length were observed to follow an exponential increase, which was related to the exponential bacterial growth. Additionally, the velocity magnitude probability density functions presented strong high and low tailing, reflecting the increasing heterogeneity of the pore network induced by biofilm growth. The bulk and the high tail of the pore-scale velocity distribution was remarkably reproduced by a gamma distribution. The shape parameter α of the gamma distribution, which can be understood to describe the connectivity of the porous medium, following the ad-hoc model based on theoretical considerations presented by (Holzner et al., 2015), decreased from 1.9 to 0.9. This decrease indicates that the pore geometry changes substantially from a predominantly parallel pore arrangement to a more serial one. A correlated CTRW based on the gamma distribution and on a stochastic velocity relaxation process provided a framework reproducing transport metrics obtained experimentally. This stochastic model captured the mean and mean square displacements measured with 3D-PTV remarkably and the conditional displacement PDFs qualitatively.

The approach presented in the first part of this thesis could be extended to model transport in other porous media whose heterogeneity are inherent to the original pore network or to networks including a dynamic component as a consequence of physico-chemical processes such as dissolution (Menke et al., 2015) or gas exchange (Klump et al., 2007).

The second part of this thesis presents a novel method allowing to obtain the spatial distribution of biofilm patches in a 3D porous medium. This X-ray microtomography method is novel in two aspects. First, iron sulfate is used as a contrast enhancing agent and it is dosed continuously during biofilm cultivation in order to be completely incorporated within the growing biofilm. Iron sulfate was already added to growing biofilm to enhance their optical properties in the frame of studies using optical coherence tomography (Wagner et al., 2010; Blauert et al., 2015) but never for X-ray micro computed tomography. Due to the relatively low density and corresponding attenuation coefficient of iron in the X-ray domain. An additional tool allowing to substantially increase the contrast was required. Therefore, an imaging method originally used to perform phase-retrieval with X-ray synchrotron data was used. This method consisted in performing the imaging on the X-ray laboratory source with a very long source-to-detector distance in combination with the application of a Lorentzian filter implemented prior to the tomographic reconstruction. The application of this commonly called "propagation" method provided a substantial noise reduction and contrast enhancement allowing to proceed to the segmentation of the biofilm, solid and liquid phases. Additionally, the segmented results were compared with results obtained another method based on the use of barium sulfate as a contrast agent (Davit et al., 2011). This comparison revealed that the injection of the barium sulfate caused the detachment of up to 50 % of the biofilm. The non-Newtonian rheological properties (i.e. shear-thinning) of the barium suflate suspension were identified to be at the root of the detachment observed.

Finally, the last part of this thesis introduced the combination of 3D-PTV and X-ray micro-tomography to delineate the influence of the porous medium topology, the hydrodynamic and mass transfer processes on the development and the morphology of biofilms. A biofilm was cultivated in a 3D porous medium for 36 h under a constant flow rate and with nutrients and electron acceptors provided in excess. The hydrodynamic and mass transfer processes were quantitatively accounted for by analyzing the distributions of the wall shear stress τ_w and of the concentration boundary layer thickness δ_c. The growing biofilm substantially influenced the pore-scale hydrodynamics. Interestingly, the experimental measurements revealed that the wall shear stress controlled the location of the nascent biofilm patches, as the wall shear stress measured at these locations were significantly lower than where biofilm did not develop. Additionally, upon biofilm growth, the wall shear stress measured stayed fairly low in the channels colonized by biofilms whereas it increased in the remaining ones. This indicates that locally, the biofilm induced a redirection of the flow in channels that were not colonized. Neither external nor internal mass transfer processes did seem to influence biofilm development, as biofilm developed in regions with the highest concentration boundary layer thicknesses. This can be explained by the high concentrations of nutrients and electron acceptors present in the feed solution.

7.2 Suggestions for future work

There are different meaningful directions in which the work presented in this thesis could be extended. To begin with, the results presented in the first part of this thesis highlighted the need to investigate the role played by the biofilm permeability on flow within porous biofilm and therefore as well on convective as on diffusive transport and and ultimately on reaction processes within biofilms. Microscale measurements of diffusion processes within biofilms suggests that the biofilm permeability can be highly variable (Stewart, 1998), which is reflected in the multiscale nature of the transport problem within porous biofilms (Davit et al., 2013), as flow occurs in sub-microscopical channels (Stoodley et al., 1994), in between extra-cellular polymeric fibers and down to within the bacterial cells (Kapellos et al., 2007b). Therefore, measurements of effective biofilm permeability allowing to link efficiently micro- and macroscale transport are required. The estimation of such effective permeability values could be performed by comparing results obtained from numerical modeling to experimental data. In that sense, flow in the porous medium and within the biofilm could be solved using Brinkman's equations (Kapellos et al., 2007a; Deng et al., 2013) applied to real three-dimensional geometries obtained with X-ray micro-tomography (Peszynska et al., 2016). The transport problem could be solved numerically and subsequently, the permeability of the biofilm estimated by comparing experimental information on the transport processes such as passive tracer breakthrough curves to the results of the transport model. Additionally, the effective biofilm permeability obtained could then be accounted for in macroscopic models such as multirate mass transfer (Dentz and Berkowitz, 2003), dual-porosity (Orgogozo et al., 2013) or dual-continuum approaches (Porta et al., 2015).

In the work presented in this thesis, the carbon source and electron acceptors were provided in excess and neither chemical gradients nor nutrient limitations were imposed on the systems. However, planktonic bacteria and biofilms are ubiquitously confronted to chemical gradients (Hall-Stoodley et al., 2004; Stocker, 2012). This is very true in soils as well (Or et al., 2007), as for instance biodegradation of pollutants is commonly accepted to predominantly take place in very local reactive hot spots at pollutant plumes fringes (Jobelius et al., 2011). Therefore, accounting for these ubiquitous chemical gradients on reactive processes is paramount in order to accurately model reactions in the frame of biodegradation processes (Meckenstock et al., 2015).

Finally, the porous medium considered in this study was formed from nafion pellets, in order to achieve a refractive index matching with an aqueous solution. Therefore, the structure considered was limited by the granular media available. However, recent technological advances in 3D printing (James et al., 2015) showed that nafion could be processed and printed in order to produce versatile structures. Therefore, nafion could be used to manufacture similar generic porous media models allowing to systematically vary parameters relative to biofilm growth (hydrodynamic conditions, nutrients and electron acceptors availablity etc.) for a given and fixed geometry and the structure of the medium and of the biofilm image by X-ray μCT. Specific structural parameters that could be varied are polydisperse size distributions of the granular material (only monodisperse was considered in this thesis), variable shape of the grain. Thereby, pore-scale hydrodynamics could either be measured with 3D-PTV or solved for numerically. Additionally, the versatility of 3D printing would not restrain to porous media mimicking soils, but models closer to practical applications, such as membrane feed-spacer or catheters could then also be considered.

Bibliography

Blauert, F., Horn, H., and Wagner, M. (2015). Time-resolved biofilm deformation measurements using optical coherence tomography. *Biotechnology and Bioengineering*, 112(9):1893–1905. pages

Davit, Y., Byrne, H., Osborne, J., Pitt-Francis, J., Gavaghan, D., and Quintard, M. (2013). Hydrodynamic dispersion within porous biofilms. *Physical Review E*, 87(1):012718. pages

Davit, Y., Iltis, G., Debenest, G., Veran-Tissoires, S., Wildenschild, D., Gerino, M., and Quintard, M. (2011). Imaging biofilm in porous media using x-ray computed microtomography. *Journal of Microscopy*, 242(1):15–25. pages

Deng, W., Cardenas, M. B., Kirk, M. F., Altman, S. J., and Bennett, P. C. (2013). Effect of permeable biofilm on micro- and macro-scale flow and transport in bioclogged pores. *Environmental Science & Technology*, 47(19):11092–11098. pages

Dentz, M. and Berkowitz, B. (2003). Transport behavior of a passive solute in continuous time random walks and multirate mass transfer. *Water Resources Research*, 39(5):n/a–n/a. pages

Hall-Stoodley, L., Costerton, J. W., and Stoodley, P. (2004). Bacterial biofilms: from the natural environment to infectious diseases. *Nat Rev Micro*, 2(2):95–108. pages

Holzner, M., Morales, V. L., Willmann, M., and Dentz, M. (2015). Intermittent lagrangian velocities and accelerations in three-dimensional porous medium flow. *Physical Review E*, 92(1):013015. pages

James, D. C., Nicklaus, W. T., Matteo, A., and Kam, K. L. (2015). Fused filament 3d printing of ionic polymer-metal composites (ipmcs). *Smart Materials and Structures*, 24(12):125021. pages

Jobelius, C., Ruth, B., Griebler, C., Meckenstock, R. U., Hollender, J., Reineke, A., Frimmel, F. H., and Zwiener, C. (2011). Metabolites indicate hot spots of biodegradation and biogeochemical gradients in a high-resolution monitoring well. *Environmental Science and Technology*, 45(2):474–481. pages

Kapellos, G. E., Alexiou, T. S., and Payatakes, A. C. (2007a). Hierarchical simulator of biofilm growth and dynamics in granular porous materials. *Advances in Water Resources*, 30(6–7):1648–1667. pages

Kapellos, G. E., Alexiou, T. S., and Payatakes, A. C. (2007b). A multiscale theoretical model for diffusive mass transfer in cellular biological media. *Mathematical Biosciences*, 210(1):177–237. pages

Klump, S., Tomonaga, Y., Kienzler, P., Kinzelbach, W., Baumann, T., Imboden, D. M., and Kipfer, R. (2007). Field experiments yield new insights into gas exchange and excess air formation in natural porous media. *Geochimica et Cosmochimica Acta*, 71(6):1385–1397. pages

Meckenstock, R. U., Elsner, M., Griebler, C., Lueders, T., Stumpp, C., Aamand, J., Agathos, S. N., Albrechtsen, H.-J., Bastiaens, L., Bjerg, P. L., Boon, N., Dejonghe, W., Huang, W. E., Schmidt, S. I., Smolders, E., Sørensen, S. R., Springael, D., and van Breukelen, B. M. (2015). Biodegradation: Updating the concepts of control for microbial cleanup in contaminated aquifers. *Environmental Science and Technology*, 49(12):7073–7081. pages

Menke, H. P., Bijeljic, B., Andrew, M. G., and Blunt, M. J. (2015). Dynamic three-dimensional pore-scale imaging of reaction in a carbonate at reservoir conditions. *Environmental Science & Technology*, 49(7):4407–4414. pages

Or, D., Smets, B. F., Wraith, J. M., Dechesne, A., and Friedman, S. P. (2007). Physical constraints affecting bacterial habitats and activity in unsaturated porous media – a review. *Advances in Water Resources*, 30(6):1505–1527. pages

Orgogozo, L., Golfier, F., Buès, M. A., Quintard, M., and Koné, T. (2013). A dual-porosity theory for solute transport in biofilm-coated porous media. *Advances in Water Resources*, 62:266–279. pages

Peszynska, M., Trykozko, A., Iltis, G., Schlueter, S., and Wildenschild, D. (2016). Biofilm growth in porous media: experiments, computational modeling at the porescale, and upscaling. *Advances in Water Resources*, 95:288–301. pages

Porta, G. M., Bijeljic, B., Blunt, M. J., and Guadagnini, A. (2015). Continuum-scale characterization of solute transport based on pore-scale velocity distributions. *Geophysical Research Letters*, 42(18):7537–7545. pages

Stewart, P. S. (1998). A review of experimental measurements of effective diffusive permeabilities and effective diffusion coefficients in biofilms. *Biotechnology and Bioengineering*, 59(3):261–272. pages

Stocker, R. (2012). Marine microbes see a sea of gradients. *Science*, 338(6107):628. pages

Stoodley, P., deBeer, D., and Lewandowski, Z. (1994). Liquid flow in biofilm systems. *Applied and Environmental Microbiology*, 60(8):2711–2716. pages

Wagner, M., Taherzadeh, D., Haisch, C., and Horn, H. (2010). Investigation of the mesoscale structure and volumetric features of biofilms using optical coherence tomography. *Biotechnology and Bioengineering*, 107(5):844–853. pages

Acknowledgements

Acknowledgements

I am deeply grateful to all the people that helped and supported me during this PhD journey. First, I would like to thank Markus Holzner for providing me the opportunity to work under his supervision. Thank you for your time, your support and your patience during these four years. Moreover, I would like to thank Verónica Morales for her availability, her help and support. Thank you very much for having hosted me in Davis! I am further grateful to Tanguy Le Borgne for serving as a referee as well as to Eberhard Morgenroth and Nicolas Derlon for their support and advice. A big thank you goes to Rolf Kaufmann and Mario Beltran for their help and advice concerning the X-ray measurements as well as to Marco Dentz for his availability and help with the correlated CTRW. I also would like to thank all the members of the EFM group and of the IFU. Ela, Dani, Lucien and René, thank you for your help with some lab material / hardware. Lukas, thanks for these tabletennis lunches. Marius sharing Semmeln with you on ski slopes always was a pleasure. Peter, thank for all the biofilm related discussions. I am really thankful for the support received by my whole family during these four years. Finally, I am extremely grateful to my wife Martina. Thank you for your never-ending support and encouragements during these four years.

Curriculum vitae

Maxence Carrel

Date of birth: August 19, 1988
Nationality: Swiss

maxence.carrel@gmail.com

Education

10/2013 – 06/2017 Ph.D. studies at ETH Zurich, Switzerland, Institute of Environmental Engineering, Thesis: "Experimental and numerical investigation of biofilm growth dynamics in porous medium" (Supervision:Prof.Dr.Markus Holzner)

09/2011 – 06/2013 Master Degree in Environmental Engineering at Eidgenössische Technische Hochschule Zurich, Switzerland, Degree: Master of Science; Master Thesis: "Membrane Ultrafiltration: A Study of the Combined Use of Iron Chloride for Coagulation and of Hypochlorite for Disinfection" (Supervision: Dr. Wouter Pronk and Prof. Dr. Eberhard Morgenroth)

09/2007 – 06/2010 Bachelor Degree in Environmental Engineering at Eidgenössische Technische Hochschule Zurich and École Polytechnique Fédérale Lausanne, Switzerland, Degree: Bachelor of Science; Bachelor Thesis: "Which melt models for which temporal resolution?" (Supervision: Dr. Francesca Pellicciotti)

06/2007 Maturité gymnasiale bilingue français-allemand. Gymnase de Marcelin, Morges, Switzerland

Journal Publications

1. M. Carrel, M.A. Beltran, V.L. Morales, N. Derlon, E. Morgenroth, R. Kaufmann & M. Holzner. Biofilm Imaging in Porous Media by Laboratory X-ray Tomography: Combining a Non-Destructive Contrast Agent with Propagation-Based Phase-Contrast Imaging Tools (2017). *PLOS ONE*
doi: 10.1371/journal.pone.0180374

2. M. Carrel, V.L. Morales, M. Dentz, N. Derlon, E. Morgenroth, R. Kaufmann & M. Holzner. Pore-scale hydrodynamics in a progressively bioclogged three-dimensional porous medium: 3D particle tracking experiments and stochastic transport modelling. Submitted to *Water Resources Research*

3. M. Carrel, M.A. Beltran, V.L. Morales, N. Derlon, E. Morgenroth, R. Kaufmann & M. Holzner. Bioclogging in three-dimensional porous media: a pore-scale experimental investigation. Submitted to *Water Research*

Conference Contributions

1. M. Carrel, V.L. Morales, R. Kaufmann, N. Derlon, E. Morgenroth & M. Holzner: "Bioclogging in porous media: preferential flow paths and anomalous transport", AGU Fall Meeting, San Francisco, USA, December 12-16, 2016.
2. M. Carrel, V.L. Morales, R. Kaufmann, N. Derlon, E. Morgenroth & M. Holzner: "Bioclogging in porous media: preferential flow paths and anomalous transport", Biofilms 7 Conference, Porto, Portugal, June 26-27, 2016.
3. M. Carrel, V.L. Morales & M. Holzner: "Lagrangian flow investigation in three-dimensional porous medium flow", 8th International Conference on Porous Media, Cincinnati, USA, May 9-13, 2016.
4. M. Carrel, V.L. Morales, R. Kaufmann, N. Derlon, E. Morgenroth & M. Holzner: "Dynamics of biofilm development in porous media: bioclogging, preferential flow pathways and anomalous dispersion", 8th International Conference on Porous Media, Cincinnati, USA, May 9-13, 2016.
5. M. Carrel, V.L. Morales, R. Kaufmann, N. Derlon, E. Morgenroth & M. Holzner: "Influence of biofilm growth on intermittency of Lagrangian velocities and accelerations in porous media", IWA Specialist Conference on Biofilms in drinking water systems: From treatment to tap, Arosa, Switzerland, August 23-26, 2015.
6. M. Carrel, V.L. Morales, R. Kaufmann, N. Derlon, E. Morgenroth & M. Holzner: "Influence of biofilm growth on intermittency of Lagrangian velocities and accelerations in porous media", Research seminar given at the Summer School: Flow and

Transport in Porous and Fractured Media: Development, Protection, Management and Sequestration of Subsurface Fluids, Cargèse, France, July 20 - August 1, 2015.

7. M. Carrel, N. Derlon, E. Morgenroth & M. Holzner: "Investigation of the biofilm-flow interactions with three-dimensional Particle Tracking Velocimetry, Optical Coherence Tomography and Confocal Laser Scanning Microscopy", Biofilms 6 Conference, Vienna, Austria, May 11-14, 2014.